RIGOROUS TASK-BASED OPTIMIZATION OF INSTRUMENTATION, ACQUISITION PARAMETERS AND RECONSTRUCTION METHODS FOR MYOCARDIAL PERFUSION SPECT

by

Mickel Ghaly

A dissertation submitted to Johns Hopkins University in conformity with the requirements for the degree of Doctor of Philosophy

Baltimore, Maryland

September, 2014

ABSTARCT

Coronary artery disease (CAD) is the most common type of heart disease and a major cause of death in the United States. Myocardial perfusion SPECT (MPS) is a well-established noninvasive diagnostic imaging technique for the detection and functional characterization of CAD. MPS involves intravenous injection of a radiopharmaceutical (e.g. Tc-99m sestamibi) followed by acquiring planar images of the 3-D distribution of the radioactive labeled agent, using one or more gamma cameras that are rotated around the patient, at different projection views. Transaxial reconstructed images are formed from these projections using tomographic image reconstruction methods. The quality of SPECT images is affected by instrumentation, acquisition parameters and reconstruction/compensation methods used. The overall goal of this dissertation was to perform rigorous optimization of MPS using task-based image quality assessment methods and metrics, in which image quality is evaluated based on the performance of an observer on diagnostic tasks relevant to MPS. In this work, we used three different model observers: the Ideal Observer (IO), and its extension, the Ideal Observer with Model Mismatch (IO-MM) and an anthropomorphic observer, the Channelized Hotelling Observer (CHO).

The IO makes optimal use of the available information in the image data. However, due to its implicit perfect knowledge about the image formation process, using the IO to optimize imaging systems could lead to differences in optimal parameters compared to those optimized for humans (or CHO) interpreting images that are reconstructed with imperfect compensation for image-degrading factors. To address this, we developed the IO-MM that allows optimization of acquisition and instrumentation parameters in the absence of compensation or the presence of non-ideal compensation methods and evaluates them in terms of the IO.

In order to perform clinically relevant optimization of MPS and due to radiation concerns that limit system evaluation using patient studies, we designed and developed a population of

digital phantoms based on the 3-D eXtended CArdiac Torso (XCAT) phantom that provides an extremely realistic model of the human anatomy. To make the simulation of the population computationally feasible, we developed and used methods to efficiently simulate a database of Tc-99m and Tl-201 MPS projections using full Monte Carlo (MC) simulations. We used the phantom population and the projection database to optimize and evaluate the major acquisition and instrumentation parameters for MPS.

An important acquisition parameter is the width of the acquisition energy window, which controls the tradeoff between scatter and noise. We used the IO, IO–MM and CHO to find the optimal acquisition energy window width and evaluate various scatter modeling and compensation methods, including the dual and triple energy window and the Effective Source Scatter Estimation (ESSE). Results indicated that the ESSE scatter estimation method provided very similar performance to the perfect scatter model implicit in the IO.

Collimators are a major factor limiting image quality and largely determine the noise and resolution of SPECT images. We sought the optimal collimator with respect to the IO performance on two tasks related to MPS: binary detection and joint detection and localization. The results of this study suggested that higher sensitivity collimators than those currently used clinically appear optimal for both of the diagnostic tasks. In a different study, we evaluated and compared various CDR modeling and compensation methods using the IO (i.e. the observer implicitly used a true CDR model), IO-MM (using an approximate or no model of the CDR) and CHO, operating on images reconstructed using the same compensation methods. Results from the collimator and acquisition energy window optimization studies indicated that the IO-MM had good agreement with the CHO, in terms of the range of optimal Tc-99m acquisition energy window widths, optimal collimators, and the ranking of scatter and CDR compensation methods. The IO was in agreement with the CHO when model mismatch was small.

Dual isotope simultaneous acquisition (DISA) rest Tl-201/stress Tc-99m MPS has the

potential to provide reduced acquisition time, increased patient comfort, and perfectly registered images compared to separate acquisition protocols, the current clinical protocols of choice. However, crosstalk contamination, where photons emitted by one radionuclide contribute to the image of the other, degrades image quality. In this work, we optimized, compared and evaluated dual isotope MPS imaging with separate and simultaneous acquisition using the IO in the context of 3-class defect detection task. Optimal acquisition parameters were different for the two protocols. Results suggested that DISA methods, when used with accurate crosstalk compensation methods, could potentially provide image quality as good as that obtained with separate acquisition protocols.

Advisor: Eric C. Frey, Ph.D.

Reader: Jonathan M. Links, Ph.D.

ACKNOWLEDGEMENTS

There are so many people that I need to thank for assisting during my graduate studies at Johns Hopkins University. First and foremost, I would like to thank my advisor Dr. Eric C. Frey for all of the guidance that he has given me over the last several years. He has been an invaluable support and inspiration, a thoughtful advisor and a wonderful mentor. Without him, completing this thesis would not have been possible.

I would also like to thank Dr. Jonathan M. Links for being the second reader of my thesis and for many helpful comments, both via email and during meetings.

I also want to thank Dr. Benjamin M. W. Tsui for starting the Division of Medical Imaging Physics at Johns Hopkins University and providing a wonderful environment to learn and grow.

Special thanks goes to Martin Stumpf for keeping the computer cluster running and helping me when I needed assistance in both my research and personal life.

Many thanks to all members of the Division of Medical Imaging Physics who provided a friendly yet dedicated atmosphere. I especially thank Dr. Emad M. Boctor, Dr. Yong Du and Dr. George S. K. Fung for their support and valuable discussions. I am also very grateful to LaVahn Tunstall for all of her hard administrative work during my time here. I would also like to thank both former and current students, Dr. Xing Rong, Xin Li, Jakir Hossain and Andrew Rittenbach for all the memories we made together in the office, at conferences and retreats.

I would like to thank my close friends and extended family from Church for their love, care, and continuous encouragement over the years. Particular thanks go to Fr. Shenouda Ebeid, (Ayman)^2, (Maria)^2, (Mary)^2, (Michael)^2, Angela, Amy, Christine, Emad, Eman, Emily, Engy, Eric, Iriny, Jeremy, Lydia, Mina, Monda, Monica, Rita, Sarah, Sherif, Toby, Peter, and Youssef

Words can never express how thankful I am to my family, Christine, Mark, and Natalie for all of the support that they have given me. I thank them for being understanding for all of the late nights or weekends that I had to spend working. I love them all so much. The everlasting love, encouragement, prayers of my mother, Flora Ghaly, has made my success possible. I am thankful to my sister, Marianne, who always has so much confidence in me. This work is in memory of my father, Adel Ghaly, who first taught me that engineering is a life style. I would also like to thank my in-laws for their continuous support and prayers.

Above all, I thank the beneficent and almighty God for His continuous work in my life. To Him is due all glory.

TABLE OF CONTENTS

LIST OF TABLES

LIST OF FIGURES

1. Introduction

1.1 Problem domain and significance

Coronary artery disease (CAD) is the most common type of heart disease. It is a major cause of death in the United States. Single Photon Emission Computed Tomography (SPECT) is a widely-used and cost-effective modality for, among other applications, diagnosis of CAD using myocardial perfusion SPECT (MPS). It is a relatively mature technology and there has been a lot of previous work on optimizing various parameters and methods. However, because of its widespread use, even relatively minor improvements would be highly significant, worthwhile, and cost-effective. The overall goal of this work is to perform rigorous and comprehensive optimization of instrumentation, acquisition and reconstruction/compensation methods in the context of single and dual isotope MPS imaging, using extremely realistic simulations of patients, patient populations, and imaging systems combined with state-of-the-art task-based image quality measures. This work in this dissertation was designed to have an impact in two ways.

First, we have optimized acquisition protocols, and processing methods that can have significant impact both immediately and in the future. Optimal energy windows and reduced acquisition times or injected activities could be implemented immediately by clinical practitioners; optimal reconstruction methods and compensation methods could be implemented by manufacturers with somewhat modest software updates; and optimal collimators could be implemented by through the production of new collimators for existing systems, a relatively modest expense compared to the development and purchase of new systems. The immediate impact on MPS is important because it is a well-established, validated, and widely used modality. Thus, there is the potential for significant healthcare impact in the near future.

The second area of significant potential impact is on the process of optimizing medical imaging protocols and procedures in general. Many medical imaging modalities involve the creation of secondary images (e.g., tomographic reconstructions) from primary measured data. A demonstration that optimizing the primary images using the Ideal Observer (IO) provides optimal secondary images would thus be an important advance in the development of optimal imaging protocols and instrumentation for medical imaging in general. In addition, in many modalities there is mismatch between the model used in constructing the final image and the true image formation process. The development and validation of the IO that includes model-mismatch (IO-MM) could have a substantial impact on development and evaluation of methods for modeling and compensating for these effects in a way that is much more computationally efficient than performing a reconstruction-space observer study. Finally, this work was designed as a very ambitious and realistic effort to apply rigorous and realistic simulation methods and image quality metrics to the optimization of medical imaging systems. It thus demonstrates the feasibility of implementing this kind of optimization *in silico*.

1.2 Organization

This dissertation is comprised of a background chapter and a series of chapters describing the findings and outcomes of this research.

Chapter 2 provides background by giving a brief overview of MPS imaging, the basic components of SPECT system, factors that affect the quality of SPECT images and the key elements of task-based image quality assessment.

Chapter 3 describes the design and development of a realistic digital phantom population and the corresponding Tc-99m and Tl-201 projection images. The phantom population is based on the three-dimensional (3D) eXtended CArdiac Torso (XCAT) phantom that provides an accurate, realistic and flexible model of the human anatomy. We use the phantom population in the optimization of SPECT instrumentation and acquisition parameters and the evaluation of compensation methods in the context of single and dual isotope MPS imaging. This work has been published in [1].

In Chapter 4, we optimize the collimator parameters to find the collimator that provides the optimal tradeoff between image noise and resolution with respect to the IO performance on two tasks related to MPS: perfusion defect detection and joint detection and localization. The IO is a mathematical observer that outperforms all other observers and makes optimal use of all the information in the raw data. We used the IO operating on projection data to find the optimal collimator that would preserve the maximum possible information in the sinogram regardless of the reconstruction method used to convert the sinogram into images suitable for human interpretation.

Chapter 5 considers the joint optimization of the collimator parameters and the reconstruction method. We use 2 classes of model observers: the IO, an extension of the IO proposed by us, the Ideal Observer with Model Mismatch (IO-MM) operating on projection images and an anthropomorphic model observer, the Channelized Hotelling Observer (CHO), used to, model the performance of human observers on reconstructed images. The IO-MM allows optimization of acquisition and instrumentation parameters in the absence or the presence of non-ideal compensation methods and evaluates them in terms of the IO performance.

In Chapter 6, we applied three different model observers, the IO, IO-MM and the CHO, for the optimization of Tc-99m acquisition energy window and the evaluation of different scatter estimation methods in the context of myocardial perfusion SPECT defect detection [2-4].

Chapter 7 focuses on the optimization and comparison of simultaneous and separate acquisition protocols for dual isotope MPS. Simultaneous acquisition of the rest and stress images protocols offers a number of advantages over separate acquisition. However, crosstalk contamination, where photons from one radionuclide are detected in the photopeak energy window of the other radionuclide, degrades image quality. Optimizing the rest Tl-201 energy window width and the relative injected activities of Tc-99m and Tl-201 could reduce the impact of crosstalk. In this work, we optimized the acquisition parameters for separate and simultaneous protocols using the IO operating on projection data in the context of three-class MPS defect detection task [5].

Chapter 8 summarizes the results from previous chapters, discusses the contributions of this work and describes some possible areas for future work that include factors not yet fully optimized or hypotheses generated by this work.

2. Background

2.1 Nuclear Medicine Imaging

Nuclear Medicine (NM) imaging is a medical imaging modality for producing images that depict the spatial distribution of radioactivity in the body. A pharmaceutical labeled with a radionuclide, e.g. Tc-99m sestamibi, is administered to the patient by intravenous injection, inhalation or ingestion. Depending on its biokinetics, the radiotracer distributes within the body and often concentrates in a specific tissue type or receptor. The radionuclide atoms of the radiopharmaceutical compound decay and emit gamma photons that penetrate through the patient's body. On their way out of the body, photons may be absorbed or scatter in the intervening tissues. Since gamma photons are emitted isotropically, imaging devices, such as gamma cameras, only record photons that travel in a specific direction to allow for spatial localization of the emitted photons. The spatial distribution of the recorded photons reflects the spatial distribution of the radiopharmaceutical within the patient and thus determines the tissue's physiological or biochemical functioning. In NM, images are formed by recording radiation emitted from within the body. This process is different than X-ray imaging, where external radiation is transmitted through the body to form an image.

There are two broad classes of NM imaging: single photon imaging including planar imaging and single photon emission computed tomography (SPECT) and positron imaging [positron emission tomography (PET)]. Single photon imaging uses radionuclides that decay by gamma-ray emission. A planar image depicts a single projection, from one particular view, of the radionuclide distribution in the patient. Although planar images have little depth information, planar imaging is still diagnostically useful for various clinical tasks such as bone scanning to assess the metastatic spread of cancer cells. SPECT is a tomographic nuclear medicine imaging modality that generates cross-sectional images of the radiotracer uptake in the body by acquiring multiple 2D planar images from many views around the patient followed by reconstructing images of the distribution of the radionuclide. One of the most common SPECT procedures is myocardial perfusion imaging using agents containing the radionuclides Tc-99m or Tl-201 for the diagnosis of the coronary artery disease. Positron imaging is a tomographic NM imaging modality that uses radionuclides that decay by positron emission. The emitted positron eventually annihilates by interaction with an electron. At the annihilation site, two 511 keV photons originate simultaneously and leave in approximately opposite directions. A ring of detectors surrounding the patient subsequently detects the two photons. If two events are detected simultaneously in two detectors, one assumes that annihilation occurred on an imaginary line connecting the two opposing detectors. Tomographic reconstruction methods can then be used to reconstruct images of the tracer distribution. In this dissertation, we will focus on SPECT imaging.

2.2 Myocardial perfusion SPECT

The heart is a muscular organ that pumps the blood through the circulatory system by rhythmic contraction and dilation. Like other muscles, the heart requires a continuous supply of oxygen-rich blood to work properly. The heart muscle gets the blood it needs from the coronary arteries. Coronary artery disease (CAD) is the most common type of heart disease and is the leading cause of death in the United States, killing nearly 380,000 people annually [6]. CAD develops when cholesterol-laden plaque builds up along the inner walls of the coronary arteries, resulting in narrowing of the arteries and thus reduction of blood flow to the heart. The decreased blood flow, known as ischemia, may cause chest pain (angina), irregular or faster heart beats, shortness of breath, sweating and nausea. Moreover, if the artery is completely blocked, known as a myocardial infarction or heart attack, permanent damage of the heart muscle may occur. Figure 2-1 shows a heart with damaged muscle and a blocked artery.

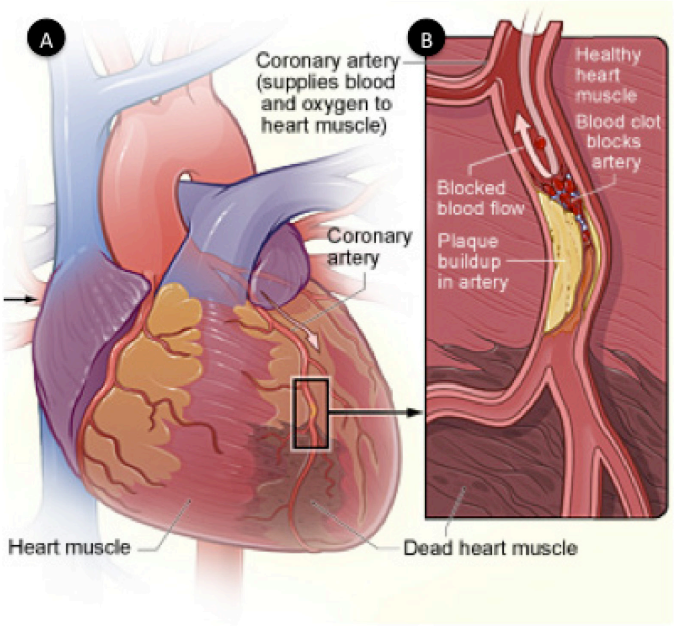

Figure 2-1. An overview of a heart and coronary artery showing damage (dead heart muscle) caused by a heart attack (left). A cross-section of the coronary artery with plaque buildup and a blood clot (right). http://www.nhlbi.nih.gov/health/health-topics/images/heart_attack_10-4-11.jpg.

Myocardial perfusion SPECT (MPS) is a well-established noninvasive diagnostic imaging technique for the detection and functional characterization of CAD, and is one of the most commonly performed nuclear medicine imaging procedures. MPS is capable of identifying regional abnormalities in coronary artery blood flow and determining their physiological relevance to myocardial function and viability. MPS requires the intravenous injection of a radiopharmaceutical followed by imaging of regional myocardial uptake under rest (i.e. the patient is at rest) and stress, where perfusion imaging agent is injected after exercise or administration of a pharmacological stressor, to unmask myocardial perfusion deficits not evident at rest.

Stress and rest images are used to distinguish normally perfused images (uniform tracer uptake at rest and stress), infarcted regions (fixed defects), where perfusion tracers are not taken up thus presenting as abnormalities in both the stress and rest images, and ischemic regions (reversible defects) where there is a region of reduced uptake in the stress image but not at rest. Therefore, the diagnosis using stress/rest myocardial perfusion SPECT imaging is based on the detection of defect presence in both stress and rest images. The diagnostic task requires classifying the patients into one of the three categories as shown in Table 2-1 using the rest and stress images.

Table 2-1. Defect status in the rest and stress images

	Normal	Infarct (Fixed defect)	Ischemic (Reversible defect)
Rest	-[a]	+[b]	-
Stress	-	+	+

[a] - denotes that defect is absent

[b] + denotes that defect is present

Ideally, a radiopharmaceutical for MPS should have (1) high first pass extraction fraction, that is myocardial uptake directly proportional to blood flow, (2) slow myocardial washout or clearance, which is affected by regional flow and radiotracer concentrations, (3) high target-to-background ratio, and (4) good myocardial retention and photon flux for optimal imaging [7-9]. The most commonly used agents for MPS are Tl-201 Chloride and Tc-99m sestamibi, and Tc-99m tetrofosmin, which has very similar characteristics and will hereafter be treated as the same as Tc-99m sestamibi. Physical and biological comparisons of Tl-201 chloride and Tc-99m sestamibi are shown in Table 2-2.

Table 2-2. Physical and biological comparison of Tl-201 and Tc -99m sestamibi

Factor	Tc-99m Sestamibi/Tetrofosmin	Tl-201 Chloride
First pass extraction	60%	85%
Myocardial retention	Prolonged	Shorter
Myocardial washout	Very slow	Relatively rapid
Redistribution	Minimal compared to Tl-201	Significant
Myocardial perfusion at high blood flow	Same	Same
Injected activities	15-30 mCi	1-4 mCi
Counting statistics	Better	Fair
Physical half-life	6 h	73 h
Photon energy	140.5KeV	68-82 KeV (abundance), 167.4 (~10%), 135 (~3%)
Radiation dosimetry	0.314 mSv/mCi	6.3 mSv/mCi

2.2.1 MPS acquisition protocols

2.2.1.1 Thalluim-201 Imaging

The most commonly used procedure for Tl-201 imaging involves administering 2.5-4 mCi of Tl-201 prior to peak exercise or at peak pharmacologic vasodilatation [10, 11]. Stress imaging is performed 10-15 minutes after the Tl-201 injection. Delayed rest (redistribution) images are obtained at 3–4 hours after injection. In addition, a rest Tl-201 image at 18-24 hours or after reinjection with an additional booster dose of 1–2 mCi is sometimes used to assess myocardial viability in cases where the standard stress-redistribution imaging shows a fixed or minimally reversible perfusion abnormality.

2.2.1.2 Technetium-99m sestamibi imaging

Imaging of Tc-99m sestamibi can be performed in a one- or two-day sessions [10]. Two-day protocols (stress/rest) are best in terms of taking advantage of the physical properties, pharmacokinetics, and acquisition parameters of Tc-99m labeled agents with the chance of cancelling day-2 study if the stress study on the first day is normal. However, it is inconvenient for patients and camera time and such protocols are thus used relatively infrequently. For one-day protocols, the rest–stress sequence is significantly better than the stress–rest sequence in terms of detecting the reversibility of perfusion defects. Typical injected activities for one- and two-day protocols are shown in Table 2-3 [10].

Table 2-3. Doses of Tc-99m labeled Agents for MPS

Protocol	Dose
One-day rest/stress	8-12mCi/24-36mCi
Two-day stress/rest	15-30mCi/15-30mCi

2.2.1.3 Dual isotope imaging

In MPS dual isotope imaging, Tl-201 and Tc-99m labeled tracers are commonly used for imaging under rest and stress conditions, respectively [10]. Dual-isotope imaging allows for shorter imaging time compared to the one- and two-day Tc-99m sestamibi imaging. However, this comes at a cost of significantly higher radiation dose to the patient [10]. Dual isotope imaging using rest Tl-201 and stress Tc-99m is typically performed by acquiring the initial rest image followed by the stress image. An appealing protocol for dual isotope imaging uses simultaneous acquisition for the rest Tl-201 and stress Tc-99m sestamibi images. A schematic for the dual isotope with separate and simultaneous acquisition protocols is shown in Figure 2-2. Dual isotope simultaneous acquisition (DISA) has some interesting potential benefits over separate dual-isotope protocols. It provides reduced acquisition time, improved patient comfort, and better clinical throughput. Furthermore, perfect registration between rest and stress images is guaranteed. However, crosstalk contamination, where photons of one radionuclide are scattered inside the body or collimator-detector system, lose energy and are detected in the photopeak window of the other isotope, degrades image quality.

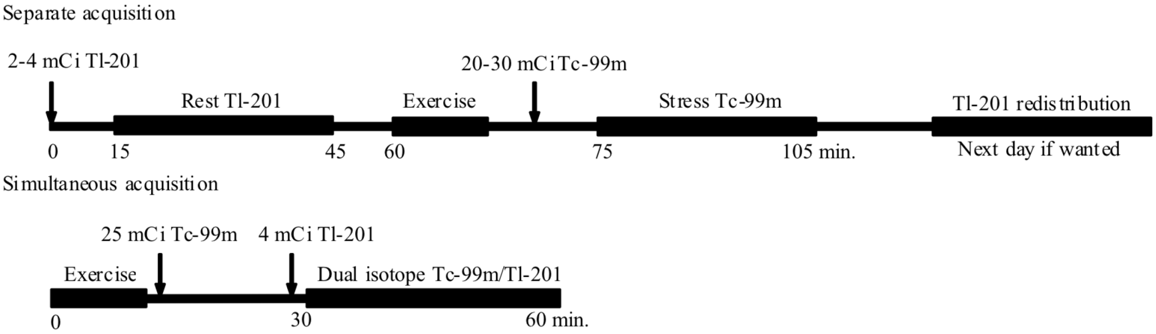

Figure 2-2. Dual isotope imaging with separate and simultaneous acquisition

2.3 Basic components of SPECT systems

Almost all commercially available SPECT systems are based on scintillation cameras (a type of gamma camera that uses scintillation-based detectors and hereafter referred to as such) to detect photons emitted by the radiopharmaceutical as a product of radioactive decay in the patient. One or more gamma cameras, mounted on a rotating gantry, acquire multiple 2D projection images at different projection views to obtain the data needed for tomographic reconstruction [12]. Figure 2-3 shows the major components of a gamma camera. A typical gamma camera consists of a collimator, a large-area scintillation detector [NaI(Tl) crystal], a light guide for optically coupling the photo-multipliers to the crystal and circuits for estimating the interaction position (positioning circuits) and energy (pulse height analyzer) of the gamma camera.

Since the scintillation detectors are incapable of determining the direction of the incoming photons, SPECT system cameras are always used in conjunction with a collimator. Typical collimators consist of a block of lead with many thousands of hexagonal holes drilled in them and which covers the entire crystal surface. Figure 2-4 shows a schematic of a parallel hole collimator with hexagonal holes. In the ideal case, only photons that arrive within the acceptance angle of a collimator hole, determined by the ratio of the collimator hole length and diameter, can reach the detector surface. The collimator serves as a mechanical lens defining the relationship between positions in the image projection plane and directions in space. This directional information is obtained at the cost of a loss of sensitivity and resulting increase in noise in the images. Typical sensitivity of a gamma camera is about 10^{-4}, meaning that 1 out of 10,000 emitted photons, from a source in air, will be detected. Collimator design is the most important factor in determining the system resolution and sensitivity. The choice of collimator parameters such as the hole length (L), hole diameter (H) and septal thickness (S) determine the tradeoff between spatial resolution and noise in SPECT images.

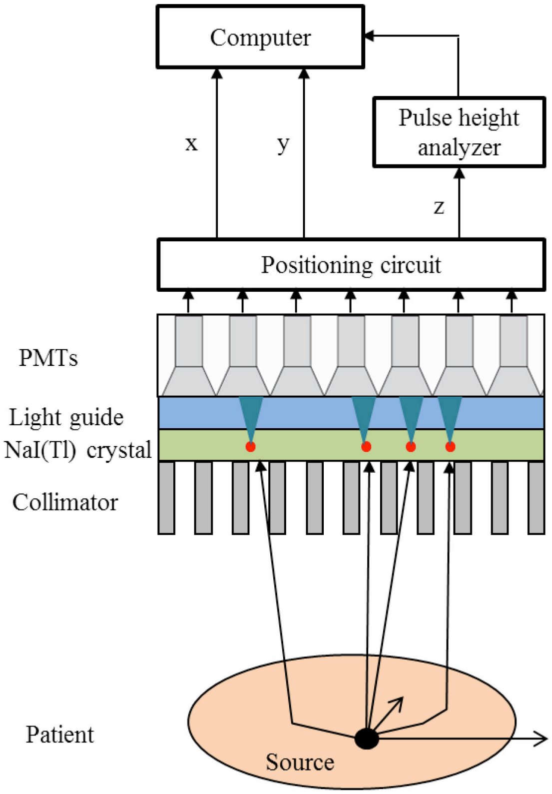

Figure 2-3. Basic components of a gamma camera.

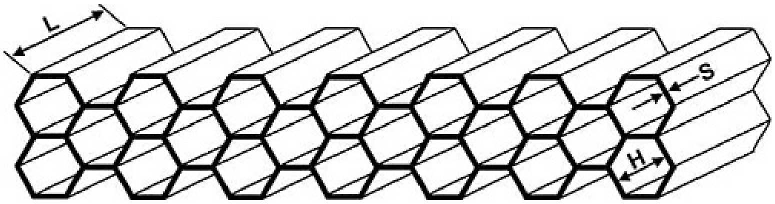

Figure 2-4. A parallel hole collimator showing the hole structure. (Courtesy Nuclear Fields, Des Plaines, IL.)

The scintillation crystal, typically made of sodium iodide with thallium doping [NaI (Tl)] is currently the most commonly used detector in NM. When a photon interacts with the crystal, it deposits energy, which in turn emits visible light (scintillation) photons with intensity proportional to the energy deposited. The scintillation light is emitted isotropically and some of it passes through the glass light guide and onto an array of photomultiplier tubes (PMT) which are in good optical contact with the light guides [12, 13].

The PMT is a vacuum tube that consists of a photosensitive front surface (photocathode), anode and a series of dynodes. The role of the photocathode is to emit photoelectrons when visible light impinges on it, where the number of emitted photoelectrons is proportional to the intensity of the incident visible light. The electrons are then accelerated to the first dynode and successively multiplied at each dynode resulting in a large increase in the number of electrons reaching the anode (the final dynode). The output of each PMT, in the form of electric current, is proportional to the amount of light that struck the photocathode and is inversely related to the distance between the center of that PMT and the interaction site [12].

The pulses from the PMTs are then processed by a series of electronic circuits including a preamplifier, pulse-shaping amplifier, pulse-height analyzer and positioning circuits to estimate the photon energy and interaction site [12]. The role of the pulse-height analyzer is to estimate the amplitudes of the amplifier output pulses and measure the energy of the detected photon. The camera can then selectively count only those events within a certain energy range. This is used to discriminate between scattered and unscattered photons. Energy discrimination is important because scattered photons lose energy and change their direction during scattering so they carry false information about their point of origin, thus degrade image contrast. Positioning circuits analyze the PMT outputs to estimate the position of the detected photon. However, there is an uncertainty in position and energy estimation due to the statistical variation in the emission and collection of photons that result in quantum noise distribution of scintillation photons and thus imprecision in position and energy information [12]. These uncertainties are responsible for the intrinsic spatial and energy resolution of the camera, respectively. The energy and position information are then analyzed by a computer where 2D projections of the 3D activity distribution inside the body are formed and stored. The 2D projections are then used by a reconstruction algorithm to obtain images of the activity inside the body.

2.4 Physics of image formation process

Figure 2-5 shows different types of photons interactions that may occur inside the body or collimator-detector system. Photons are emitted isotropically from each point throughout the body in proportion to the activity at that point. Many of these photons (event P.1) escape from the patient in directions away from the detector. It is desirable to detect photons that escape from the patient without interaction with the intervening tissues and are perpendicular to (event P.3) or within an acceptance angle (event P.4) of the collimator holes and deposit all of their energy in the NaI(Tl) crystal at a single location. We call these photons as primary photons. These photons provide correct directional information about their origin inside the body. However, due to interactions inside the body and collimator-detector system, a non-negligible number of photons will be detected that provide false positional information and thus affect the contrast and resolution of SPECT images. Inside the body, photons may be absorbed (P.2) and never reach the detector, or scatter and change their direction (P.5 and P.6) inside the patient and absorbed in the crystal. In addition to the chance that photons may interact inside the body, it may also interact with the collimator and reach the crystal. Photons could possibly scatter (event C.1) or penetrate (event C.2) the septa and absorbed by the crystal. Photons absorbed in the collimator may also result in the emission of characteristic Pb- x-rays (C.3). This happens when high-energy photons are absorbed during a photoelectric interaction with a Pb atom in the collimator septa resulting in ejection of an inner shell atom and the atom is left in an excited state. To return to ground state, outer shell electrons fall into the vacancy in the inner shell, emitting characteristic x-rays with energies equal to the difference between the binding energies of the of the outer and inner shell electrons. These photons can be detected and result in degraded image quality. In this section, we will introduce the major image-degrading factors including attenuation, scatter, statistical noise and collimator-detector response. Accordingly, compensating for these factors is essential and results in improved quantification and better performance on a variety of tasks.

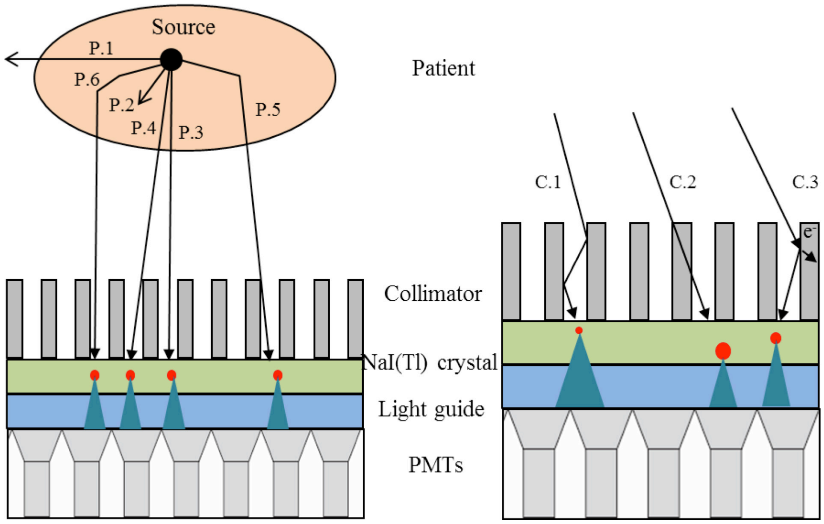

Figure 2-5. Illustration of the different types of interactions inside the body (left) and the collimator-detector system (right) and detected by a gamma camera.

2.4.1 Attenuation and scatter

Attenuation is a process that is caused by the interaction of photons with the body. When a beam of photons passes through the body, there is a probability that it will interact with the intervening tissues. The probability and mechanism of interaction depend on the photon energy, composition of tissues and the distance the photon travels through the body to reach the detector. Given the energies of SPECT photons (140 keV for Tc-99m) and the material properties of the body, which is generally similar to water, the two main mechanisms by which photons interact with tissues are (1) photoelectric absorption (event P.2) and (2) Compton scattering (events P.5 and P.6). The photoelectric effect occurs when a photon interacts with an inner shell electron, causing the ejection of the electron from the atom. The energy of the incident photon is transferred to the electron, called a photoelectron, and the photon is completely absorbed by the atom. Photoelectric absorption results in a significant depth-dependent reduction in the number of detected primary counts [12].

In Compton scattering, a photon interacts with a free electron. Since the energies of the gamma rays are so high compared to the atomic energy levels of atoms in the body, the atomic electrons can, for this purpose, be considered free. As a result of the interaction, some of the incident photon’s energy is transferred to the electron. Moreover, the photon, changes direction and continues with reduced energy. The more energy the photon loses, the larger the scattering angle is. The scattered photon may undergo further scatter, photoelectric absorption or exit the body, pass through the collimator and be detected. If detected, these photons give false information about their original site of emission and thus result in poor contrast SPECT images. Since the scattered photon loses some of its energy during scattering, it will produce a smaller signal in the PMTs and thus can be rejected by proper setting of acquisition energy windows to reject lower energy photons.

An ideal and perfect detector, i.e. one that has a 0% energy resolution, would detect only primary photons. The finite energy resolutions of NaI(Tl) and Cd(Zn)Te (CZT) detectors are directly responsible for the inclusion of scattered radiation in the projection data. In order to include a large fraction of the primary photons, one has to increase the width of the energy window in proportion to the energy resolution full width at half maximum (FWHM), with the cost that more scattered radiation is also detected. Thus, when performing the transition from an ideal to a real detector, one is forced to include an increasing amount of scattered radiation. In order to mitigate the effects of scattered photons, in addition to the energy discrimination methods, a variety of scatter compensation techniques have been proposed [14-20].

2.4.2 Collimator-detector blurring

Ideally the collimator would only allow photons to pass through when their incident direction is perpendicular to the collimator. However, because of the finite hole size and the fact that the collimator is not completely opaque to gamma radiation, there is some blurring of the resulting image. Collimator blurring is due to the detection of photons that arrive with non-perpendicular directions and pass through the collimator holes. The intrinsic resolution of the detector contributes additional blurring. These effects can be characterized by the collimator-detector response (CDR).

The CDR function (CDRF) describes the probability that photons emitted from a point source in air will be detected at some point in the detection plane. The CDRF can be decomposed into 4 components that affect the quality of SPECT images. The intrinsic response function (IRF) describes the response of the detector to a perfectly collimated point source; its integral represents the efficiency of the detector. The IRF is determined by the uncertainty in position estimation, which, for a scintillation camera, is due to the statistical variation of the estimated interaction position in the crystal. For such cameras the intrinsic resolution can be well modeled as a Gaussian function and is typically assumed to be invariant across the detector surface.

The other 3 components of the CDRF depend on the collimator characteristics and the photon energy. This includes the geometric (GRF), septal penetration (SPRF) and septal scatter (SSRF) response functions, which describe the detection probabilities of photons emitted from a point source that pass through the collimator holes, penetrate through the septa, or scatter in the septa, respectively. The geometric response largely determines the FWHM of the CDRF. The relative importance of these effects largely depends on the collimator parameters and the energy of the incident photons. For example, a collimator with a relatively small aspect ratio, defined as the ratio of hole length to the hole size, septal scatter and penetration are non-negligible factor and potentially important. Accurate modeling of the CDRF can result in improved image resolution and contrast and thus can improve the quantitative accuracy for small organs and objects of interest such as tumors [21-23].

2.4.3 Statistical noise

The imaging process includes randomness in the radioactivity distribution, emission of photons in radioactive decay, interaction of photons in the body and collimator-detector system, generation and collection of scintillation photons, absorption of scintillation photons by the PMT cathode, and the generation and collection of photoelectrons in the PMT. These sources of randomness result in randomness in the raw measurements, in the form of quantum noise, acquired by SPECT imaging system. The randomness in the projection data can be treated as a Poisson random process. Thus, the number of detected photons per unit area is a Poisson random variable. For a Poisson random variable, the mean is equal to the variance. The signal to noise ratio (SNR) of the mean counts in in the image is given by [13]:

$$SNR = \frac{\overline{N}}{\sqrt{\overline{N}}} = \sqrt{\overline{N}}, \tag{2.1}$$

where $\overline{N}$ is the mean total number of acquired photons.

Therefore, this SNR is directly proportional to the number of acquired photons and as a result the noise in SPECT projection data decreases with increasing the number of acquired photons.

2.5 Imaging chain

An object to be imaged can be described as a function in a three-dimensional Euclidean space as. $f(x,y,z)$ In SPECT imaging, $f(x,y,z)$ refers to the density of a radioactive tracer. The continuous object can be written as a vector $\mathbf{f} = [f_1, f_2, f_3 \ldots f_N] \in \mathbb{R}^N$ in the Hilbert space of square-integrable functions [24]. We can model the imaging system using the linear equation:

$$\mathbf{g} = \mathbf{Hf} + \mathbf{n}, \tag{2.2}$$

where, $\mathbf{H} \in \mathbb{R}^{MxN}$ the imaging operator, is a continuous-to-discrete projection operator that maps the object $\mathbf{f}$ to the projection space, $\mathbf{n} \in \mathbb{R}^{M}$ is the (Poisson distributed) measurement noise and $\mathbf{g} \in \mathbb{R}^{M}$ is the noisy projection data returned by the imaging system. The operator $\mathbf{H}$ is determined by the physical characteristics of the image formation process, including all physical processes and factors that degrade image quality (e.g., finite energy resolution, scatter, attenuation and CDR)

To produce images that depict the activity distribution inside the body, the projection data $\mathbf{g}$ are often further processed using a tomographic reconstruction algorithm, $\mathbf{O}$ which produces an estimate $\hat{\mathbf{f}}$ of the original object $\mathbf{f}$ using the equation:

$$\hat{\mathbf{f}} = \mathbf{O}\mathbf{g}. \tag{2.3}$$

2.6 Reconstruction methods

SPECT 3D reconstruction problem can be treated as solving the inverse problem of estimating the 3D activity distribution, $\hat{\mathbf{f}}$ from a set of 2D projection data, $\mathbf{g}$ as described in (2.3). There are 2 major classes of reconstruction algorithms used in reconstructing SPECT images: analytical and iterative methods. Filtered backprojection (FBP) is an example of classical analytical methods. FBP and is a very commonly used algorithm due to its speed and ease of implementation. However, FBP does not take into account the physical characteristics of the image formation process and image degrading factors such as attenuation, scatter, CDR modeling and statistical noise. This can lead to artifacts in SPECT images, which would certainly impact the diagnostic accuracy of readers interpreting them.

Iterative reconstruction methods have a number of potential advantages over analytical methods such as the possibility of incorporating complex models of the underlying physics of the imaging process, models for noise in the projection data, and methods to control noise into the reconstruction process. State-of-the-art SPECT reconstruction methods are statistical iterative reconstruction methods such as the maximum likelihood-expectation maximization (ML-EM) method [25, 26] and its variation the ordered subsets-expectation maximization (OS-EM) method [27]. Statistical iterative reconstruction methods have two major components: the statistical criterion or objective function (e.g. expectation maximization (EM), or the ordered subsets version of the EM algorithm) and the iterative criterion (e.g. maximum likelihood).

The ML-EM method uses EM algorithm to iteratively approach the ML solution. The update equation at iteration $n+1$ can be written in a matrix-vector form as:

$$\hat{\mathbf{f}}^{(n+1)} = \frac{\hat{\mathbf{f}}^{(n)}}{\mathbf{H}^T\mathbf{e}} . \left(\mathbf{H}^T . \frac{\mathbf{g}}{\mathbf{H}\hat{\mathbf{f}}^{(n)}} \right), \tag{2.4}$$

where $\mathbf{e}$ is an *N*-D vector with all elements equal to 1. Note that in (2.4), vector-vector multiplication and division are element-by-element processes and matrix-vector multiplication is still applied using the conventional way.

The implementation of ML-EM can be described as follow. An initial estimate of the activity distribution in the object (usually an image with uniform intensity restricted to the region that contains the object) is projected using a forward model of the imaging process including attenuation, scatter, CDR and noise. The error between the estimated and the measured projection data is calculated. The error term is then used to update the estimate of the activity distribution. The update process requires backprojecting the error term to the image space by multiplying it by the transpose of the projection matrix $\mathbf{H}$. The projection-backprojection-update process is repeated until some criterion is fulfilled, often as simple as a user-specified number of iterations. Note that the projection matrix $\mathbf{H}$ can incorporate models of all the previously discussed image degrading processes, including attenuation, scatter and distance-dependent CDRF. Thus, the imaging degrading factors are compensated for during the iterative reconstruction process.

Despite the advantages of ML-EM method, it is computationally expensive, primarily because it involves forward and backward projection processes of the full data in each iteration, and thus converges slowly. To accelerate the convergence rate, OS-EM method [27] was proposed. In OS-EM, the backprojection step is only performed using an ordered subset of the projection (e.g., the projection data with 60 views can be grouped into 12 ordered subsets with 5 views in each subset). At each update (called sub-iteration and is equal to the number of subsets), a different subset of the projection data is used. A full iteration of OS-EM is completed after looping through all the subsets. The estimated image is updated k times (number of subsets) in one iteration of OS-EM compared to one time in an ML-EM iteration. Therefore, OS-EM converges faster than ML-EM by a factor of the number of subsets. While it has been shown to be of great practical value and give results very similar to ML-EM [28], OS-EM has relatively weak theoretical basis and its convergence properties have not been well understood.

2.7 Task-based image quality assessment

Often research in medical imaging dealing with the design of imaging systems instrumentation, and the optimization of acquisition parameters and evaluation of reconstruction methods aims at producing “better” images. It is thus important to define what is meant by a “better” image. Several approaches have been proposed to assess the image quality, including subjective assessments, fidelity measures, and information-theoretic assessments [24, 29, 30]. However, these approaches do not take into consideration the task that will be performed with the image. Task-based assessment of image quality is an approach to evaluate image quality based on the performance of an observer on a specific diagnostic task of practical interests. The four key elements of task-based assessment are: a patient population being imaged, a task of interest, an observer who performs the task and a figure of merit (FOM) that quantifies the performance of the observer on the task [24]. We should note that observers might act on the raw image data, $\mathbf{g}$ reconstructed images, $\hat{\mathbf{f}}$ or features extracted from images. In the following sections, we use the notation for image data $\mathbf{g}$, as a shorthand notation for any of these.

2.7.1 Object and system models

Ultimately, we would like to use patient data to optimize system design, acquisition parameters and reconstruction methods. However, it is impractical to optimize the large number of instrumentation and acquisition parameters with human studies due to radiation concerns and difficulty in obtaining true perfusion status and patient data acquired using various kinds of parameters, which is either too expensive, time consuming or both. Computer simulations are a practical alternative. Nevertheless, to provide clinically relevant optimization of SPECT imaging system parameters, it is important that the object models be as realistic as possible and include anatomical and tracer uptake variability that models a clinical population. Many studies have modeled background variability using statistically defined lumps [31-34]. This lumpy model has been primarily adopted for mathematical convenience. However, for cardiac SPECT imaging, lumpy backgrounds are not a very suitable background model. In this dissertation, we designed and developed a realistic digital phantom population based on the 3D eXtended Cardiac Torso (XCAT) phantom [35], that provides an accurate, realistic and flexible model of human anatomy by using non-uniform rational B-splines NURBS surfaces. The 3D XCAT phantom models whole body male and female anatomies based on data from the 3D Visible Human Male and Female anatomical imaging data sets from the National Library of Medicine (NLM).

In addition to accurately and realistically modeling patient populations, an accurate and realistic simulation of the imaging process is also essential. Monte Carlo (MC) methods are the gold standard for modeling photon transport, and have been extensively used in the field of nuclear medicine and emission tomography to model the various physical processes and instrumentation. However, they are computationally expensive especially for studies that involve populations of phantoms, and full MC simulation of the collimator-detector system. In this dissertation, we developed and used several techniques to efficiently simulate realistic projections for the phantom population modeled using MC simulation methods. A full description of the phantom population and the projection database is given in Chapter 3.

2.7.2 Tasks

Medical images are typically used to perform a relevant task. The clinical tasks of interest can be categorized as parameter estimation or classification tasks. In estimation tasks, the goal is to quantify some parameter of interest from the image. Examples of estimation tasks include determination of patient's cardiac ejection fraction, which is the fraction of blood pumped out of the left ventricle during a heart cycle, the physical extent of a perfusion defect, and estimating uptake in a particular organ or region of interest. For classification task, the goal is to determine to which class, among a finite number of classes, the imaged object belongs. In the context of MPS imaging, the task might be perfusion defect detection, or the classification of a perfusion defect into a particular class such as classifying the patient as having a fixed or reversible defect. In this dissertation, we are interested in the tasks described in the following sections.

2.7.2.1 Binary defect detection task

A binary defect detection task is a special case of general classification tasks where there are only two underlying hypotheses or classes from which the data might have been drawn. In a binary detection task, the goal is to determine whether or not a signal (i.e. perfusion defect) is present based on the measured data $\mathbf{g}$. The object $\mathbf{f}$ can be thought of as being comprised of a random background, $\mathbf{f}_b$ and a signal, $\mathbf{f}_s$ if a signal is present. The background and signal projection images can then be expressed as $\mathbf{b} = \mathbf{H}\mathbf{f}_b$ and $\mathbf{s} = \mathbf{H}\mathbf{f}_s$ respectively. The two hypotheses to be tested can be represented mathematically as:

$$H_0 : \mathbf{g} = \mathbf{b} + \mathbf{n},$$

$$H_1 : \mathbf{g} = \mathbf{b} + \mathbf{s} + \mathbf{n},$$

where $\mathbf{g}$, $\mathbf{b}$, $\mathbf{s}$ and $\mathbf{n} \in \mathbb{R}^M$ are the noisy projection, background, defect and noise data vectors, respectively and the hypotheses H_0 **and** H_1 mean signal -absent and -present, respectively.

2.7.2.2 Three-class detection task

In dual isotope imaging with simultaneous acquisition, task-based optimization of acquisition parameters requires taking into account the 3-class nature of the diagnostic task because there is an inverse relationship between image qualities for the rest and stress images. For example, if the Tl-201 injected activity is fixed, then decreasing the Tc-99m injected activity decreases the crosstalk contamination of the rest image, and thus improves the rest image quality at the expense of noisier stress images; similarly, increasing the Tc-99m injected activity improves the stress image quality (by reducing noise) at the expenses of more crosstalk contamination in the rest images.

For the 3-class MPS detection task, the observer is required to classify the patient as being normal or having a fixed or reversible perfusion defect. The 3-class hypotheses to be tested can be represented mathematically by:

$$\begin{aligned} H_N &: \mathbf{g} = \mathbf{b} + \mathbf{n}, \\ H_F &: \mathbf{g} = \mathbf{b} + \mathbf{s}_F + \mathbf{n}, \\ H_R &: \mathbf{g} = \mathbf{b} + \mathbf{s}_R + \mathbf{n}, \end{aligned}$$

where $\mathbf{g}$, $\mathbf{b}$, $\mathbf{s}_F$, $\mathbf{s}_R$ and $\mathbf{n}$ $\in \mathbb{R}^M$ are the noisy projection, background, fixed defect, reversible defect and noise vectors, respectively and the hypotheses H_N, H_F **and** H_R mean signal absent, fixed and reversible defects present, respectively. Note that in this case the data vector includes both the rest and stress image data.

2.7.2.3 Joint defect detection and localization task

For the joint detection and localization task, the observer is required to jointly detect and localize a defect among a set of L possible defect locations. The task can be treated as an L+1 decision task where L is the (finite) number of defect locations. When L equals 1, the problem becomes the binary detection task described above. The L + 1 hypotheses to be tested can be represented mathematically as:

$$H_0 : \mathbf{g} = \mathbf{b} + \mathbf{n}$$

$$H_j : \mathbf{g} = \mathbf{b} + \mathbf{s}_j + \mathbf{n},$$

where hypothesis H_j means that the defect $\mathbf{s}_j$ is present at location j and $j = 1, 2 \ldots L$.

2.7.3 Observers

Observers come in many forms; the most obvious is human observer. Human observers in medical imaging are usually trained professionals such as radiologists or cardiologists. A major limitation of human observer studies is that human observers only evaluate a limited number of images for each parameter setting, resulting in low statistical power. Moreover, human observer performance suffers from both within and between -observer variations [36]. Therefore, assessing image quality using human observer studies is time consuming and expensive. To overcome these difficulties and limitations, model observers have been proposed to optimize imaging systems. Model observers are mathematical operators, either linear or non-linear, that act on an image to extract some information and return a test statistic or decision variable, which is then used to make a decision. Model observers fall into two categories: ideal observers, which make use of all the available data to generate the best possible diagnosis; and anthropomorphic observers, which are used to emulate human observer performance. In this dissertation, we are interested in the observers described in the following sections.

2.7.3.1 The Ideal Observer (IO)

The ideal observer (IO) is defined as the observer that performs the task using the data in the optimal way, i.e. its performance is better than or equivalent to any other observer. The fact that it is ideal does not mean that it does not make wrong decisions. However, it is ideal in the sense that it makes optimal use of the available information. For a binary detection task it turns out that IO uses the ratio of signal present and absent statistical likelihoods, known as the likelihood ratio (LR), or any monotonic transformation of the LR, as the test statistic or decision variable [24]. The likelihood ratio can then be written as:

$$t(\mathbf{g}) = \Lambda_{H_0,H_1}(\mathbf{g}) = \frac{pr(\mathbf{g}\,|\,H_1)}{pr(\mathbf{g}\,|\,H_0)}. \tag{2.5}$$

For the three-class task, the IO uses a pair of log-likelihood ratios as decision variables, defined as,

$$t_1(\mathbf{g}) = \log\Lambda_{N,R}(\mathbf{g}) = \frac{pr(\mathbf{g}\,|\,H_R)}{pr(\mathbf{g}\,|\,H_N)}, \tag{2.6}$$

$$t_2(\mathbf{g}) = \log\Lambda_{R,F}(\mathbf{g}) = \frac{pr(\mathbf{g}\,|\,H_F)}{pr(\mathbf{g}\,|\,H_R)}. \tag{2.7}$$

The IO decision variable for the joint detection and localization task, $t_{loc}(\mathbf{g})$ as derived in [37], can be written as,

$$t_{loc}(\mathbf{g}) = \max_{j\in\{1,2,\ldots L\}} pr(j)\Lambda_{H_0,H_j}(\mathbf{g}), \tag{2.8}$$

$$l(\mathbf{g}) = \arg\max_{j\in\{1,2,\ldots L\}} pr(j)\Lambda(\mathbf{g}\,|\,\mathbf{b},\mathbf{s}_j), \tag{2.9}$$

where $pr(j)$ is the prior probability that a perfusion defect is present at location j and $l(\mathbf{g})$ is the location assigned to the defect.

Due to its optimality, it is often assumed desirable to optimize instrumentation and acquisition parameters using the IO performance operating on projection data so that maximum information about the task is contained in the measured raw data. The role of the subsequent reconstruction, regularization, and compensation steps can then be conceptualized as matching the information in the raw data for optimal performance by a human observer.

Using the IO to optimize instrumentation and acquisition parameters is theoretically appealing. It requires only calculating the decision variables, i.e. likelihood ratios, for the different task as defined above. However, it has not been rigorously applied to real imaging tasks due to the technical difficulty of estimating the performance for cases of realistic background variability arising from variations in patient anatomy and uptake. Typically, application of the IO has been limited to cases where the background and signal models were relatively simple [38-40]. To overcome this limitation, we modified and applied previously developed methods based on Markov Chain Monte Carlo (MCMC) techniques [33, 34, 41] to estimate the IO test statistic for realistic and general backgrounds and signal models. More details on this are given in Chapter 4.

2.7.3.2 The Ideal Observer with Model Mismatch (IO-MM)

Another difficulty in evaluating and optimizing imaging systems using the IO is that since the IO has full knowledge of all the statistical information about the background and signal, it implicitly has a perfect model of the image formation process. However, real reconstruction and compensation algorithms do not perfectly model the image formation process. The difference between the true, complete and accurate model and that used in reconstruction is referred to in the context of this work as model mismatch (MM). This mismatch is one reason why the IO may not always give the same optimum operating parameters as human observer when operating on images reconstructed with imperfect or incomplete system models. To account for the degradation of the observer performance due to the model-mismatch, we developed an observer that explicitly includes model-mismatch in the IO [3, 4]. This observer was termed the IO-MM, where MM stands for the model-mismatch. The IO-MM still uses the LR as the test statistic, but in the estimation of the LR it uses an approximate model of the image formation process instead of the true one. This observer is described in more detail in Chapters 5 and 6

2.7.3.3 The Hotelling Observer (HO) and Channelized Hotelling Observer (CHO)

The IO uses the likelihood ratio (LR) as the test statistic, which is a non-linear function of the data $\mathbf{g}$. This is usually mathematically intractable and hard to compute. It is thus desirable to consider observers that use linear discriminant functions and therefore require only the knowledge of the first and second order statistics of the data. A general linear test statistic can be written as:

$$t(\mathbf{g}) = \mathbf{w}^t \mathbf{g} \tag{2.10}$$

where $\mathbf{w} \in \mathbb{R}^M$ is a linear template that is applied to the image $\mathbf{g} \in \mathbb{R}^M$ to obtain a scalar test statistic $t(\mathbf{g})$.

In the context of binary detection task, the Hotelling Observer (HO) is the linear observer that maximizes the signal-to-noise ratio (SNR), a measure of class separability, defined as [24]:

$$SNR = \frac{<\mathbf{t}(\mathbf{g})>_{H_1} - <\mathbf{t}(\mathbf{g})>_{H_0}}{\sqrt{\frac{1}{2}\left(\sigma_{H_1}^2 + \sigma_{H_0}^2\right)}} \tag{2.11}$$

where $<\mathbf{t}(\mathbf{g})>_{H_i}$ and $\sigma_{H_i}^2$ $(i = 0,1)$ are the mean and variance of the test statistics under hypothesis H_i. The Hotelling template takes the form [42]:

$$\boldsymbol{w}_{\boldsymbol{Hot}} = \boldsymbol{K}_{\mathbf{g}}^{-1}\Delta\overline{\mathbf{g}}, \tag{2.12}$$

$$\boldsymbol{K}_{\mathbf{g}} = \left[\frac{1}{2}(\boldsymbol{K}_0 + \boldsymbol{K}_1)\right], \tag{2.13}$$

where K_i (i=1 and 2) is the covariance matrix of the image vector $\mathbf{g}$ under the hypothesis H_i and $\Delta\overline{\mathbf{g}}$ is the difference in the means of the image data vectors under the two hypotheses. The SNR can be computed as:

$$SNR^2 = \Delta\overline{\mathbf{g}}^T K_{\mathbf{g}}^{-1}\Delta\overline{\mathbf{g}}. \tag{2.14}$$

Calculating the HO test statistic, and thus the SNR, requires knowledge of the first and second order statistics of the image data. The difference in the means $\Delta\overline{\mathbf{g}}$ is easy to compute. However, the covariance matrix K_{g} may be difficult to estimate because of its size, typically M^2 elements. For example, if a planar imaging system produces image data that have 128 × 128 elements, then $M = 128^2$ and K_{g} is a $128^2 \times 128^2$ matrix. For a 3D tomographic system, the size in each dimension is increased by the number of viewing angles and reconstructed slices, respectively. Note that calculating the HO template requires inverting this large matrix. This is both computationally challenging and makes the result sensitive to noise in the covariance matrix, especially if the covariance is estimated from data samples.

The addition of a channel mechanism to the IO or HO was originally proposed to partially model the way in which the human-visual system processes images [43]. When visually processing an image, humans are sensitive only to the total power in a series of frequency bands or channels rather than to individual frequencies (i.e., infinitesimally small frequency bands). An example of an anthropomorphic channel, and the one used in this work, is a set of difference of mesa channels. Figure 2-6 shows four non-overlapping difference-of-mesa frequency channels with successively doubling widths and a starting frequency of 0.5 pixel^{-1}.

The application of channels involves taking the dot product of the image data $\mathbf{g} \in \mathbb{R}^M$ with a series of $L\ (L << M)$ channel template images, such as the ones shown in Figure 2-6, resulting in one scalar response for each channel image, i.e.

$$\nu = \mathbf{Tg} \tag{2.15}$$

where $\nu \in \mathbb{R}^L$ is the channel output for image $\mathbf{g} \in \mathbb{R}^M$ and $T \in \mathbb{R}^{LxM}$ is the channel operator. The HO template and test statistics can then be computed using the channel outputs $\nu \in \mathbb{R}^L$ instead of the image data $\mathbf{g} \in \mathbb{R}^M$. Accordingly, many of the computational difficulties associated with the estimation and inversion of the covariance matrix $K_{\mathbf{g}}$ can be avoided when applying the HO on the lower dimensional channel output data $\nu \in \mathbb{R}^L$.

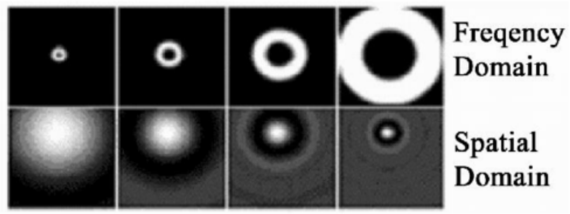

Figure 2-6. Four band-pass frequency-domain channels and their spatial-domain counterparts shifted to a specific signal centroid location.

The CHO has shown good agreement with human observers in a variety of clinical applications and tasks [44-52]. The CHO is typically applied to reconstructed images. The quality of reconstructed images depends on regularization methods, such as low pass filtering, applied to the images to control noise. It is only meaningful to compare methods using regularization parameters optimized for each method under comparison. However, optimization of regularization parameters is very computationally intensive because of the need to reconstruct many images and assess the quality of images obtained with many different values of regularization parameters. As a result, as mentioned above, it is highly desirable, if possible, to optimize instrumentation and acquisition parameters using the Ideal Observer applied to projection domain images.

2.7.4 Figures-of-merit

2.7.4.1 Binary defect detection task

In a binary decision task, the observer decides that an image $\mathbf{g}$ contains a signal (i.e. perfusion defect) if the test statistic $t(\mathbf{g})$ is greater than a threshold α. However, due to the inherent randomness in the image data, the test statistics under the two hypotheses for an ensemble of known signal-present and signal-absent images will be distributed as shown in Figure 2-7, with some degree of overlap between the distributions. This implies that, for each threshold α, some normal patients may be classified as having perfusion defects and vice versa.

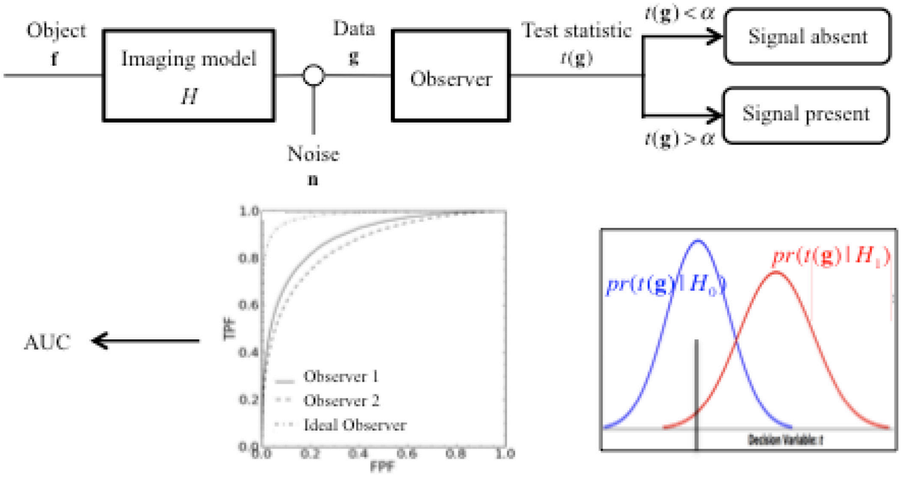

Figure 2-7. A flow chart of a binary decision task including the model of the image formation, the application of the observer and the ROC analysis methodology.

In a clinical setting, we are interested in two parameters: the sensitivity and specificity, also known as the true positive fraction (TPF) and the true negative fraction (TNF), defined as the fraction of patients who were correctly diagnosed as abnormal and normal, respectively. One possible FOM to evaluate the observer performance is the diagnostic accuracy, defined as the total number of patients who were diagnosed correctly. In order to maximize the diagnostic accuracy, both the sensitivity and specificity must be maximized. Therefore the threshold α must be chosen to balance between the sensitivity and specificity. Note that a lower threshold implies that more patients will be classified as abnormal, thus increasing the sensitivity but decreasing specificity (Figure 2-7). If the threshold value is large, more patients will be classified as normal and thus increasing specificity with the cost of decreased sensitivity. However, the choice of the threshold is affected by various factors, which include skill and training of the observer, disease prevalence, and prior estimate of the cost versus benefit of the decisions.

An alternative way to evaluate the performance of the observer on a diagnostic task, in a way that is independent of prevalence, the main complaint lodged against the use of accuracy, is using Receiver Operating Characteristics (ROC) curves. An ROC curve can be constructed by sweeping the decision variable α across the decision variable plane and calculating the true positive fraction (TPF(α)) and the false positive fraction (FPF(α)), that is one minus the specificity. The ROC curve is a parametric plot of TPF(α) vs. FPF(α). The area under the ROC curve (AUC) serves as a figure-of-merit for task performance. In Figure 2-7, the IO outperforms observers 1, and observer 1 outperforms observer 2. We note that the IO is an observer that provides the largest true positive fraction for any given false positive fraction.

2.7.4.2 Three-class detection task

Three-class ROC analysis is the extension of ROC analysis to the case of classification into three diagnostic classes. In the 3-class task, the observer uses a pair of log likelihood ratios. The 3-class ROC surface is obtained by sweeping the decision structure across the log-likelihood decision plane as shown in Figure 2-8 (a) and calculating the triplet (T1F, T2F and T3F), defined as the true class fractions, for every position of the critical point, i.e., the intersection of the 3 rays in the decision structure. The volume under the 3-class ROC surface (Figure 2-8 (b) (VUS) serves as a FOM for 3-class task performance.

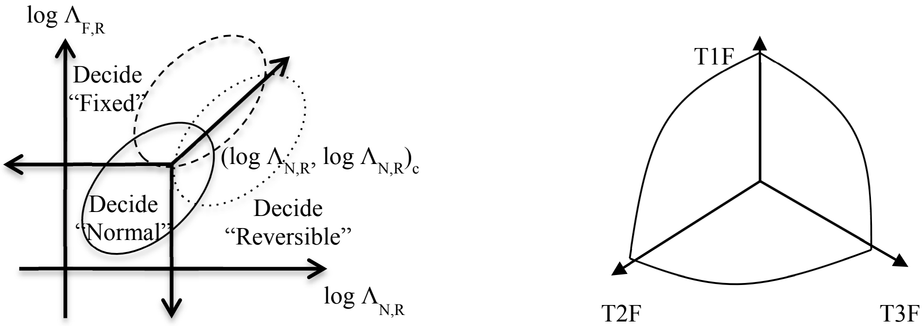

Figure 2-8.(a) Log likelihood ratio decision plane and the decision structure for the practical 3-class ROC analysis method. (b) Sample 3-class ROC surface.

2.7.4.3 Joint perfusion detection and localization task

In the joint detection and localization task, the observer is required to jointly detect and localize a defect among a set of L possible defect locations. A curve similar to the ROC curve, called the localization ROC curve (LROC) (Figure 2-9), can be constructed by calculating the percent correct localization (PCL), defined as the probability of simultaneously detecting a defect (if present) and localizing it, and FPF pair for each threshold value. The task performance measure for this joint task is the area under the LROC curve [37, 53].

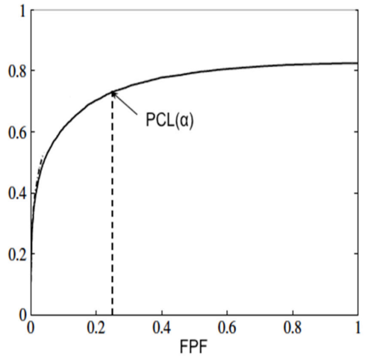

Figure 2-9. Sample LROC curve.

3. Design of a digital phantom population for myocardial perfusion SPECT imaging research

3.1 Introduction

Myocardial perfusion SPECT (MPS) has been shown to be an accurate and useful non-invasive diagnostic imaging technique for the detection and functional characterization of coronary artery disease, and is one of the most commonly performed nuclear medicine imaging procedures. While there have been advances in cardiac imaging with modalities such as MRI and CT angiography, MPS continues to be a useful, widely used, and cost-effective diagnostic test to assess perfusion status.

Recent advances in MPS technology aim at reducing radiation exposure, improving image quality, increasing patient comfort and increasing clinical throughput. This includes the use of cameras with novel detector materials (including solid-state detectors such as cadmium zinc telluride [CZT]), novel camera geometries and collimator designs, new reconstruction and processing methods, and protocols that allow reduced imaging time. Of potential appeal is the use of a simultaneous stress Tc-99m/rest Tl-201 dual isotope cardiac SPECT protocol, which would allow for reduction in imaging time and associated increase in patient comfort, more accurate registration of the two scans, and an increase in clinical throughput.

In order to fully exploit these advances, it is essential to have tools that can be used for MPS system optimization and evaluation. However, due to radiation concerns and difficulty in obtaining true perfusion status, it is impractical to optimize the large number of imaging parameters with human or animal studies on clinically relevant tasks. It is equally impractical to perform optimization studies using physical phantoms, since they cannot realistically duplicate the organ shapes and spatial relationships of patients, and it is prohibitively expensive to fabricate populations of physical phantoms modeling a realistic range of patient sizes, variations, and deformations.

Computer generated digital phantoms offer a practical alternative approach to evaluate, compare, and improve medical imaging devices and techniques. In order for digital phantoms to reach their full potential as a research and evaluation tool, it is essential for them to be as anatomically realistic as possible. Otherwise, studies using them would not be indicative of what would occur in live patients.

The three-dimensional (3D) eXtended CArdiac Torso (XCAT) phantom, as well as its predecessor, the Nurbs-based CArdiac Torso (NCAT) phantom, have been widely used for medical imaging simulation [35, 54-59]. The 3D XCAT and NCAT phantoms provide an accurate, realistic and flexible model of the human anatomy by using non-uniform rational B-splines NURBS surfaces. The XCAT models whole body male and female anatomies based on the 3D Visible Human Male and Female anatomical imaging data sets from the National Library of Medicine (NLM). With its basis upon human data and the inherent flexibility of the NURBS surfaces that allows transformation to model varying patient anatomy, the XCAT is capable of creating a realistic population of patients of varying anatomy from which to perform myocardial perfusion SPECT imaging research.

In this work, we designed a new adult digital phantom population based on the 3D XCAT phantom. The population consists of fifty-four digital phantoms including variability in gender, body size, heart size and fat level. To realistically model anatomical variability in a way that is clinically relevant, we used anatomical distributions obtained from the Emory Cardiac Database [60]. We chose particular parameters to vary based on those that have the biggest impact on MPS image quality. Of importance, we chose to model specific patient and organ sizes, rather than taking random samples from an assumed normal distribution [47], in order to more uniformly span a range of meaningful patient sizes rather than to model a specific phantom population. Using these specific sizes, it is possible to see if methods fail for certain kinds of patients (e.g., very large or small). It is also possible to explore the dependence of optimal acquisition or reconstruction parameters on patient anatomy. This is potentially useful since it is something that can be observed prior to imaging.

In addition to accurately and realistically modeling patient populations, an accurate and realistic simulation of the imaging process is also essential. However, realistically modeling the imaging process is computationally demanding. We thus used several techniques to efficiently simulate realistic projections of the phantom population.

The first technique was to use an efficient simulation method. Monte Carlo (MC) methods have been extensively used in the field of nuclear medicine and emission tomography to model the various physical processes and instrumentation. A number of MC simulation tools have been developed that offer tradeoffs between simulation accuracy and flexibility on one hand and computation time on the other hand. The Simulation System for Emission Tomography (SimSET) is a widely used package, developed, validated, and maintained by the University of Washington Imaging Research Laboratory, which is specifically designed for the simulation of SPECT and PET using voxelized phantoms [61]. SimSET incorporates variance reduction techniques that are appropriate for nuclear medicine simulations and which greatly increase the simulation efficiency. SimSET models the important physical phenomena, including photoelectric absorption, Compton's scattering and coherent scattering. However, in SimSET, the collimator is not modeled using MC photon tracking, but by an approximate analytical model that neglects physical effects such as photon penetration, x-rays fluorescence, and scatter in the collimator. For some applications, such as dual isotope imaging using Tc-99m and Tl-201, septal Pb x-rays are detected in the Tl-201 photopeak energy window, this fluorescence x-ray component is a non-negligible degrading factor; discarding its effect in the simulation may lead to inaccurate results.

Full MC simulation of the collimator–detector system is computationally expensive and is impractical for the simulation of SPECT data, especially for studies involving populations of phantoms. Song et al [23] developed and implemented a fast and accurate method to model collimator and detector effects based on angular response functions (ARFs). The ARF is a function of the incident photon's direction and energy and describes the probability that a photon traveling in a certain direction will interact with the collimator-detector system and be detected in an energy window of interest. The ARF tables are pre-computed using full MC simulations of a point source in air and are used subsequently to model the response of the detection system for a given energy deposition window.

In this work, we used ARF tables in conjunction with the SimSET MC code to efficiently and accurately model the interactions in the patient and collimator-detector system respectively. In this method, the photon interaction inside the phantom is modeled using SimSET. When the photon exits the phantom, its position, direction, and energy are saved to a history file. The history file is then processed by the ARF simulation to model interactions inside the collimator-detector system and the final projection data is generated as shown in Figure 3-1.

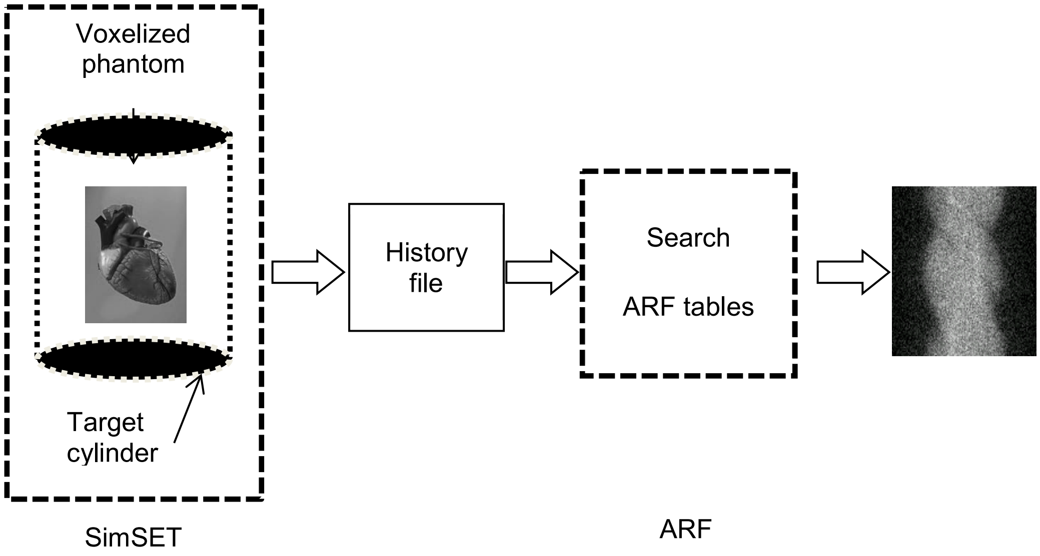

Figure 3-1. Block diagram of the SimSET+ARF simulation.

The combined SimSET+ARF simulation method has been previously validated for various camera systems and a variety of radionuclides. In the original work by Song et al [23], they validated the SimSET+ARF method by comparing the simulated projections with those simulated using full MC simulations using SimSET and MCNP codes [62, 63], a combination that has been validated against experimental measurements. The investigated cases were ones where interactions in the collimator-detector system are important. The SimSET+ARF combination was validated for simulation of Tc-99m/Tl-201 dual isotope cardiac imaging (where Pb x-rays fluorescence is important and the same isotope combination used for this work) and I-123/Tc-99m dual isotope brain imaging (where collimator scatter, septal penetration and partial deposition in the crystal are important interactions). They also validated it for In-111 imaging where septal penetration and scatter are non-negligible and potentially important. They modeled a GE Millennium VG camera system and a GE low-energy high-resolution (LEHR) collimator for Tc-99m/Tl-201 and I-123/Tc-99m dual isotope imaging and a medium-energy general-purpose (MEGP) collimator for In-111 imaging.

He et al. [64] compared the projections of a hollow plastic sphere, filled with 231.62MBq of In-111, inside a cold elliptical phantom filled with water with the projections simulated using SimSET+ARF. They modeled a GE Discovery VH/Hawkeye SPECT/CT system with a 2.54 cm thick crystal and a MEGP collimator. Song et al. [65] validated SimSET+ARF by conducting a similar experiment, but modeled a Philips Precedence SPECT/CT system and a high-energy general-purpose (HEGP) collimator. The results of those experiments showed that the SimSET+ARF method was in good agreement with full MC simulations and physical phantom measurements for the cases studied. It also provided a substantial reduction in the simulation computational time.

As mentioned earlier, SimSET incorporates variance reduction methods to increase the simulation efficiency. Many of these methods involve changing the weight of the simulated photons. As a result, the resulting projections no longer have Poisson-distributed noise. For this reason, an alternative strategy was used to generate noisy projection data. Projections are simulated using a large number of photons in order to generate low noise projection data. A Poisson distributed pseudo random number generator is then used to simulate the desired level of Poisson noise.

We denote the noise in the projection image from the MC simulation as MC noise. The MC noise in a given projection bin is proportional to $\sqrt{N}$, where N is the number of simulated photons. It thus requires a large increase in the number of simulated photons to generate low noise projection data and make a substantial decrease in the MC noise level. To make simulation of the phantom population computationally feasible, it is desirable to track as few photon histories as necessary. However, if too few photons are used to simulate the low-noise projections, then after simulating Poisson noise the projections will have a higher variance than appropriate for the given count level. We thus investigated the effect of noise in the MC simulated images. We adapted and used a criterion based on the Relative Poisson effective count level [66] to determine the required number of simulated photons for each simulated organ. This technique provided a quantitative estimate of the true noise in the simulated projection data, including residual MC simulation noise.

Another technique that we used to make the phantom library general and the simulation computationally feasible was to simulate the organs separately. We divided each phantom into seven organs, each simulated separately. This enabled modeling of organ uptake variability by scaling and summing the projection data from the individual organs. Also, we separately simulated perfusion defects at different locations of the myocardial wall. To generate a projection image with a defect, the defect projection image was subtracted from the defect free projection prior to simulating noise [47].

3.2 Methods

3.2.1 Population of realistic digital phantoms

We developed a digital phantom population that realistically and accurately models the patient population. The population included 3 variations each in body size, heart size, and subcutaneous adipose tissue level, for a total of 27 phantoms of each gender. The simulated population is based on the 3D XCAT phantom with organ parameters sampled from the Emory PET Torso Model Database, which contains the anatomical measurements of 166 patients who underwent cardiac imaging. Table 3-1 shows the relevant anatomical parameters of the patient population for male and female populations.

Table 3-1. Anatomical parameters of the patient population (cm).

		Body LAT [a]	Body AP [b]	LV [c] Length	LV Radius	Height
Male	Mean	34.84	25.70	8.31	2.67	175.68
	Std.	2.15	2.44	0.93	0.47	6.80
	Minimum	29.40	20.00	6.60	1.90	154.94
	Maximum	38.40	31.40	11.60	4.00	187.96
Female	Mean	34.37	23.50	7.39	2.32	163.45
	Std.	3.25	2.08	0.92	0.33	7.34
	Minimum	26.70	19.60	5.70	1.60	149.86
	Maximum	40.90	28.80	10.50	3.50	177.80

[a] LAT: Lateral dimension
[b] AP: Antero-posterior dimension
[c] LV: Left ventricle

In this work, we used a set of user-controllable parameters [35] to vary the anatomy of the XCAT phantom. By changing these parameters, different levels of inner core body sizes, left ventricle length and radius and subcutaneous adipose tissue thicknesses were simulated.

To model variation in body size, the torso and the organ sizes of the 3D XCAT phantoms were scaled to match patients with average sizes and with sizes 2 standard deviations above and below the average, based on the data from the Emory Cardiac Database. Variability in the subcutaneous adipose tissue level was modeled by scaling the XCAT skin layer by the factors 0.5 and 1.5 of the average skin layer thickness for the given body size. We kept the ratio of the average body lateral to antero-posterior dimensions fixed to 1.36 and 1.47 for male and female populations, respectively, as observed in the male and female patient populations. Variability in heart size was modeled by changing the left ventricle (LV) length and radius while keeping their ratio fixed to 3.2 and 3.17 for the male and female population, respectively matching the observed measurements in the patient databases.

We modeled small, medium and large hearts for each of the body sizes. To do so, we varied the heart size in terms of the LV length and radius as a function of the different body sizes. For example, a medium-sized heart in a medium sized phantom is larger than a medium-sized heart in a small sized phantom and smaller than that in a large sized phantom. The heart parameters were scaled to match patients with average heart sizes and with sizes that are one standard deviation above and below the average.

Each phantom was digitized prior to simulation into 0.22-cm voxels in a 256x256x228 matrix. The range of the axial dimension varied such that we included 20 cm above and 30 cm below the centroid of the heart. We also checked each phantom visually to ensure that there was no unrealistic protrusion of organs into each other.

In addition to the anatomical variations, we varied the organ uptakes by dividing each phantom into seven “organs”, i.e., heart, liver, lungs, kidneys, gall bladder, blood pool, and the rest of the body (background). Figure 3-2 shows sample transaxial slices of the different organs in the phantom. We simulated projections of each organ separately assuming a homogeneous distribution inside. As described below, this enabled generation of the projection data corresponding to different organ uptakes by scaling and summing the projection data from the individual organs. It also enabled independently varying the number of photons used to simulate each organ in order to increase the simulation efficiency.

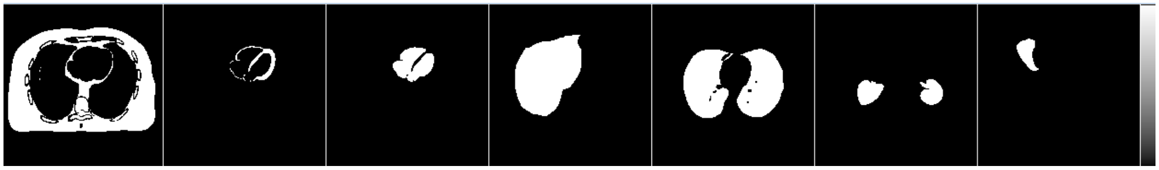

Figure 3-2**.** Sample transaxial slice of the background, heart, blood pool, liver, lung, kidneys and the gall bladder (from left to right) of phantom.

3.2.2 Simulate projection data using SimSET+ARF

We used the SimSET MC code in conjunction with the ARF method to generate projection images of the phantom population. This combination provides fast and accurate simulation of the SPECT system and includes modeling of septal penetration, Pb x-rays and scatter. SimSET does not provide a model of camera dead-time. Since dead-time effects are generally small for myocardial perfusion imaging, it was thus not modeled in this work.

The SimSET MC software requires two different distributions: the activity distribution and the material distribution. The activity distribution specifies the concentration of radioactive isotope in each voxel. We simulated photons with energy of 140.5 keV for Tc-99m; for Tl-201, we simulated photons with energies of 167.4, 135.3, 82.6, 80.3, 79.9, 70.8 and 68.9 keV, where the number of photons simulated for each energy was proportional to their abundances. In SimSET, the material (e.g., tissue type) in each voxel is specified via a pointer to a list of supported materials. The supported materials include materials used in scanners or phantoms (e.g., lead, scintillation crystals, and water) and tissue types (e.g., brain, blood, bone). To better model the interactions inside the body, we added new tissue types to the SimSET material tables including ribs, cartilage, kidneys, pancreas, bone marrow, spleen, thyroid and spine. The densities and the tissue compositions were taken from the International Commission on Radiation Units and Measurements (ICRU) report 46.

We modeled a GE Infinia dual-head SPECT system with two large field-of-view (LFOV) scintillation cameras each fitted with a GE low-energy high-resolution (LEHR) collimator. We modeled a 9.5 mm thick NaI(Tl) crystal within the scintillation camera with perfect energy resolution. We generated ARF tables for 1 keV wide energy windows from 48 keV to 140.5 keV for Tc-99m and from 48 keV to 167.4 keV for Tl-201. As a result, by appropriately weighting and summing these 1 keV wide projections we can model any desired energy resolution and energy window only by reprocessing the simulated projections. We created four separate sets of projection data corresponding to the detected photons that did and did not interact in the body and the collimator-camera system. This enables evaluation of the effects of the different components of the projection image on the final image quality.

In each case, the ARF tables were pre-computed using the methods described in [23]. Since the photons may undergo scattering in the phantom, the energies of the photons incident on the collimator can have any values below the emission energy. We broke down the expected incident photon energies into sub-ranges and computed separate ARF tables for primary photons and for scattered photons with energies in each sub-range. These latter ARFs were used to model collimator interactions for photons scattered in the body and incident on the collimator with a lower energy. The primary photons were processed using an ARF computed using point sources with the photopeak energies mentioned above for Tc-99m and Tl-201. The scattered photons were processed by using ARFs computed using sources emitting with a uniform distribution of energies in 10 keV wide energy sub-ranges spanning the range from 40 to 140 keV for Tc-99m and from 40 to 167 keV for Tl-201. These ARF tables were then used in the ARF-based simulations to generate projection data. The projection data were generated with a 0.44cm bin size at 120 views over 180° using a non-circular body-contouring orbit.

3.2.3 Relative Poisson effective count level

As mentioned earlier, for MC-based simulated projections, the noise in a projection bin is proportional to the square root of the number of simulated photons (Note: it is not equal to the square root of the intensity in a bin because of the use of variance reduction techniques). Figure 3-3 illustrates the concept of the MC residual noise in the low noise projections using an increasing number of simulated photons. It is clear that a large increase in the number of photons is required to make a significant impact on the MC noise level.

Our ultimate goal is to generate projection data with Poisson noise. One approach is to simulate projections using a very large number of photons in order to obtain an essentially noise-free estimate of the projection and then simulate Poisson noise using a Poisson pseudo-random number generator. It is desirable to be able to quantify the effects of the residual noise on the final projection data. To do this we introduce the concept of the relative Poisson effective count level.

The relative Poisson effective count level (r_{eff}) is defined as the ratio between the Poisson variance, σ_P^2 for a given count level and the total variance, σ_T^2, including the variance contributions from the simulated projection (residual noise from the MC procedure) and the Poisson random number generator (RNG). Ideally the projection data from the simulation would have an r_{eff} of 1. However, this would require simulating a very large number of photons. An expression for r_{eff} was derived in [66] and is given by:

$$r_{\mathrm{eff}} = \frac{\sigma_P^2}{\sigma_T^2} = \frac{s\bar{p}_s}{s^2\sigma_{\bar{p}_s}^2 + s\bar{p}_s}, \tag{3.1}$$

where $\bar{p}_s$ is the mean projection image using M batches of simulated photons, $\sigma_{\bar{p}_s}^2$ is the variance of the mean projection image, $\bar{p}_s$, and s is the scaling factor needed to scale this simulated projection data so that it has a clinically realistic count level. We note that the variance due to the MC procedure in the simulated projections is equal to the variance before scaling, $\sigma^2_{\overline{p}_s}$ times s^2, and the variance due to the RNG is equal to the count level, $s\overline{p}_s$.

In MC simulations, it is desirable to run the simulation multiple times using different random seeds to generate independent sequences and thus independent simulated projection images. We calculated the mean projection image $\overline{p}_s$ and its variance $\sigma^2_{\overline{p}_s}$ using M ensembles of MC simulated projection images p_s^i. Each projection image p_s^i was simulated using a batch of 50 million photons.

$$\overline{p}_s = \frac{1}{M}\sum_i p_s^i, \tag{3.2}$$

$$\sigma^2_{\overline{p}_s} = \frac{1}{M^2}\operatorname{var}\left(\sum_i p_s^i\right) = \frac{1}{M}\sigma^2_{p_s^i}. \tag{3.3}$$

To determine the required number of batches of photons to achieve a given r_{eff}, the expression in (3.1) can be written in terms of M as:

$$M = \frac{s\, r_{eff}\sigma^2_{p_s^i}}{\overline{p}_s(1-r_{eff})}, \tag{3.4}$$

and thus the total number of photons required is equal to M times 50 million photons.

To make the simulation of the population computationally feasible and achieve acceptably low noise levels in the heart region of the projection image, we set the r_{eff} of the different organs to the values shown in Table 3-2.

Table 3-2. Relative Poisson effective count level values for the different organs for Tc-99m and Tl-201 simulation.

	Heart	Liver	Lung	Gall Bladder	Kidney	Blood pool	Background
Tc-99m	0.98	0.95	0.97	0.85	0.85	0.99	0.85
Tl-201	0.99	0.98	0.99	0.98	0.9	0.99	0.9

The choice of the particular $\boldsymbol{r}_{\mathbf{eff}}$ values was somewhat empirical. Quantitatively, the effect can be understood in terms of the value itself: the total variance is $1/r_{\mathrm{eff}}$ higher than the desired Poisson variance. The particular choice of r_{eff} was made based on a combination of qualitative, quantitative, and practical considerations. In fact, the advantage of r_{eff} is that it shows how much computational effort is needed to provide a given amount of additional quantitative advantage. Correlating the quantitative values to visual quality of the projections is somewhat subjective. To give a better idea of how r_{eff} relates to the visual image quality, projection images shown in Figure 3-3 correspond to the 13 r_{eff} values indicated in Table 3-3 plus $r_{\mathrm{eff}} = 0.99$.

Table 3-3 also gives the mean square difference (MSD) in units of counts between projections of the heart of a medium sized male phantom with various r_{eff} values compared to the projection with the $r_{\mathrm{eff}} = 0.99$.

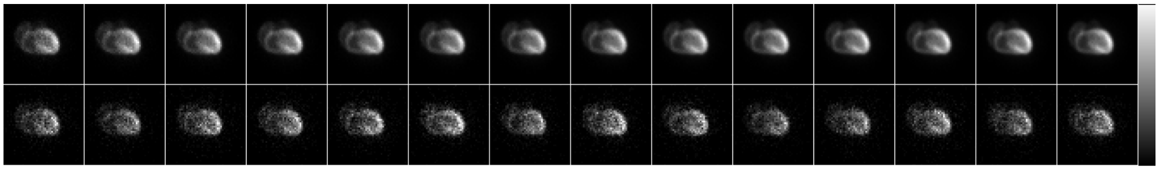

Figure 3-3. MC simulated anterior projections of the heart using 2, 4, 6, 8, 10, 12, 14, 16, 18, 20, 22, 24, 26 and 28x10^8 photons (top row from left to right) and the corresponding projections after adding Poisson noise (bottom row).

Table 3-3. Mean square difference between the heart projection images with various r_{eff} and the projection image with r_{eff} =0.99

$\mathbf{r}_{\mathbf{eff}}$	0.881	0.934	0.954	0.965	0.972	0.976	0.98	0.982	0.984	0.986	0.987	0.988	0.989
MSD	1.06	0.48	0.3	0.2	0.14	0.11	0.09	0.06	0.05	0.03	0.02	0.01	0.01

3.2.4 Modeling energy resolution

As mentioned earlier, projections were generated assuming a perfect detector (i.e., energy resolution equal to zero) to allow modeling of any arbitrary energy resolution. Also, they were generated into 1 keV wide energy bins so they could be combined to permit study of the effects of window width. Energy resolution was modeled at the time the windows were combined to form an acquisition energy window in order to allow studying the optimal energy windows as a function of energy resolution.

For any arbitrary acquisition energy window, $ewin$, and detector with energy resolution, $eres$, we model a projection image ($\boldsymbol{p}_{\mathbf{ewin}}^{\mathbf{eres}}$) as

$$p_{\mathbf{ewin}}^{\mathbf{eres}} = \sum_{e=48}^{184} w_e^{\mathbf{eres}} p_e, \tag{3.5}$$

where $\boldsymbol{w}_e^{\mathbf{eres}}$ denotes the probability that an incident photon with an energy *e* would be detected in an energy window *e* for a detector with energy resolution *eres*, and p_e is the simulated projection image acquired in an energy window (*e,e*+1) using a detector with perfect energy resolution.

Detectors with arbitrary energy response functions can be modeled using Equation(3.5). For scintillation crystals such as NaI(Tl) and LaBr, the energy response can be modeled as a Gaussian function with a specified percent energy resolution at 140.5 keV respectively and an inverse square root energy dependence. For this model there is an analytic expression for $\boldsymbol{w}_e^{\mathbf{eres}}$. However, for detector materials such as CZT detectors, where the energy response is non-Gaussian, we developed an analytical model of the CZT energy response from which we could compute $\boldsymbol{w}_e^{\mathbf{CZT}}$.

The model of CZT energy spectral includes three parts: the charge induction efficiency as a function of depth of interaction, the probability that a gamma photon deposit its energy as a function of depth, and a Gaussian distribution of the generated charge carriers [67].

When a gamma photon with energy E_0 deposits its energy in a CZT detector at depth *x* it will generate N electron-hole pairs, where $N = E_0 / e$ and *e* is the pair creation energy of the

CZT detector (~4.64 eV). When a bias potential is added to the detector the electrons and holes will move toward and induce charges on the anode and cathode, respectively. The efficiency of the charge induction (or the fraction of charge collected) is given by the Hecht relation:

$$\eta(x)=\frac{\lambda_e}{D}(1-e^{-(D-x)/\lambda_e})+\frac{\lambda_h}{D}(1-e^{-x/\lambda_h}) \tag{3.6}$$

where, *D* is the detector thickness, λ_e is the mean free path of electrons, and λ_h is the mean free path of holes. The two mean free paths are related to the bias potential and characteristics of the detector material.

The detected gamma photon energy is proportional to the number of charges collected, therefore:

$$E(x)=\frac{\eta(x)}{\eta(x=0)}E_0 \tag{3.7}$$

Assuming that all the gamma photons are absorbed at the first interaction site in the detector, the probability that a gamma photon with energy E_0 deposits its energy in the CZT detector at depth x is given by Beer's law:

$$P(x)=\mu(E_0)e^{-\mu(E_0)x}dx \tag{3.8}$$

Here $\mu\left(E_0\right)$ is the linear attenuation coefficient of the detector material at energy E_0.

Also, due to counting statistics the final detected energy is Gaussian distributed and centered at $E\left(x\right)$ and has a variance *E*. The FWHM (in units of energy) of this Gaussian distribution is given by:

$$FWHM_{E(x)}=2.3548\eta(x)\sqrt{F\varepsilon E_0} \tag{3.9}$$

where F is the *Fano* factor, accounting for the difference between the observed energy resolution and that resulting from Poisson counting statistics [68, 69].

Based on this, we have the detector spectrum at energy E for gamma photon deposited at depth x as:

$$S(E,x) = \mu(E_0)e^{-\mu(E_0)x}Gaussian(E(x),E)\,dx \tag{3.10}$$

Integrating the above over the entire detector thickness, D, we then have that the detected energy spectrum, $S(E)$, is given by:

$$S(E) = \int_0^x \mu(E_0)e^{-\mu(E_0)x}G(E(x),E)dx \tag{3.11}$$

or as a discrete approximation:

$$\begin{aligned} S(E) &= \sum_{i=0}^{L} \mu(E_0)e^{-\mu(E_0)x_i}G(E(x_i),E)\Delta x \\ x_i &= i * \Delta x \end{aligned} \tag{3.12}$$

Based on the above model, we calculated the energy spectrum for Tc-99m detected in a 5mm thick CZT detector system with ~500V bias potential. Figure 3-4 shows good agreement between the measured and calculated spectra based on the model. Note the peak at 40 keV is from a characteristic X-ray of the CZT that is not included in the model.

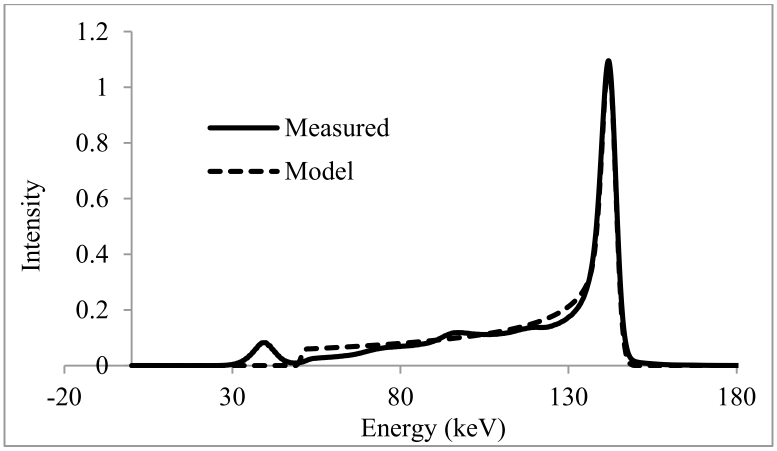

Figure 3-4. Comparison between measured and calculated spectrum of Tc-99m.

Figure 3-5 shows the detection probability of a photon in a 20% wide acquisition energy window centered at 140.5 keV for three different detectors as a function of the photon's energy. For the case of ideal detectors, all photons with energies within the energy window range are counted. For detectors with a Gaussian energy response, such as NaI(Tl) crystals, notice the symmetric distribution of the photons detected in the acquisition energy window. However, for CZT detectors, it is quite clear the asymmetric distribution of the detection probability results from the tail of the energy resolution function.

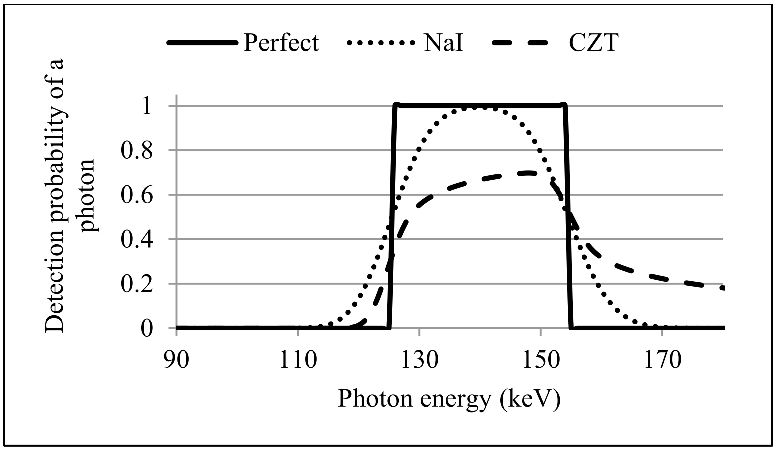

Figure 3-5. Detection probability of photons for a perfect, NaI(Tl) crystal and CZT detector in a 20% wide acquisition energy window centered at 140.5 keV.

3.2.5 Validation of the energy window and energy resolution modeling method

The proposed simulation approach used the SimSET MC code and ARF tables to model the interactions inside the body and collimator-detector system respectively. ARF tables were generated assuming a perfect detector system into 1 keV wide bins. Finally, the acquisition energy window and the detector energy resolution were modeled by appropriately weighting and summing the 1 keV wide projections using Equation(3.5). The former simulation tools have been extensively validated as mentioned earlier. However, the method of modeling the energy window and resolution has not been validated yet.

We validated the proposed method by comparing projections generated using Equation(3.5) with those simulated using pre-generated ARF tables that include models of the energy window and resolution. We computed the percent average absolute difference for the projection images of the different organs using both methods. We investigated acquisition energy window widths of 10%, 20% and 40% centered at 140.5 keV for Tc-99m modeling a NaI(Tl) scintillation crystal. For each organ, the number of simulated photons corresponded to r_{eff} values as given in Table 3-2.

3.2.6 Modeling uptake variability

For each phantom in the population, we simulated low noise Tc-99m and Tl-201 projection data for the heart, liver lung, gall bladder, kidney, blood and background (including all other organs). By doing so, we could generate a projection image of the entire phantom for any relative uptake value in these organs and product of injected activity and acquisition duration by scaling and summing these individual sets of projection data followed by simulating Poisson noise. Variations in organ uptake were modeled by randomly sampling the scale factors from truncated Gaussian distributions with parameters as shown in Table 3-4. The distributions were based on data from a set of 34 patients who underwent dual isotope myocardial perfusion studies. Patients were injected with 30 mCi of Tc-99m and 4 mCi of Tl-201 following a standard clinical protocol.

Table 3-4. Activity parameters of Tc-99m and Tl-201.

Activity (counts/cm^3)	Mean		Std. deviation		Minimum		Maximum	
	Tc-99m	Tl-201	Tc-99m	Tl-201	Tc-99m	Tl-201	Tc-99m	Tl-201
Heart	9139	3090	2625	605	4774	2030	15716	4118
Liver	3852	1994	2362	680	709	1099	10061	4071
Lung	843	396	330	105	408	255	1957	658
Gall Bladder	80299	668	63726	286	10234	379	279583	1540
Kidney	13208	6438	5391	1528	6086	3629	24750	9741
Blood	731	668	360	286	234	379	2011	1540
Background	731	668	360	286	234	379	2011	1540

3.3 Results

3.3.1 Population of realistic digital phantoms

Figure 3-6 to Figure 3-8 show sample coronal and transaxial images of attenuation distributions illustrating variations in body size, heart size and subcutaneous adipose tissue thickness of the population.

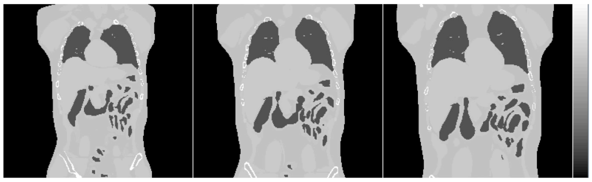

Figure 3-6. Sample coronal images of the attenuation distribution from the male phantom population showing variations in body size for a medium heart size and average subcutaneous adipose tissue thickness.

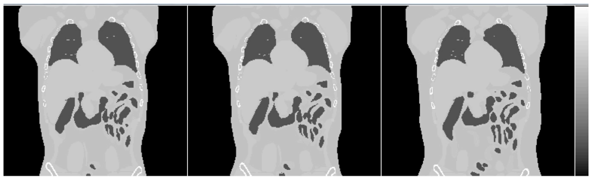

Figure 3-7. Sample coronal images of attenuation distribution from male phantom population showing variations in subcutaneous adipose tissue thickness for medium body and heart sizes.

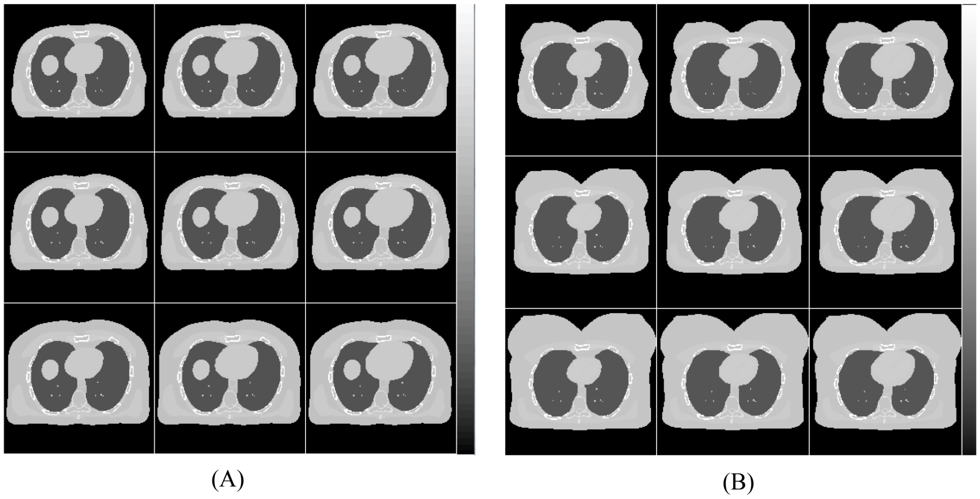

(A) (B)

Figure 3-8. Sample transaxial images of the attenuation distribution from male (A) and female (B) phantom populations showing variations in heart size (left to right) and subcutaneous adipose tissue thickness (top to bottom) for a medium body.

3.3.2 Simulated projection data using an efficient Monte Carlo method

For each phantom and organ we calculated the required number of simulated photons using Equation(3.4). Figure 3-9 shows sample low noise projection images using $r_{\mathbf{eff}}$ values from Table 3-2.

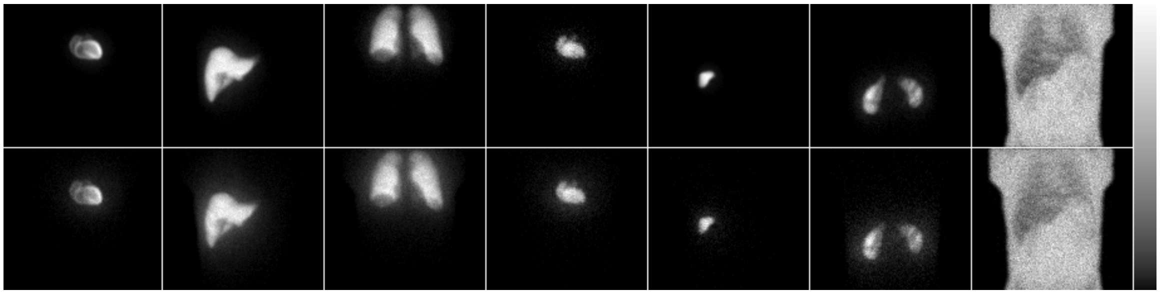

Figure 3-9. Low noise projection images of Tc-99m (top row) and Tl-201 (bottom row) of a medium sized phantom. Projection images were acquired in a 20% acquisition energy window centered at 140.5 keV for Tc-99m and 30% acquisition energy window centered at 72 keV for Tl-201.

We validated the method for simulating data for an arbitrary energy window and resolution by comparing projections generated using Equation(3.5) with those simulated using ARF tables where the energy window and resolution were modeled when generating the ARF tables, as has been used and validated in previous work. The same exact set of photons exiting the body was used to generate both projections. Figure 3-10 shows the projection image of the different organs generated using both methods. We computed the percent average absolute difference, defined as the absolute value of the pixel-by-pixel difference in projections, summed this over all projection bins, and divided this by the average of the sum of the two projections. Using the absolute value prevents cancellation of errors with different signs in the sum, and summing before dividing by the mean prevents voxels with very small values from dominating the error metric. The average absolute percent difference was always less than 0.1% and was generally substantially smaller than this.

Some difference in the two methods is expected due to differences in the way the effect of energy resolution and the collimator-detector response function (CDRF) are modeled in the two methods. In particular, when using data from 1 keV wide bins the energy resolution and the probabilities of counting photons in a given energy window were calculated based on the energy value at the center of each energy bin. On the other hand, when the energy resolution was included in the ARF, it was modeled for each photon energy when generating the ARF. In addition, the effects of the CDRF were averaged over the window by sampling photon energies from a uniform energy distribution spanning the range of the ARF energy window. Thus, the method of including energy resolution assumes that the CDRF is energy invariant over a larger range of energies than the method using 1 keV bins. This latter effect explains the increasing percentage difference with increasing the energy window width.

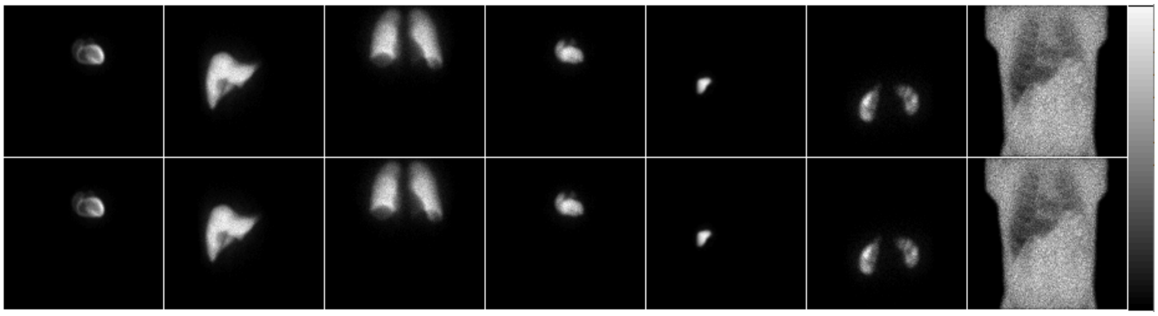

Figure 3-10. Low noise projection images of the different organs for a medium sized phantom for Tc-99m acquired in a 20% acquisition energy window centered at 140.5 keV. Energy window and resolution are modeled using Equation (3.5) (top row) and inside the ARF (bottom row).

Table 3-5. Percent average absolute difference of projection images for the different organs

Energy window width / Organ	Heart	Liver	Lung	Blood pool	Gall bladder	Kidney	Background
10%	0.003	0.003	0.003	0.003	0.003	0.003	0.004
20%	0.007	0.007	0.007	0.007	0.008	0.007	0.008
40%	0.084	0.079	0.085	0.081	0.087	0.079	0.092

As mentioned earlier, we generated separate sets of projection data for each of the four categories of detected photons (Figure 3-11), i.e., (A) photons that did not interact inside the body or the collimator, (B) photons that did not interact inside the body but interacted in the collimator, (C) photons that interacted inside the body but did not interact in the collimator, and finally (D) those that interacted inside the body and the collimator.

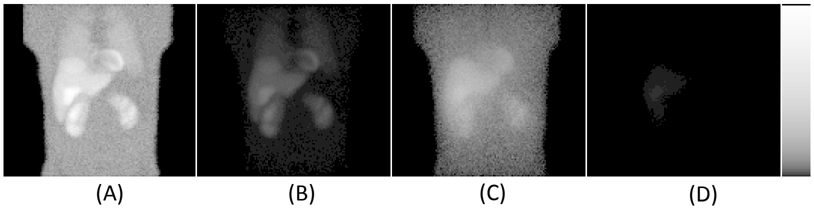

Figure 3-11. Low noise Tc-99m images for the different components of the projection. The components are: (A), (B), (C), and (D). Images were displayed using a logarithmic gray scale to better show the lower uptake organs.

Figure 3-12 shows sample noisy projection images modeling uptake and anatomical variations by scaling and summing the individual organ projections using scale factors randomly sampled from the corresponding truncated Gaussian distribution with parameters shown in Table 3-4.

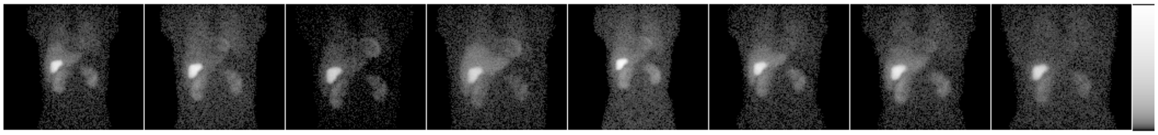

Figure 3-12. Sample Tc-99m noisy projection images modeling anatomical and uptake variations acquired in a 20% acquisition energy window width. Images were displayed using a logarithmic gray scale to better show the lower uptake organs.

3.3.3 Applications

In the context of MPS, one application would be finding the optimum Tc-99m or Tl-201 acquisition energy window width. To do that, we will have to generate projection images acquired in various acquisition windows. By applying the above-described methods of modeling the energy window and resolution, we can generate the projection images in any arbitrary energy window and resolution quickly and easily.

Figure 3-13 shows sample low-noise and noisy projection images simulated for various energy windows. Note the tradeoff between increasing scatter, which reduces the contrast of the myocardium, and noise as the energy window width increases. Figure 3-14 shows sample noisy Tc-99m projection images for a medium sized phantom acquired from anterior projection view for different energy windows using a perfect detector, NaI(Tl) crystal and CZT detector.

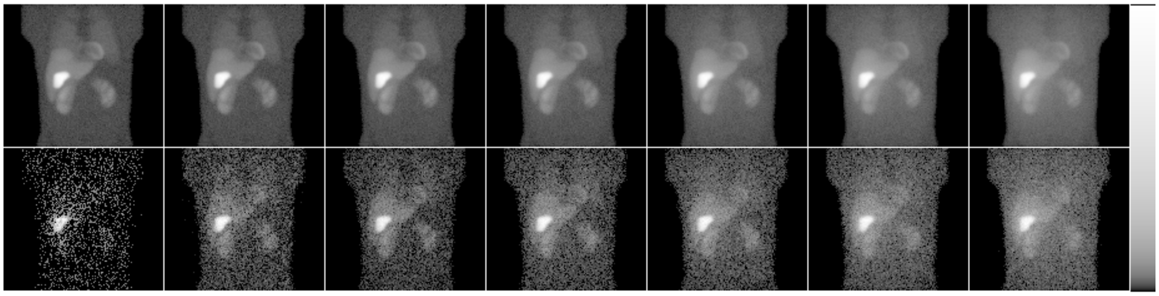

Figure 3-13. Sample of low noise (top) and noisy (bottom) MC simulated projection images of a medium sized male phantom with medium size heart and average subcutaneous adipose tissue thickness acquired from an anterior projection view in energy windows with widths of 1, 9, 25, 37, 57, 77 and 101 keV centered at 140.5 keV from left to right respectively. Images were displayed using a logarithmic gray scale to better show the lower uptake organs.

Another application of interest is the optimization and evaluation of the simultaneous stress Tc-99m/rest Tl-201 dual isotope cardiac SPECT protocol. Crosstalk contamination, where photons emitted by Tc-99m contribute to the Tl-201 image due to interactions in the patient and gamma camera, degrades image quality. Figure 3-15 demonstrates the effect of the down scatter component from Tc-99m into a Tl-201 energy window. Note the negligible contribution of Tl-201 to the Tc-99m energy window. Reducing the amount of crosstalk by optimizing energy windows settings and relative injected activities could reduce the impact of crosstalk and improve the image quality. The flexible design of the projection database allows us to generate rapidly projections for various combinations of Tc-99m and Tl-201 acquisition windows.

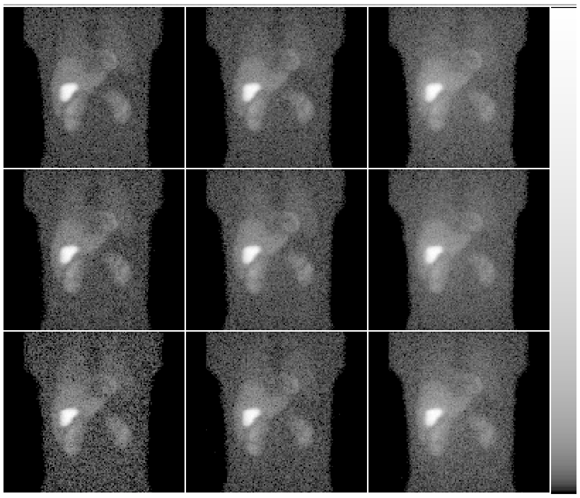

Figure 3-14. Sample noisy Tc-99m projection images for a medium sized phantom acquired from an anterior projection view in 10%, 20% and 40% wide energy windows (from left to right) using a perfect detector, NaI(Tl) crystal with 9% energy resolution and CZT detector (from top to bottom, respectively). Images were displayed using a logarithmic gray scale to better show the lower uptake organs.

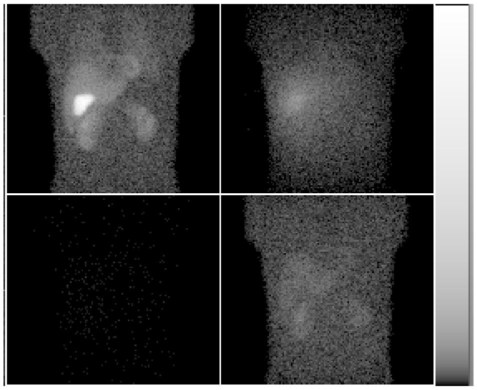

Figure 3-15. Sample noisy projection images for Tc-99m (Top row) and Tl-201 (bottom row) acquired in a 20% acquisition energy window (left) centered at 140.5 keV and 30% acquisition window (right) centered at 72 keV using a NaI(Tl) crystal with 9% energy resolution. Images were displayed using a logarithmic gray scale to better show the lower uptake organs.

3.3.4 Computational efficiency

The generation of projection data for each complete phantom realization required 14.8 CPU years and 48 GB of disk space. This represents a total of 799 CPU years and 2.6 TB of disk space for the entire phantom population. The CPU times are for a single core of a 2.33GHz Intel Xeon E5410 quad core processor. A breakdown of the simulation times of one batch of simulated photons is shown in Table 3-6. Note that for these simulations most of the processing time is taken in the ARF code, which models the interactions inside the collimator and detector system. This is because we generated projection images in 1 keV energy bins. We ran a simulation using SimSET+ARF where we modeled the acquisition energy window and resolution in the ARF tables prior to the simulation. We call this simulation the "Standard" method. We see that the simulation time is less by a factor of 4 than our simulation time. However, when investigating multiple combinations of windows and resolutions as in [3, 4], where a total of 13 energy windows and 3 energy resolutions were investigated, the "Standard" SimSET+ARF method would have taken 10 times longer than the proposed method.

Table 3-6. Comparison of CPU time for simulation of Tc-99m using SimSET+ARF.

	SimSET+ARF	SimSET+ARF "Standard"
Number of photons	50 million	50 million
SimSET	~55 minutes	~55 minutes
ARF	~285 minutes	~32 minutes
Overhead time [a]	~2 minutes	0

[a] Overhead time includes the time taken to sum the individual 1 keV projection images to generate a projection image for a given energy window and resolution combination.

3.4 Discussion

This work presents a methodology for the design and simulation of a digital phantom population for use in myocardial perfusion SPECT research. The population included variability in gender, body size, heart size and fat level with no modeling of the cardiac or respiratory motion included. The major application of the specific data set generated here was focused on the energy dimension, because of our interest in dual isotope imaging. For this application, choosing optimal energy windows is important. The energy dimension is also important for investigating the potential improvement in image quality provided by detectors with improved energy resolution. Since we were primarily interested in comparing scatter and crosstalk compensation methods and optimizing energy windows, respiratory and cardiac motions would impact all methods equally and tend to result in a general reduction in performance. On the other hand, uptake distribution and organ geometry result in different degrees of scatter and crosstalk artifacts. Previous results have indicated the importance of including anatomic and uptake variability [47], and there is certainly the potential for different energy windows or compensation methods to perform differently with different anatomies and uptakes. In an attempt to acknowledge the fact that the heart changes shape during beating motion, we did generate the phantoms at the point in the cardiac cycle where the heart was closest to the average of the heart over the 8 gates of the cardiac cycle.

Adding the time dimension (motion) to the simulations would require a substantial increase in computational complexity. With current MC simulations this would require simulating data at multiple points in the cardiac and respiratory cycle. Since these motions are not synchronous, this involves simulating all possible combinations. For example, using 8 phases each for cardiac and respiratory phases would increase the computational complexity by a factor of 64. If the images were ultimately to be added together, the simulation time would of course not be increased by this factor to obtain an equal noise level. However, the amount of disk space, number of simulations, etc., would all be increased. However, in principle the methodology described in this work could be extended to include motion without difficulty beyond the increased computational complexity.

One other aspect of the clinical situation that is not modeled is the effect of the various data corrections. These include energy, spatial, and linearity corrections as well as corrections for center of rotation. In modern gamma cameras these corrections are implemented during the acquisition process or prior to image reconstruction, and the raw projections given to the user often include them. In previous studies, our reconstruction codes, which do not implement these corrections, have provided accurate reconstructions with good image quality. We have observed this for radionuclides as diverse as Tc-99m [70], In-111 [64], I-131 [65], and Y-90 bremsstrahlung photons [71]. As a result, we believe that residual correction errors are small compared to other effects. A related effect that is not modeled in this work is the potential change in noise characteristics that these methods might introduce. However, once again this effect is likely small compared to the quantum noise level itself. Thus we believe these effects can safely be neglected for the simulation applications of interest here, as they have been in essentially all nuclear medicine simulations we are aware of to date.

The combination of the methods used allowed us to efficiently simulate realistic projections for a realistic population of phantoms. The population is useful for performing rigorous and comprehensive optimization and evaluation of the instrumentation, acquisition and reconstruction/compensation methods in the context of MPS imaging. We have already used the phantom population and the simulated projection images to find the optimal Tc-99m acquisition energy window and investigated the effects of energy resolution on the image quality using the Ideal Observer (IO) and the recently developed Ideal Observer with Model Mismatch (IO-MM) in the context of a myocardial perfusion SPECT defect detection task [3, 4]. Finally we have also investigated the optimal acquisition energy window and relative injected activity in the context of dual isotope MPS [5].

3.5 Conclusion

There is an increasing need to perform initial validation, optimization, and evaluation of nuclear medicine imaging methods using realistic simulations. Such simulations must realistically model the clinical situation, including patient populations and clinical imaging systems. Technologies for generating realistic phantoms and modeling imaging systems have previously been developed. However, modeling populations of phantoms and providing the ability to evaluate parameters such as energy window and energy resolution function, acquisition time, and administered activity requires combining multiple technologies. In addition, despite increases in available computer processing speed, careful implementation is needed for the simulations to be computationally feasible.

We have developed a comprehensive method for efficiently simulating such a population in the context of myocardial perfusion imaging. The set of digital phantoms, the simulation methods themselves, and the set of simulated MPS projections provide tools and methods needed to expand the applications of realistic simulation in the optimization and evaluation of nuclear medicine and SPECT imaging.

4. Collimator optimization in MPS using the ideal observer for lesion detection and joint detection and localization tasks

4.1 Introduction

Single photon emission computed tomography (SPECT) is a widespread and cost-effective modality for diagnosis of cardiovascular disease using myocardial perfusion SPECT (MPS). In SPECT, the collimator establishes a relationship between positions in the image projection plane and directions in space that largely determines the spatial resolution. This directional information is only imperfectly obtained, and at the cost of a loss of sensitivity and a resulting increase in quantum noise in the images. The tradeoff between resolution and noise has a significant impact in determining the diagnostic accuracy of readers interpreting the images.

Collimator properties including hole length, hole diameter and septal thickness determine the tradeoff between resolution and sensitivity. Techniques for selecting collimator parameters for a given geometric resolution are well established [72-74]. Typically, a desired spatial resolution and maximum permissible single-septal penetration probability at some specified energy are specified *a priori,* and the collimator parameters giving the highest sensitivity are then determined. There are, however, important limitations to this approach regarding how to optimize the resolution–sensitivity trade-off for a given task, such as estimation, i.e., quantifying one or more parameters of interest using the given image data [75-78], or classification, i.e., deciding to which class an image belongs [38, 40, 77, 79-85]. In this work, we focus on two particular classification tasks: binary signal detection and the arguably more clinically realistic joint detection and localization task. In a binary detection task, an observer is asked to classify a given image as either containing or not containing a defect. In the joint detection and localization task, the observer is required to jointly detect the presence of a signal and estimate its location.

Performing task-based system optimization requires specification of a task, an observer, and a scalar figure of merit (FOM) that quantifies the performance of the observer on the task. One obvious way to perform task-based assessment of medical image quality is with a human observer study. However, human observer studies are time consuming and expensive. Thus, in addition to (and frequently instead of) using human observers, model observers are often used to evaluate image quality [24, 86]. Model observers are mathematical operators, either linear or non-linear, that act on an image to extract some information and return a test statistic or decision variable that is then compared with a decision threshold to decide whether the signal is present or absent. A receiver operating characteristic (ROC) curve is then constructed by calculating the true positive fraction (TPF) and false positive fraction (FPF) pair for each decision threshold. The performance of a specific observer can be characterized by the ROC curve and the area under that curve (AUC_d) [87]. For the joint detection and localization task, a curve similar to the ROC curve, called the localization ROC curve (LROC), is constructed by calculating the percent correct localization (PCL) and FPF pair for each threshold value. The task performance measure for this joint task is the area under the LROC curve (AUC_{d+l}) [37, 53].

Two important categories of model observers are ideal and anthropomorphic observers. Anthropomorphic observers, such as the Channelized Hotelling Observer (CHO) [43] and the recently developed visual search (VS) model observer [88], are designed to mimic human observer performance or performance rankings for various tasks, including detection [44, 45, 48, 49, 51, 89] and localization [50, 52, 88, 90]. Anthropomorphic observers, especially the CHO, have shown good agreement with human observers, but applying them to reconstructed images is challenging because of the difficulty of estimating the noise properties of reconstructive images analytically, and the computational expense of estimating them using ensemble techniques. In this regard, the VS model observer for localization tasks is appealing, as it has been shown to predict human observer performance rankings without the need to estimate the noise covariance of the reconstructed images [88, 90]. However, both the CHO and VS are applied to reconstructed images, which mean there is a need to optimize image reconstruction, even when only comparing, for example, different collimators. For example, the regularization parameters optimal for one collimator are not, in principle, optimal for another collimator.

The Ideal Observer (IO) has full knowledge of the imaging system and object statistics and makes optimal use of all the information in the image. Thus, it outperforms all other observers and sets an upper bound on task performance as measured by Bayesian risk, and thus on FOMs such as the AUC_d and $\mathrm{AUC}_{\mathrm{d+l}}$ [24, 37] . IO performance can be estimated directly from the projection data, where noise statistics are well known and easy to characterize. Subsequent conventional (linear) image processing or reconstruction steps do not improve its performance. In optimizing instrumentation and acquisition parameters (i.e., factors affecting task performance that precede reconstruction), it is helpful to use the IO because it identifies the parameter settings that maximize information about the task contained in the measured raw data. The role of the subsequent reconstruction, regularization, and compensation steps can then be conceptualized as matching the information in the raw data for optimal performance by a human observer.

Despite the potential advantages of using the IO to evaluate and optimize imaging systems, it is very difficult to estimate IO performance for realistic tasks that model realistic objects and background variability arising from variations in patient anatomy and biokinetics. This is because the background model statistics are complex and difficult to analyze analytically. Many applications of the IO to imaging system optimization and evaluation have used simplified assumptions to make the IO computationally or mathematically tractable, such as considering the task of detecting a signal-known-exactly superimposed on a background-known-exactly (SKE/BKE). However, this task is a poor model of the clinical task, and using the IO to optimize nuclear medicine imaging for this task has given rise to some results that are contrary to experience, e.g., that the best acquisition energy window was no energy window and the best collimator was no collimator [81, 91, 92]. It is thus important for clinically relevant optimization that object models be as realistic as possible and include background variability [31, 47, 66, 81, 89].

Several studies have applied the IO to simulated background-known-statistically (BKS) and signal-known-exactly (SKE) or signal-known-statistically (SKS) data for both a binary detection task [33, 34, 40, 41, 93, 94] and a joint detection and localization task [38, 95]. However, to allow computation of the requisite likelihood functions analytically, even when background variability was modeled, these studies have been limited to cases where object and system models were relatively simple, such as modeling 2D SPECT systems [38], modeling collimator response as spatially invariant Gaussian blurring [33], and modeling the background as statistically defined lumps [31]. Background variability modeled as statistically defined lumps has been primarily adapted for mathematical convenience and has been shown to be adequate for background modeling in mammography. However, for cardiac SPECT imaging, lumpy backgrounds might not be the most suitable background model to use. It is thus highly desirable, for a clinically relevant optimization, to include more realistic background models.

Kupinski et al. [33] developed a method to estimate the performance of the IO for realistic and general background-known-statistically and signal-known-exactly (BKS/SKE) paradigms. Park et al. [34] extended the method to estimate the performance of the IO in the case where both backgrounds and signals are random with known statistical properties (BKS/SKS). These methods use Markov Chain Monte Carlo (MCMC) techniques to estimate the likelihood ratios for, in principle, arbitrarily complex objects and imaging systems. However, these methods require generating very large numbers of noise-free projections of the background for arbitrary values of background parameters. Thus, computation time considerations practically limit these methods to simplified system models and backgrounds.

He et al. [41] adapted Kupinski's method to backgrounds parameterized by a combination of discrete and continuous values. Discrete values were used to specify phantom anatomies and continuous values to specify organs uptake. In this method, projections of all organs for all the discrete anatomies are precomputed and stored in a projection library from which projections for any particular value of the background parameters can be obtained very rapidly by scaling and summing appropriate members of the library. This method was applied in myocardial perfusion SPECT imaging using a realistic background model consisting of a parameterized torso phantom and projections generated using a realistic analytical SPECT projector. In this work, we extended that technique by using a more complete and realistic phantom library. We then used the MCMC technique to estimate the IO test statistic, i.e., the likelihood ratio, for both binary detection and joint detection and localization tasks in the context of MPS operating on realistic simulated backgrounds including anatomical and uptake variability.

4.2 Methods

4.2.1 Background variability

To provide clinically relevant optimization of imaging system parameters, it is important that the objects be as realistic as possible and include anatomical and uptake variability that models a clinical population. We have previously designed, developed, and reported on a digital phantom population based on the 3D XCAT phantom [1]. The simulated population included 3 variations each in body size, heart size, and level of subcutaneous adipose tissue (fat level), resulting in a total of 27 phantoms for each gender. The anatomical parameters of the population were based on the Emory PET Torso Model Database [96]. Figure 4-1 shows sample transaxial of the attenuation distribution illustrating variations in body size, heart size and subcutaneous adipose tissue thickness of the population.

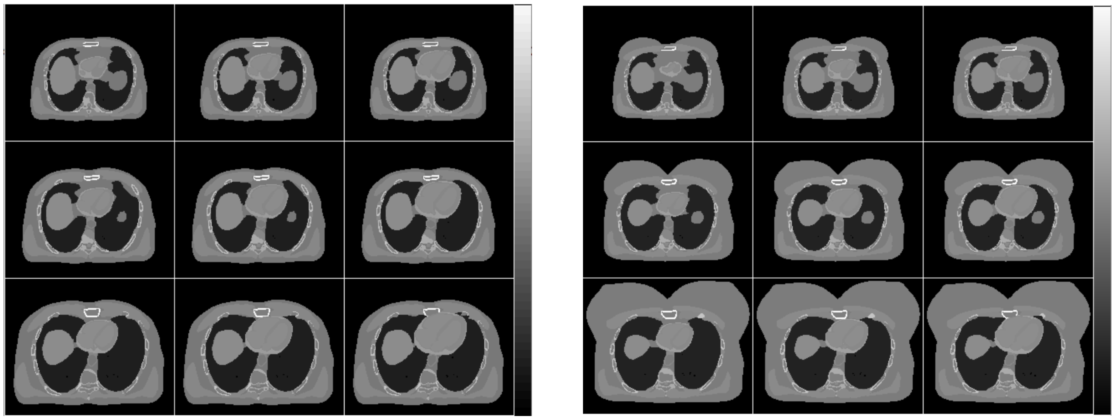

(A) (B)

Figure 4-1. Sample transaxial images of the attenuation distribution from male (A) and female (B) phantom populations showing variations in heart size (left to right) and body sizes (top to bottom) for a medium subcutaneous adipose tissue thickness.

In addition to the anatomical variation, we modeled uptake variation by separately generating projection data for the heart, liver and body (including other organs). We could then scale and sum the individual projections to model any arbitrary uptake ratio and level. Variations in organ uptake were modeled, as shown in Figure 4-2, by randomly sampling the scale factors, A_{heart}, A_{liver} and A_{body}, from truncated Gaussian distributions with parameters shown in Table 4-1. The parameters were derived from a set of 34 clinical studies of patients who underwent MPS. Values in Table 4-1 correspond to the number of detected counts within a 1-cm^3 volume within each of the different organs. To generate a projection image with a defect, the defect projection image was subtracted from the defect-free projection prior to simulating noise. We simulated a stress study of a standard MPS one-day stress/rest clinical protocol [97]. We modeled an injected activity of 10 mCi of Tc-99m and a total acquisition time of 26 minutes.

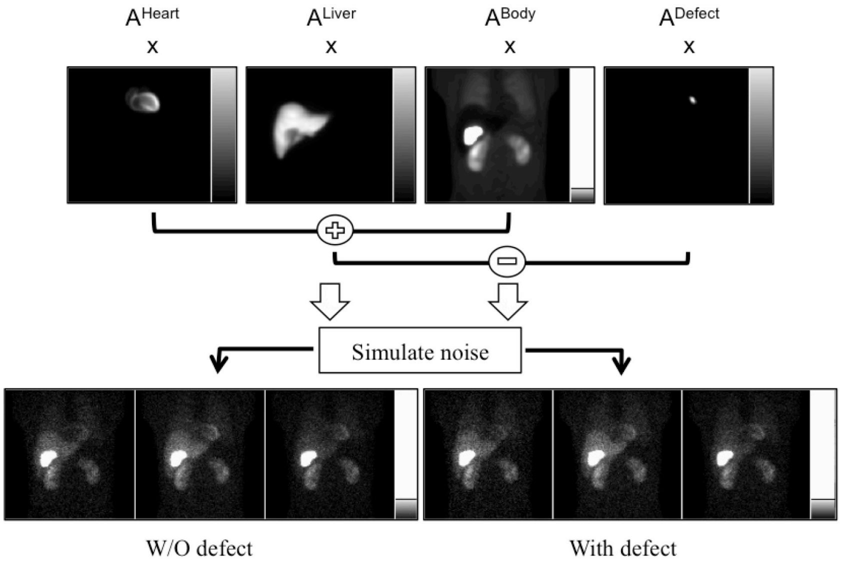

Figure 4-2. A schematic showing the modeling of variations in activity uptake

Table 4-1. Tc-99*m* activity distribution parameters

Activity (counts/cm^3)	Heart	Liver	Body
Mean	3046	1284	244
Std. dev.	875	787	120
Minimum	1591	236	78
Maximum	5239	3354	670

4.2.2 Simulated perfusion defects

We simulated perfusion defects at six different locations, each with extent and severity of 10% and 25%, respectively. The extent and severity are, respectively, the perfusion defect fractional volume and reduction of uptake relative to the normal myocardium. This combination of extent and severity was chosen to be challenging but clinically relevant. For each phantom, we varied the axial and angular extents of the defects to achieve the aforementioned volume extent. Figure 4-3 shows each of the six defect locations (labeled as d_1 to d_6 from left to right) in the short axis slices containing the defect centroid. Projection images of the heart and the different defects are shown in Figure 4-4. The perfusion defects, d_1 to d_5, were uniformly distributed over a mid-ventricular slice of the heart between the anterior and inferior walls through the lateral wall. The center of each successive defect was separated by 45 degrees. We simulated an additional perfusion defect, $d_{6,}$ centered at a mid-ventricular slice in the septal wall.

To study the effect of the defect size on the observer performance, we also simulated perfusion defects at locations d_2 and d_5 with 5% and 25% extents (labeled as $d_{2,5\%}$, $d_{2,25\%}$, $d_{5,5\%}$ and $d_{5,25\%}$ respectively) in addition to the 10% extent defects, as shown in Figure 4-5. For each defect, the product of the extent and severity was kept constant to model a constant overall reduction of the activity in the myocardium. Parameters of the simulated defects are reported in Table 4-2. Since the extent was fixed and the heart sizes were different for the various phantoms, the axial length of the defect was different for the different heart and body sizes. Thus, Table 4-2 gives the mean and standard deviation of the axial length.

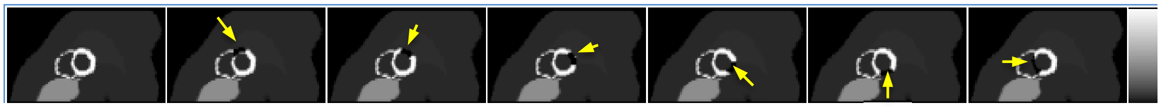

Figure 4-3. Sample short axis images showing a normal heart and a defective heart at six different locations of the myocardial wall. For illustrative purposes, defects shown have 100% severity.

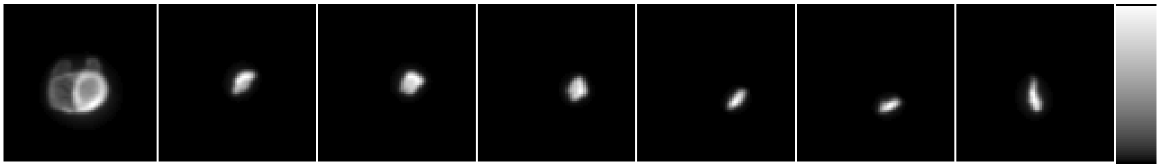

Figure 4-4. Sample projection images, from a left anterior oblique view, for the heart and the defects at locations d_1 to d_6 (from left to right).

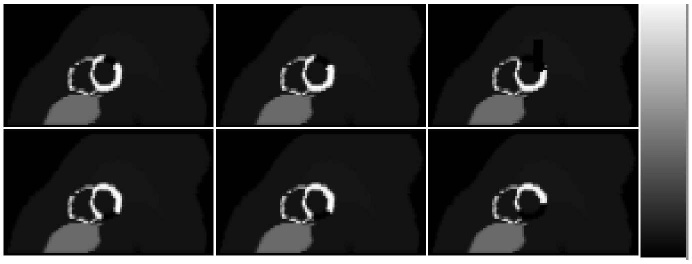

Figure 4-5. Sample short axis images showing a heart with a perfusion defect at two different locations (d_2 [top row] and d_5 [bottom row]) in the heart and extents of 5%, 10% and 25%, from left to right. For illustrative purposes, defects shown have 100% severity.

Table 4-2. Parameters of simulated defects.

Defect	Location	Extent (%)	Severity (%)	Length of defect (cm)	
				Mean	Std. dev.
d_1	Anterior	10	25	3.6	0.5
d_2	Antero-lateral	10	25	3.2	0.6
$d_{2,5\%}$	Antero-lateral	5	50	2.5	0.4
$d_{2,25\%}$	Antero-lateral	25	10	5.3	0.8
d_3	Lateral	10	25	3.4	0.6
d_4	Infero-lateral	10	25	2.8	0.5
d_5	Inferior	10	25	2.2	0.4
$d_{5,5\%}$	Inferior	5	50	1.7	0.3
$d_{5,25\%}$	Inferior	25	10	3.6	0.6
d_6	Septal	10	25	5.4	0.7

4.2.3 Projection data simulation

We generated projection data using an analytical projector that modeled attenuation, scatter, the collimator-detector response (CDR), a 9.5 mm thick NaI(Tl) crystal with an energy resolution of 9% at 140 keV (which we varied as one over the square root of energy), and a 4 mm intrinsic spatial resolution. Projection images were simulated at 60 equally spaced angles over a 180° acquisition arc extending from 45° right anterior oblique (RAO) to 45° left posterior oblique (LPO). We simulated a non-circular body-contouring orbit specific for each phantom. Projection images were formed in a 128x114 matrix with a pixel size of 0.442 cm. To model scatter in the object, we used the effective source scatter estimation (ESSE) method [19]. The ESSE method estimates the object-dependent spatially varying contribution of scattered photons to the projection data, based on the attenuation map and the activity distribution. The CDR was modeled using distance-dependent CDR functions (CDRFs). The CDRFs modeled hexagonal parallel-hole collimators and included the intrinsic, geometric, septal penetration and septal scatter response components. Scatter kernels used by the ESSE method and CDRF tables were pre-calculated using Monte Carlo simulations.

4.2.4 Collimator Design

We investigated a family of eight parallel-hole collimators that spanned a wide range of resolution-sensitivity trade-offs. The collimator parameters, i.e., hole length, hole diameter (flat-to-flat distance) and septal thickness, were chosen to maximize the sensitivity for each selected resolution with the value of the septal penetration criterion (i.e., the probability that a photon would pass through the thinnest possible full septum based on the hole geometry) at 140 keV fixed at 0.3%, to match that of the GE-LEHR collimator. We used standard formulas to calculate the collimator parameters for each given resolution [74, 77]. The parameters of the simulated collimators are listed in Table 4-3. Sample images of the heart of a medium sized phantom acquired using the different collimators are shown in Figure 4-6.

Table 4-3. Parameters of the simulated family of collimators

	Hole diameter (mm)	Septal thickness (mm)	Resolution [a] (mm) at 10 cm	Relative geometric sensitivity [b]
C_1	0.566	0.081	5.2	0.208
C_2[c]	1.242	0.178	6.9	1
C_3	1.730	0.248	9.2	1.940
C_4	2.136	0.307	11.0	2.956
C_5	2.533	0.364	12.4	4.157
C_6	2.925	0.420	13.8	5.544
C_7	3.700	0.531	16.7	8.872
C_8	4.468	0.642	19.7	12.933

[a] FWHM of the combined intrinsic resolution and geometric collimator resolution

[b] Sensitivity relative to that of the GE-LEHR collimator.

[c] Parameters were chosen to match GE-LEHR collimator.

The hole-length was 32 mm for all collimators, which is the hole-length that maximizes the sensitivity for the given penetration fraction.

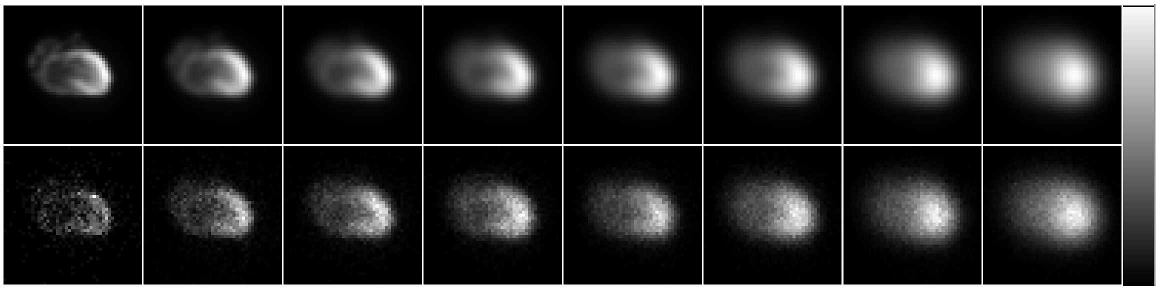

Figure 4-6. Sample noise-free (top row) and noisy (bottom row) projection images of the heart acquired at an anterior view using collimators C_1 to C_8, respectively, from left to right. From left-to-right note the decreasing noise (in the bottom row) and sharpness of the images, as expected.

4.2.5 Ideal Observer for detection and joint detection and localization tasks

In SPECT imaging, the projection data, **g,** can be represented by the following imaging equation:

$$\mathbf{g} = \mathbf{H}\mathbf{f} + \mathbf{n}, \tag{4.1}$$

where $\mathbf{H} \in \mathbb{R}^{MxN}$**,** the system matrix, is a continuous-to-discrete projection operator that maps the object $\mathbf{f} = [f_1, f_2, f_3 ... f_N] \in \mathbb{R}^N$ to the projection space and $\mathbf{n} \in \mathbb{R}^M$ is the (Poisson distributed) measurement noise. The object $\mathbf{f}$ consists of a random background, $\mathbf{f}_b$, and a signal, $\mathbf{f}_{s_j}$, if a signal is present at location j (j =1 to L). The background and signal projection images can then be expressed as $\mathbf{b} = \mathbf{Hf}_b$ and $\mathbf{s}_j = \mathbf{Hf}_{s_j}$ respectively.

In a binary detection task, the goal is to determine whether or not a defect is present based on the measured data. The two hypotheses to be tested can be represented mathematically as:

$$\begin{aligned} H_0 &: \mathbf{g} = \mathbf{b} + \mathbf{n}, \\ H_1 &: \mathbf{g} = \mathbf{b} + \mathbf{s} + \mathbf{n}, \end{aligned}$$

where $\mathbf{g}$, $\mathbf{b}$, $\mathbf{s}$ and $\mathbf{n} \in \mathbb{R}^M$ are the noisy projection, background, defect and noise data vectors, respectively and the hypotheses H_0 and H_1 mean signal -absent and -present, respectively.

The ideal observer uses the likelihood ratio $\Lambda(\mathbf{g}\,|\,\mathbf{b},\mathbf{s})$ of defect-present (H_1) to –absent (H_0) as the test statistic, $t_d(\mathbf{g})$.

$$t_d(\mathbf{g}) = \Lambda(\mathbf{g}\,|\,\mathbf{b},\mathbf{s}) = \frac{pr(\mathbf{g}\,|\,H_1)}{pr(\mathbf{g}\,|\,H_0)}. \tag{4.2}$$

However, for the joint detection and localization task, the observer is required to jointly detect and localize a defect among a set of L (L = 6) possible defect locations. In myocardial perfusion SPECT this would be, for example, detecting and specifying a segment of the heart that has a perfusion defect. The task can be extended to an L+1 decision task where L is the (finite) number of defects locations. When L equals 1, the problem becomes the binary detection task described above. The L + 1 hypotheses to be tested can be represented mathematically as:

$$\begin{aligned} H_0 &: \mathbf{g} = \mathbf{b} + \mathbf{n} \\ H_j &: \mathbf{g} = \mathbf{b} + \mathbf{s}_j + \mathbf{n}, \end{aligned}$$

We define the hypothesis H_j that the defect $\mathbf{s}_j$ is located at location j and j = 1, 2 … L.

The optimal decision strategy for the joint detection and localization task, as derived in [37], can be written as:

$$t_l(\mathbf{g}) = \max_{j\in\{1,2,...L\}} pr(j)\Lambda(\mathbf{g}\,|\,\mathbf{b},\mathbf{s}_j), \tag{4.3}$$

$$l(\mathbf{g}) = \arg\max_{j\in\{1,2,...L\}} pr(j)\Lambda(\mathbf{g}\,|\,\mathbf{b},\mathbf{s}_j), \tag{4.4}$$

$$\text{Decide } l(\mathbf{g}) \text{if}\, t_l(\mathbf{g}) > \tau, \text{ else decide } H_0,$$

where $t_l(\mathbf{g})$ is the test statistic for the joint detection and localization task. In (4.3) and (4.4), $pr(j)$ is the prior probability that a perfusion defect is present at location j. In this study, we assumed that the probability that a defect is present at any of the six locations is equal. In the above, $l(\mathbf{g})$ is the location assigned to the defect if the test statistic $t_l(\mathbf{g})$ is larger than a threshold value α.

For both tasks, it is required to calculate one or more likelihood ratios. For the case where the background and signal are known exactly (BKE/SKE) and the only source of randomness is the measurement noise, the expression for the likelihood ratio is:

$$\Lambda_{\mathrm{BKE}}\left(\mathbf{g}\,|\,\mathbf{b},\mathbf{s}_j\right) = \prod_i \left(1+\frac{s_j(i)}{b(i)}\right)^{g(i)} \exp\left(-s_j(i)\right), \tag{4.5}$$

where $\boldsymbol{i}$ is a pixel index in the background, signal and raw projection images.

However, for the BKS/SKE task, the expression for the likelihood ratio is given by:

$$\Lambda_{\mathrm{BKS}}(\mathbf{g}) = \int \Lambda_{\mathrm{BKE}}(\mathbf{g}\,|\,\mathbf{b},\mathbf{s}_j)\, pr(\mathbf{b}\,|\,\mathbf{g},H_0)\; db \tag{4.6}$$

Kupinski [33] has shown that if the background, $\mathbf{f}_{\boldsymbol{b}}$, and thus the projection images arising from them, $\mathbf{b}$, can be completely characterized by a statistically-defined set of parameters $\vec{\theta}$, and that for any given $\vec{\theta}$, there exists a unique $\mathbf{b}$, the expression of the likelihood ratio can reformulated as an integral of the BKE likelihood ratio over the background, $\mathbf{b}=\mathbf{b}(\vec{\theta})$, parameterized by the vector $\vec{\theta}$, given the image $\mathbf{g}$ under H_0 as:

$$\Lambda_{\mathrm{BKS}}(\mathbf{g}\,|\,\mathbf{b},\mathbf{s}_j) = \int \Lambda_{\mathrm{BKE}}(\mathbf{g}\,|\,\mathbf{b}(\vec{\theta}),\mathbf{s}_j)\,pr(\vec{\theta}\,|\,\mathbf{g},H_0)\;d\vec{\theta} \tag{4.7}$$

In this work, we assumed that the background, $\mathbf{b}(\vec{\theta})$, was parameterized by the object parameter vector, $\vec{\theta} = [n,p,q,l,A_{heart},A_{liver},A_{body}]$ that was a combination of discrete and continuous parameters: n, p, q and l were integer parameters specifying the object gender, body size, heart size and fat level and A_{heart}, A_{liver} and A_{body} were scalar parameters representing the total activity in the heart, liver and body respectively. Thus, the background $\mathbf{b}(\vec{\theta})$ given the object parameter vector $\vec{\theta}$ was represented as:

$$\mathbf{b}(\vec{\theta}) = A_{heart}\mathbf{prj}^{heart}_{n,p,q,l} + A_{liver}\mathbf{prj}^{liver}_{n,p,q,l} + A_{body}\mathbf{prj}^{body}_{n,p,q,l}, \tag{4.8}$$

where $\mathbf{prj}^{heart}$,$\mathbf{prj}^{liver}$ and $\mathbf{prj}^{body}$ are the projections of the of the heart, liver and the body (including other organs), respectively, filled with unit activity for a given anatomy.

Markov Chain Monte Carlo:

The integral in (4.7) can be estimated using standard Monte Carlo integration methods by generating many independent and identically distributed (i.i.d) samples of $\vec{\theta}$ from the posterior distribution, $pr(\vec{\theta}\,|\,\mathbf{g},H_0)$, and computing the sample mean of $\Lambda_{BKE}(\mathbf{g}\,|\,\mathbf{b}(\vec{\theta}))$. However, it is difficult to draw i.i.d samples from the posterior distribution $pr(\vec{\theta}\,|\,\mathbf{g},H_0)$ because the density function is usually complex or unknown. Markov Chain Monte Carlo (MCMC) techniques offer an alternative way to draw samples from the posterior distribution. We adopted a Metropolis–Hastings approach to draw samples $\vec{\theta}^{(0)},\vec{\theta}^{(1)},...,\vec{\theta}^{(k)},...\vec{\theta}^{(N)}$, where N is the number of iterations. For each $\vec{\theta}^{(k)}$, a proposed $\tilde{\vec{\theta}}$ is generated according to a symmetric and an easy to sample conditional distribution, $q\left(\tilde{\vec{\theta}}\,|\,\vec{\theta}^{(k)}\right)$, and is accepted with probability $\rho\left(\tilde{\vec{\theta}}\,|\,\vec{\theta}^{(k)}\right)$ given by:

$$\rho\left(\tilde{\bar{\theta}} \mid \vec{\theta}^{(k)}\right)=\min\left\{\frac{pr(\mathbf{g} \mid \tilde{\bar{\theta}}, H_0)\, pr(\tilde{\bar{\theta}})\, q\left(\tilde{\bar{\theta}} \mid \vec{\theta}^{(k)}\right)}{pr(\mathbf{g} \mid \vec{\theta}^{(k)}, H_0)\, pr(\vec{\theta}^{(k)})\, q\left(\vec{\theta}^{(k)} \mid \tilde{\bar{\theta}}\right)}, 1\right\}. \tag{4.9}$$

We used a proposal function, $q(.|.)$, like the one used [41]. This function was designed as a symmetric and variable-at-a-time function that is, in each iteration, the function randomly choses one parameter to propose. For the continuous parameters $\left(A_{heart}, A_{liver} \text{ and } A_{body}\right)$, the prior probabilities followed truncated Gaussian distributions with parameters shown in Table 4-1. However, the discrete parameters (*n, p, q* and *l*), defining the gender, body size, heart size and fat level thickness, were all considered to be equally likely.

The entire sampling procedure is described by the following.

Metropolis-Hasting algorithm for estimating $\Lambda_{\text{BKS}}(\mathbf{g} \mid \mathbf{b}, \mathbf{s}_j)$:

Step 0 (*initialization*): Choose length of "burn-in" period *M* and initial state $\vec{\theta}^{(0)}$. Set *k* = 0.

Step 1 (*candidate point*): Generate a candidate point $\tilde{\bar{\theta}}$ according to the proposal distribution $q\left(\tilde{\bar{\theta}} \mid \vec{\theta}^{(k)}\right)$.

Step 2 (*accept/reject*): Generate a random number $U \sim u(0,1)$. Set $\vec{\theta}^{(k)} = \tilde{\bar{\theta}}$ if $U \le \rho\left(\tilde{\bar{\theta}} \mid \vec{\theta}^{(k)}\right)$ (Metropolis-Hasting criterion). Otherwise set $\vec{\theta}^{(k+1)} = \vec{\theta}^{(k)}$.

Step 3 (*iterate*): Repeat Steps 1 and 2 until $\vec{\theta}^{(M)}$ is available. Terminate "burn-in" process and proceed to step 4 with $\vec{\theta}^{(k)} = \vec{\theta}^{(M)}$.

Steps 4–6 (*ergodic average*): Repeat process in Steps 2 and 3 and compute the ergodic average:

$$\widetilde{\Lambda}_{\mathrm{BKS}}\left(\mathbf{g} \mid \mathbf{b},\mathbf{s}_j\right) = \frac{1}{N-M}\sum_{k=M+1}^{N} \Lambda_{\mathrm{BKE}}\left(\mathbf{g} \mid \mathbf{b}\left(\vec{\theta}^{(k)}\right),\mathbf{s}_j\right) \tag{4.10}$$

The ergodic average $\widetilde{\Lambda}_{\mathrm{BKS}}\left(\mathbf{g} \mid \mathbf{b},\mathbf{s}_j\right)$ is an estimate of $\Lambda_{\mathrm{BKS}}(\mathbf{g} \mid \mathbf{b},\mathbf{s}_j)$.

The Metropolis-Hasting algorithm is an iterative approach that requires thousands of iterations to estimate the IO test statistics. In this work we used 50,000 iterations. It is often suggested, as we have done here, to discard the early outputs of the chain and not include them in the sum of step 6. This is because the choice of the initial state $\vec{\theta}^{(0)}$ biases the subsequent likelihood ratios and the amount of bias decreases with iteration. We discarded the first 20,000 iterations, which are referred to as the burn-in iterations in the MCMC literature. This ensures the stabilization of each Markov chain for the computation of $\widetilde{\Lambda}_{\mathrm{BKS}}\left(\mathbf{g} \mid \mathbf{b},\mathbf{s}_j\right)$. As suggested in [98], we targeted an acceptance rate of ~30% for $\rho\left(\tilde{\vec{\theta}} \mid \vec{\theta}^{(k)}\right)$ by adjusting the parameters of the proposal functions.

Step 2 requires generating the projection images $\mathbf{b}\left(\vec{\theta}^{(k)}\right)$ and $\mathbf{s}_j$. This is computationally demanding and is practically impossible to apply for realistic background distributions and system models using either analytic or Monte Carlo simulation approaches. To efficiently apply the MCMC IO estimation, we precomputed noise-free projection images $\mathbf{prj}_{n,p,q,l}^{heart}$, $\mathbf{prj}_{n,p,q,l}^{liver}$ and $\mathbf{prj}_{n,p,q,l}^{body}$. This constituted a database of 2(genders) × 3(heart sizes) × 3(fat levels) × 3(body sizes) = 54 different anatomies. For a given parameter vector, $\vec{\theta}^{(k)}$, we located the corresponding anatomy using the indexes n, p, q and l and the background image was then generated by scaling and summing the three organ projections together according to the values of A_{heart}, A_{liver} and A_{body}.

Figure 4-7 shows the likelihood ratios, $\Lambda_{\mathrm{BKS}}(\mathbf{g} \mid \mathbf{b},\mathbf{s}_j)$, for one sample input projection image as a function of the iteration number for the 30,000 iterations after the burn-in process. The input projection image simulated here had a perfusion defect at the antero-lateral wall of the heart (d_2). For the binary detection task, the test statistic, $t_d(\mathbf{g})$, to be used was the one corresponding to the d_2 defect. To compute the test statistic, $t_l(\mathbf{g})$, for the joint detection and localization task, we picked the maximum from the six likelihood ratios and used the location corresponding to that maximum. For the input projection simulated in Figure 4-7, the location would be correctly assigned to the anterolateral wall (d_2).

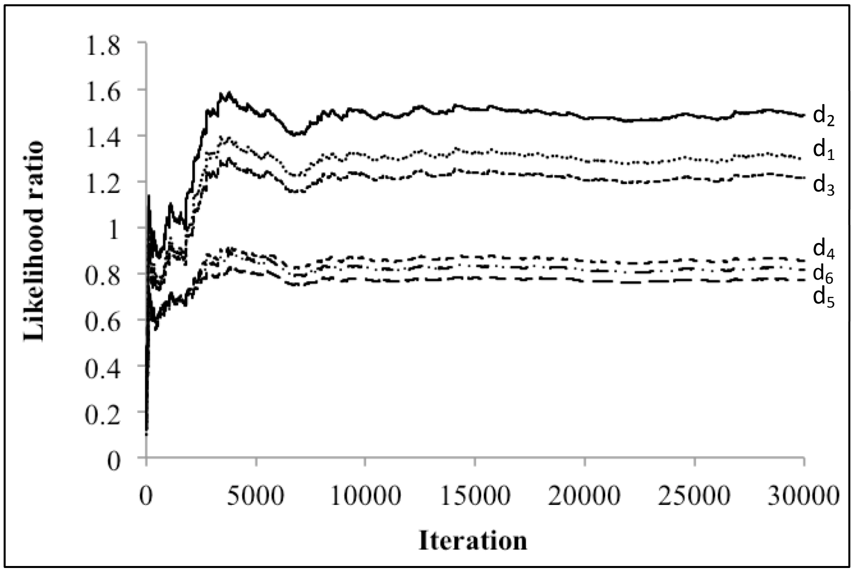

Figure 4-7. A plot of the likelihood ratio with iteration number for an input projection image with a perfusion defect located at the anterolateral wall (location d_2).

To perform the IO study for both tasks, we generated an ensemble of 540 pairs of noisy defect-present and -absent images. For each collimator and each defect location, we computed the IO test statistic using the MCMC method for the 540 images. For the joint detection and localization task, for each input projection image, we calculated six likelihood ratios: one for each of the different defect locations. We could then identify the largest among them, as described earlier, and select the corresponding defect location. The projection data contained a 64x24x60 pixel region of interest centered over the heart centroid. This ensured that the whole heart was included inside the region-of-interest. Using a larger region made the IO computation more intensive without changing performance.

The IO test statistics were then analyzed using ROC and LROC methodologies for the detection and joint detection and localization tasks, respectively. We used the area under the ROC and LROC curves (AUC_d and AUC_{d+l}) as the figures of merit to evaluate observer performance. We used the ROCkit code [99] which fits a binormal ROC curve to the input data, to estimate AUC_d. To calculate AUC_{d+l}, we constructed the LROC curve by sweeping the decision threshold across the distributions of defect-present and defect-absent test statistics. At each threshold, we calculated the percent correct localization and the false positive fraction pair. We then computed the area under the LROC curve using trapezoidal integration. We used bootstrapping methods to estimate the standard deviation of the AUC_{d+l}.

4.3 Results

4.3.1 Binary defect detection task

Figure 4-8 shows a plot of the AUC_d for the different collimators for the binary detection task. Note that the error bars are very small (~0.005). These data suggest that a collimator with a FWHM resolution of 0.9-1.1 cm (C_3-C_4) at 10 cm is optimal. We tested the statistical significance of the differences between the AUC_d values for the collimators C_2 to C_5 on a pair-wise basis. The tests indicated that the differences were statistically significant at 95% confidence level (all p-values were less than 10^{-15}) except for the difference between AUC_d values for C_3 and C_4 with a p-value equal to 0.178. A plot of the ROC curves for the standard collimator (C_2) and the optimal collimator (C_4) is shown in Figure 4-9. The ROC curves do not cross and the AUC is thus suitable as a figure of merit. We note that optimal collimators determined in this study tended to have poorer resolution and higher efficiency than the collimator C_2, which had resolution characteristics typical of those used for myocardial perfusion imaging, an effect seen by others using different task criteria [38, 84].

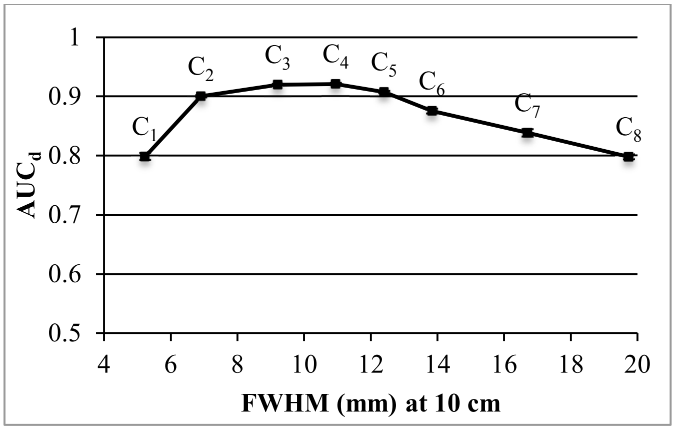

Figure 4-8. The ideal Observer performance measured in terms of AUC$_d$ for the different collimators.

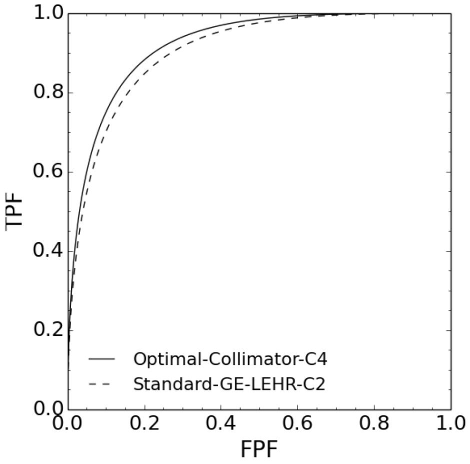

Figure 4-9. ROC curves for the optimal collimator (C_4) and the standard GE-LEHR collimator (C_2).

We also calculated the specificity for various sensitivities for the standard GE-LEHR (C_2) and the optimal collimator (C_4) (Table 4-4). The maximum difference between the specificities of the two collimators was 4% at the 90% sensitivity level.

Table 4-4. Sensitivity/Specificity pairs for the standard and optimal collimators

	Specificity (%)	
Sensitivity	Standard GE-LEHR (C2)	Optimal Collimator (C4)
80	84.1	86.6
82.5	82.1	84.8
85	79.5	82.6
87.5	76.6	80.1
90	72.8	76.8

4.3.1.1 Effect of perfusion defect location

We estimated the observer performance for each of the six defects and the corresponding optimal collimator, as shown in Table 4-5. It is clear that the optimal collimator was the same for individual defects and for the whole set of defects combined. The AUC values suggest that there was a great deal of difference in the amount of information about the absence or presence of a myocardial perfusion defect at the various defect locations. A likely reason for this is the difference in the number of detected photons from the different locations and the average distance of the defects to the face of the collimator, resulting in different image resolution and noise levels.

Table 4-5. IO performance measured in terms of AUC_d for the different defect locations

Defect location	AUC_d	Std. dev.	Optimal collimator
d_1	0.917	0.003	C_3-C_4
d_2	0.947	0.006	C_3-C_4
d_3	0.921	0.001	C_3-C_4
d_4	0.921	0.003	C_3-C_4
d_5	0.932	0.007	C_3-C_4
d_6	0.909	0.007	C_3-C_5

4.3.1.2 Effect of perfusion defect size

In this experiment, we evaluated the IO performance on the detection of perfusion defects of various sizes. We simulated perfusion defects with 5%, 10% and 25% extents, located at locations d_2 and d_5, as shown in Figure 4-5. As a reminder, the product of the extent and severity was kept constant to model constant overall reduction of the activity in the myocardium. For each collimator and defect, we computed the IO test statistics using the MCMC method for 1,080 images. As shown in Figure 4-10 and Figure 4-11, we observed significant and direct dependence of the optimal collimator on defect size: as the defect size decreased the optimal collimator shifted toward better resolution. This agrees with previous results as reported in [38].

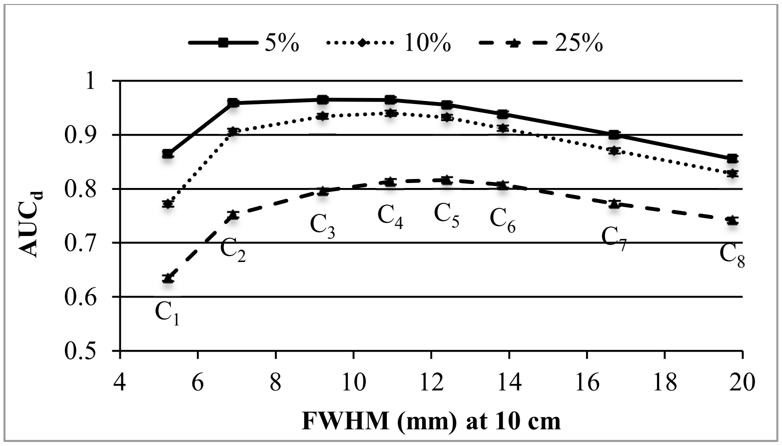

Figure 4-10. Observer performance in terms of AUC$_d$ for various defect sizes located at d_2.

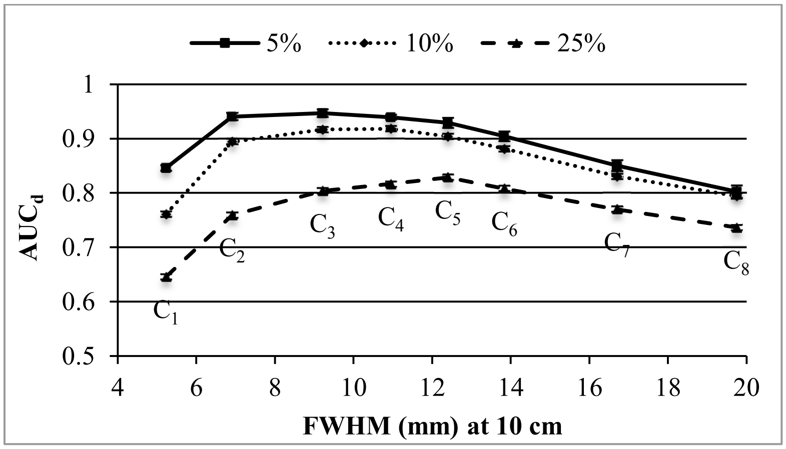

Figure 4-11. Observer performance in terms of AUC$_d$ for various defect sizes located at d_5.

4.3.1.3 Observer performance for different phantom sub populations

To investigate whether the optimal collimator depended on patient anatomical characteristics, we calculated AUC$_d$ for different sub populations, as shown in Figure 4-12. The figure also indicates the optimal collimator range for each sub population. The sub populations included phantoms having small, medium and large heart sizes, phantoms having small, medium and large adipose tissue levels and finally phantoms with small, medium and large body sizes. We note that the IO performance improved as the number of detected counts from the heart increased as well as when the size of the heart increased. This applies to the cases when assessing the observer performance for the various heart sizes. In addition, the observer performance decreased as the adipose tissue thickness increased, resulting in fewer detected counts from the heart and a larger distance from the detector to the heart. For larger body sizes, increased attenuation and scatter inside the body and poorer resolution, due to the increased distance from the heart to the face of the collimator, would degrade image quality. It is worth noting that in the digital phantom population used here [1], the heart size varied in proportion to body size. For example, a medium-sized heart in a medium sized phantom was larger than a medium-sized heart in a small sized phantom and smaller than that in a large sized phantom. This compensated for the increased attenuation in the larger phantoms and thus resulted in more counts acquired from the heart for larger phantoms than for smaller phantoms.

We note that fat thickness had an impact on the choice of the optimal collimator. For phantoms with the small adipose tissue thickness, the optimal collimator range was C_3 to C_5, while for the larger fat thicknesses the optimal collimator was C_3.

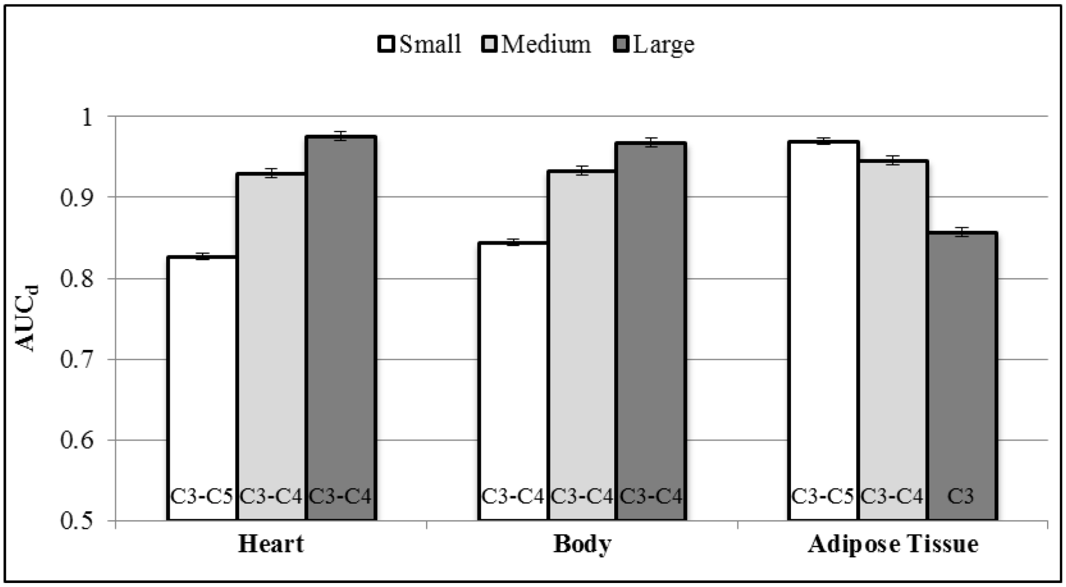

Figure 4-12. AUC_d values for the different sub populations.

4.3.2 Joint perfusion defect detection and localization task

Figure 4-13 shows the IO performance, measured in terms of AUC_{d+l} for the different collimators. This suggests that a collimator with a resolution of 0.9 cm FWHM (C_3) at 10 cm was optimal. We tested the statistical significance of the differences between the AUC_{d+l} values for the collimators C_2 to C_4 on a pair-wise basis. The tests indicated that the differences were statistically significant at a 95% confidence level (all p-values were less than 10^{-14}). This is similar to what was suggested by the observer for the binary detection task. This result suggests that the optimal collimator for both tasks was similar. This agrees with the results of Zhou et al. [38]. However, for the binary detection task, the observer performance on reading images acquired using C_4 collimator was optimal. For the joint detection and localization task, the IO performance was more peaked at C_3, and there was an increasing penalty for choosing collimators with poorer resolution. This same effect has been reported in [100].

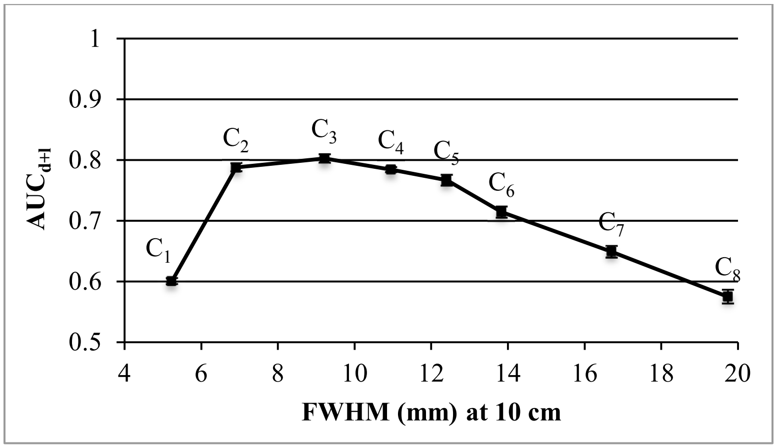

Figure 4-13. The ideal Observer performance measured in terms of AUC_{d+l} for the different collimators.

Table 4-6 shows the contingency table for the assignment of the different defects to the different locations. The vertical direction denotes the true location of the defect and the horizontal denotes the assigned location. The IO had the greatest success rate for assigning perfusion defects at location d_3. We also notice that the maximum failure rate occurred for either the super or sub-diagonal entries of the contingency table. This indicates that incorrect localization was generally to one of the neighboring defect locations.

Table 4-6. Contingency table in percent for collimator C_3.

	d_1	d_2	d_3	d_4	d_5	d_6
d_1	89.6	5.2	2.2	0.9	2.0	0.0
d_2	1.3	89.3	5.2	0.7	3.1	0.4
d_3	0.2	1.1	95.4	1.3	1.3	0.7
d_4	0.6	0.0	3.1	91.9	3.9	0.6
d_5	0.4	0.0	1.3	7.2	88.5	2.6
d_6	0.7	0.4	3.5	4.1	7.8	83.5

4.3.3 Computational cost

In this section, we report the computation times required to perform the experiments conducted in this Chapter. The times required to calculate the test statistics for one image were about 14 and 25 minutes for the detection and joint detection and localization tasks, respectively. (Note that for the joint task, we calculated six likelihood ratios, one for each of the different defect locations.) Thus, the calculations presented here required a total of 4.76 CPU years. A breakdown of the simulation times is as shown in Table 4-7. The CPU times are for a single core of a 2.33GHz Intel Xeon E5410 quad core processor. Not included in these times are the time required to generate the projection library database and the table of collimator detector response functions for each collimator.

Table 4-7. A breakdown of the simulation times

	Binary detection	Joint detection and localization
Noise realizations	540	540
Defect status	2 (present and absent)	2
Defects	10 (d_1-d_6 plus 2 additional defect sizes at locations d_2 and d_5)	6 (d_1-d_6)
Collimators	8	8
Required time to calculate the likelihood ratio for one image	~14 minutes	~25 minutes
Total required time (years)	2.3	2.46

4.4 Discussion

This Chapter describes a collimator optimization procedure for defect detection, as well as defect detection plus localization tasks, in the context of MPS imaging. Our results suggest that collimators with somewhat poorer resolution than a commonly used SPECT collimator appear optimal for the task of defect detection in MPS. A difference of 0.02 in the AUC_d values of the reported optimal collimators and the standard collimator was statistically significant. While this change in AUC may seem small, to put it in clinical perspective, this is the same difference in the AUC_d for MPS with and without attenuation compensation reported in [47]. Nevertheless, these results indicate that the standard GE-LEHR collimator is nearly optimal, especially for smaller perfusion defects and for the case when defect localization is of interest.

We used a simplified version of the joint detection and localization task in which the defect could appear only in one of six different locations distributed over a mid-ventricular slice of the heart. Furthermore, we did not apply the notion of search tolerance ordinarily used in LROC studies. The addition of more defect locations or search tolerance would be computationally expensive. Of note, MPS images are usually interpreted in territories and sub-territories [101]. In a clinical search scenario, the task is not to identify the precise position of the defect, but to localize it in some territory of the coronary artery structure. This is different than the clinical search in tumor imaging, in which accurate localization of the tumor is essential. For computational reasons, we also limited the number of defects. Furthermore, we chose a mid-ventricular slice and the six locations mimic the six segments that are clinically used to interpret this plane, as depicted in Figure 4-3.

We investigated a single injected activity of Tc-99m of 10mCi. This corresponds to the usual clinical injected activity that is administered to a patient for the first study in a one-day stress/rest protocol. In this protocol, the diagnostic outcome of the low-dose stress scan determines the necessity of calling for the high-dose rest scan. If the patient has normal stress study it is a trend in many practices to forego the rest study and thus avoid the additional radiation exposure. However, a higher injected activity would certainly affect the noise levels of the projection and reconstructed SPECT images, and consequently could result in a different optimal collimator than the ones reported here.

We investigated a family of eight parallel-hole collimators that spanned a wide range of sensitivity and resolution tradeoffs. We chose the collimator parameters to maximize the sensitivity for each selected resolution, while fixing the single septal penetration (SSP) probability at 140 keV to 0.3%. Other septal penetration probabilities might give different optimal results than those reported in this Chapter. Investigating the optimal septal penetration probability would, however, have been highly computationally intensive. Of note, a previous study of two collimators with vastly different septal penetration fractions indicated relatively little difference in image contrast [102].

We used the IO operating on projection data to find the optimal collimator that would preserve the maximum possible information in the sinogram, regardless of the reconstruction method used to convert the sinogram into images suitable for human interpretation. We note that a given reconstruction method may or may not make optimal use of the sinogram information and thus affect observer performance and the choice of the optimal collimator. It has been advocated that joint (simultaneous) optimization of collimator and reconstruction methods yields better detection/estimation task performance than the sequential approach, in which the collimator is optimized using the projection data, for various tasks such as defect detection, and estimation tasks [78, 103]. In the cited studies, it was reported that the optimal collimators had higher resolution than those identified when optimizing using only the raw projection data (i.e., when not considering the reconstruction method). In a previous study [4], we demonstrated that, for a detection task, when a good model of the image formation process is incorporated into the reconstruction algorithm, the IO yielded similar optimal operating ranges as those obtained using the CHO. In this study we took advantage of the fact that accurate models of the collimator-detector response for Tc-99m are readily available, which permitted us to avoid the computationally expensive joint acquisition and reconstruction optimization, and performed the collimator optimization in this study using the raw projection data.

4.5 Conclusions

We performed defect detection and defect detection and localization task-based collimator optimization in the context of MPS using the IO operating on a realistic simulated population of BKS/SKE data. This represents a clear step forward in the use of clinically realistic IO-based optimization. Our results indicate that poorer resolution collimators than standard collimators, such as the GE-LEHR collimator, are optimal for the range of defect sizes studied. The results showed that the optimal collimator was the same for the individual defects and for the whole set of defects combined together. We observed significant and direct dependence of the optimal collimator on defect size: as the defect size decreased, the optimal collimator shifted toward better resolution. It was also noted that the optimal collimator for both tasks was similar, though the detection-localization task tended to prefer a collimator with somewhat higher resolution. The improvement in the area under the ROC curve for the detection task was about 0.02, providing a 4% increase in specificity at 90% sensitivity compared to a typical LEHR collimator. While these results do demonstrate the potential for some improvement, they also indicate that typical LEHR collimators are near-optimal for MPS.

5. Collimator and reconstruction optimization in MPS using the ideal observer with and without model mismatch and an anthropomorphic model observer

5.1 Introduction

In SPECT imaging, reconstructed image quality is affected by a host of physical, instrumentation, and patient-generated degrading factors. Accordingly, compensating for these factors typically results in improved quantification and better performance on a variety of tasks. The collimator-detector response (CDR) including the geometric, septal penetration and scatter, and the detector intrinsic resolution components, is the primary factor that determines the spatial resolution of SPECT images. The design of the collimator is the primary factor determining the resolution-noise tradeoff in the image data and thus is an important determinant of image quality.

The CDR function (CDRF) describes the probability that photons emitted from a point source in space will be detected at some point in the detection plane. The CDRF can be decomposed into 4 components that affect the quality of SPECT images. The intrinsic response function (IRF) describes the response of the detector to a perfectly collimated point source; its integral represents the efficiency of the detector. The IRF is determined by the uncertainty in position estimation, which, for a scintillation camera, is due to the statistical variation of the estimated interaction position in the crystal. For such cameras the intrinsic resolution can be well modeled as a Gaussian function and is typically assumed to be invariant across the detector surface.

The other 3 components of the CDRF depend on the collimator characteristics and the photon energy. This includes the geometric (GRF), septal penetration (SPRF) and septal scatter (SSRF) response functions that describe the probabilities that photons emitted from a point source and pass through the collimator holes, penetrate the septa, or scatter in the septa, respectively. All of these components are spatially varying. The GRF can be modeled analytically by calculating a distance dependent response function that is typically averaged in the direction parallel to the detector surface [104]. CDR can be modeled in an iterative reconstruction algorithm [105-107]. Reconstruction-based compensation has been shown to provide accurate quantitation [108] and improved lesion detection in the context of thoracic Ga-67 citrate SPECT [109]. The SPRF and SSRF are difficult to treat analytically and must be modeled using Monte Carlo (MC) simulation techniques.

The relative importance of these components largely depends on the collimator parameters and the energy of the incident photons. For example, for a collimator with a relatively small aspect ratio, defined as the ratio of hole length to the hole size, septal scatter and penetration are non-negligible factors and potentially important. In this work, we are interested in comparing three different CDR compensation schemes including modeling the full CDR, geometric response only and the case when no CDR model was used, for a family of collimators that spans a wide range of sensitivity and resolution tradeoffs. We have also investigated the optimal collimator when using each of the CDR compensation methods.

It is important to optimize the resolution-sensitivity tradeoff and compare the different compensation methods for a given diagnostic task such as estimation, i.e., quantifying parameters of interest using the given image data [75-77], or classification, i.e., deciding to which class a patient belongs based on an image [38, 40, 77, 79-85]. In this work, we focus on a binary defect detection task in which an observer is asked to classify a given image as either containing or not containing a defect. In this work, we used 2 classes of model observers: the Ideal Observer (IO) and its extension, the Ideal Observer with Model Mismatch (IO-MM) [3, 4] operating on projection images and an anthropomorphic model observer, the Channelized Hotelling Observer (CHO) [43] to assess the performance of the human observers on reconstructed images.

The IO outperforms all other observers and sets an upper limit on task performance, as measured by figures of merit such as the area under the receiver operating charectersitic (ROC) curve (AUC) [24]. It makes optimal use of all the information in the raw data. However, it requires full knowledge of the raw data statistics. Therefore, it is typically applied in the projection domain, where the noise statistics are known and easy to analyze analytically. Moreover, IO performance is not altered by linear operations on the raw data such as linear filtering or reconstruction [24].

Anthropomorphic model observers, such as the CHO [43], are designed to model human task performance. They have been extensively used in the evaluation and optimization of acquisition, instrumentation, reconstruction and compensation methods in the context of myocardial perfusion, bone, and prostate SPECT [45-47]. The CHO has shown good agreement with human observers in a variety of clinical applications and tasks [44-52]. The CHO is typically applied to reconstructed images, and thus, for a fair comparison, requires optimization of reconstruction and regularization parameters (e.g., iteration number and cutoff frequency of post-reconstruction smoothing filters). Optimizing imaging systems in the projection domain using the IO is appealing in part because it avoids the need to select and optimize the reconstruction algorithm.

Despite the potential advantages of using the IO, it has rarely been rigorously applied to real imaging tasks due to the technical difficulty of estimating the performance for cases of realistic background variability arising from variations in patient anatomy and uptake. Typically, application of the IO has been limited to cases where the background and signal models are simple [38-40]. To overcome this limitation, methods based on Markov Chain Monte Carlo (MCMC) techniques have been developed and applied to estimate the IO test statistic, i.e., the likelihood ratio (LR), for realistic and general backgrounds and signal models [33, 34, 41].

Another difficulty in evaluating and optimizing imaging systems using the IO is that since the IO has full knowledge of all the statistical information about the background and signal, it implicitly has a perfect model of the image formation process including all physical processes and factors that degrade image quality (e.g., finite energy resolution, scatter, attenuation, CDR). One way to think about this is that the models embedded in the IO perfectly match the models used to form the projection images, $p_t(.)$ (Figure 5-1), which is equivalent to saying the IO does perfect compensation for all physical processes and factors that degrade image quality. Real reconstruction and compensation algorithms do not perfectly model the image formation process and, in fact, many physical effects are not even compensated for at all. The difference between the true (complete and accurate) model, $p_t(.)$, and that used in reconstruction, $p_m(.)$, is referred to as model mismatch (MM). This mismatch is one reason why the IO may not always give the same optimal parameters as human observers when operating on images reconstructed with imperfect or incomplete system models. In a sense, the IO can be conceptualized as providing ideal (perfect) compensation for the various image degrading effects, and the task performance it achieves reflects the best achievable with perfect compensation.

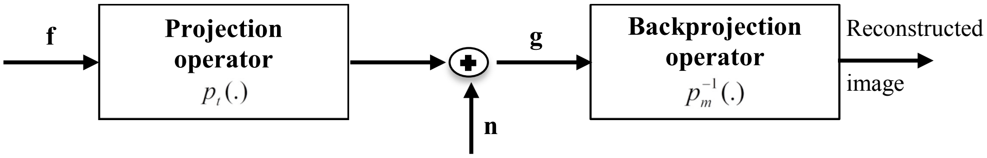

Model Mismatch: MM = $p_t(.) - p_m(.)$

Figure 5-1. A schematic diagram of the image formation process and the definition of model mismatch term

We have previously introduced the concept of including MM into the IO framework [3, 4]. The IO-MM still uses the LR as the test statistic, but in the estimation of the LR it uses an approximate model of the image formation process ($p_m(.)$) instead of the true one ($p_t(.)$). In [4], we compared the performance of the IO and IO-MM with that of the CHO for the task of optimizing the energy window for myocardial perfusion SPECT imaging. The IO-MM showed good agreement with the CHO. We have also applied the IO and IO-MM to optimize the energy window for Y-90 bremsstrahlung SPECT for a detection task [110]. The optimal acquisition window was narrower when taking into account model-mismatch, and was similar to that previously obtained when optimized for an estimation task [71].

In this work, we evaluated the performance of the IO (i.e. the IO had perfect model of CDR) and IO-MM in cases where the IO-MM had (1) no model or (2) a model of the GRF only. We investigated and compared the optimal collimator for each compensation method. We also compared the performance of the IO and IO-MM to an anthropomorphic observer (CHO) applied to Ordered-Subset Expectation-Maximization (OS-EM) reconstructed images for the same compensation methods.

5.2 Methods

In this section, we introduce the key elements of task based image quality assessment, including the task, object, imaging system models, observer and figure of merits. We revisit the concept of MM and give a brief overview of the IO, its estimation with MCMC methods and the introduction of MM into the IO. Finally, we give a brief introduction of the CHO that is used as a surrogate for human observer performance.

5.2.1 Identification of the task

In this work, we focused on the task of detecting a fixed signal in a randomly varying background in the context of MPS. In a binary decision detection task, the observer is asked to classify a given image as either containing or not containing a signal, which in this case was a myocardial perfusion defect.

5.2.2 Object and imaging system models

It has been previously reported that variability in patients' anatomy and activity uptake are important factors that limit task performance. It is thus important that the object model incorporates clinically realistic variability in anatomy and uptake. To this end, we have previously designed and developed a digital phantom population based on the 3D eXtended CArdiac Torso (XCAT) phantom [1]. The population consists of 54 phantoms, including anatomical models for both genders and 3 (small, medium and large) body habitus, subcutaneous adipose tissue thicknesses, and heart sizes. The anatomical parameters of the phantom population were obtained from the Emory Cardiac Database (Barclay, Emory University) that included anatomical measurements from 166 patients who underwent MPS imaging [96].

We simulated anterolateral and inferior perfusion defects with variable extents and severities as shown in Table 5-1. The extent and severity were defined as the fraction of the left ventricular myocardial volume and reduction of uptake in the perfusion defect relative to the normal myocardium, respectively. The extent and severity of the defect were chosen to be challenging and clinically relevant, and their product was kept constant to model constant reduction of the activity in the myocardium. Figure 5-2 shows short axis images of hearts with defects in either the anterolateral or inferior wall.

Table 5-1. Simulated defects parameters

Defect	Location	Extent (%)	Severity (%)
$d_{A,1}$	Anterolateral	5	50
$d_{I,1}$	Inferior	5	50
$d_{A,2}$	Anterolateral	10	25
$d_{I,2}$	Inferior	10	25
$d_{A,3}$	Anterolateral	25	10
$d_{I,3}$	Inferior	25	10

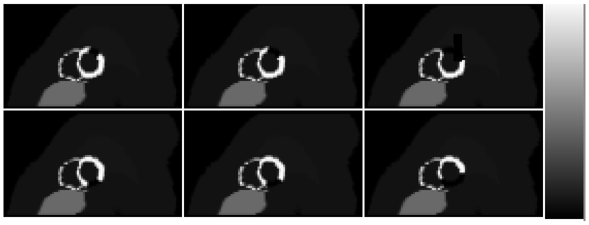

Figure 5-2. Sample short axis images showing hearts with defects present in the anterolateral (top) and inferior (bottom) myocardium with extents of 5%, 10% and 25% from left to right. For illustrative purposes, defects shown have 100% severity.

We investigated a family of eight parallel hole collimators, labeled C_1 to C_8, spanning a wide range of sensitivity and resolution tradeoffs, as shown in Figure 5-3. The parameters of collimator C_2 were chosen to match the resolution and sensitivity of the GE-LEHR collimator, a standard collimator commonly used in our clinic for MPS imaging. We used standard formulas to calculate the collimator parameters for each given resolution [74, 77]. The hole-length was 32 mm for all collimators, which was the hole-length that maximized the sensitivity for a penetration criterion of 0.3% at 140 keV. In Chapter 4, we optimized over the same family of collimators in the context of MPS using the IO for a joint detection and localization task. Figure 5-4 shows sample noise-free and noisy projection images for the different collimators.

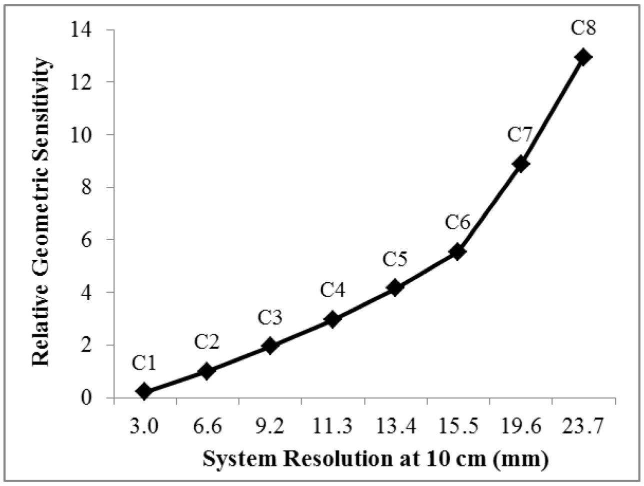

Figure 5-3. Plot of the resolution-sensitivity tradeoff for the collimators investigated in this study. The resolution is the total system FWHM resolution 10 cm and geometric sensitivity is relative to that of the GE-LEHR collimator (C_2).

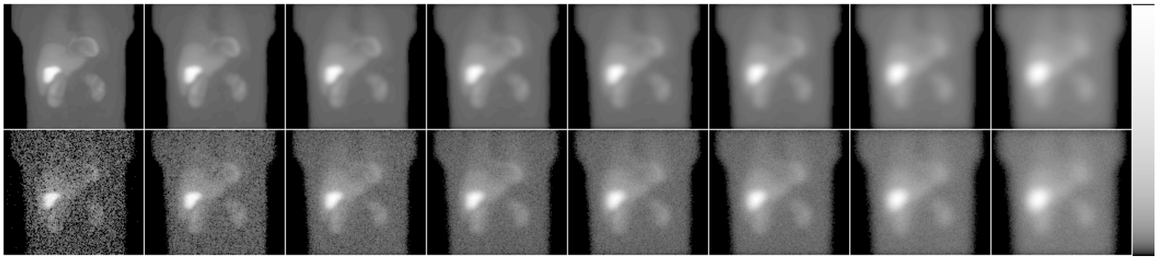

Figure 5-4. Noise-free (top) and noisy (bottom) projection images obtained using collimators C_1 to C_8 (from left to right). From left-to-right note the decreasing noise and sharpness of the images, as expected. Images were displayed using a logarithmic map to better show the low activity organs.

To compare between the different CDR compensation methods, for each collimator, projections of the phantom population were simulated using an analytical projector that modeled attenuation (A), scatter (S) and three CDR models. The three models studied were (1) F (full CDR including geometric, septal penetration and septal scatter response components) using pre-calculated CDRF tables obtained from MC simulations, (2) G (geometric response) using distant-dependent Gaussian functions and (3) N (no model). We modeled a GE Infinia dual-head SPECT system with a 9.5 mm thick NaI(Tl) crystal. We simulated non-circular body-contouring orbits and projections acquired at 60 equispaced angles over a 180° acquisition arc extending from 45° right anterior oblique to 45° left posterior oblique. Projection images were binned in a 128x114 matrix with a pixel size of 0.442 cm.

We separately generated noise-free Tc-99m projection data for the heart, liver, and body (including all other organs) for each phantom. This enabled us to separately scale the individual projection images of the different organs using random scale factors obtained from distributions that were based on data from a set of 34 patients who underwent MPS. We could then sum the scaled projections before simulating Poisson noise to generate an uptake realization. In this study, we modeled an injected activity of 10mCi of Tc-99m sestamibi. Figure 5-5 shows noise-free projection images for the different collimators and the various CDR modeling methods.

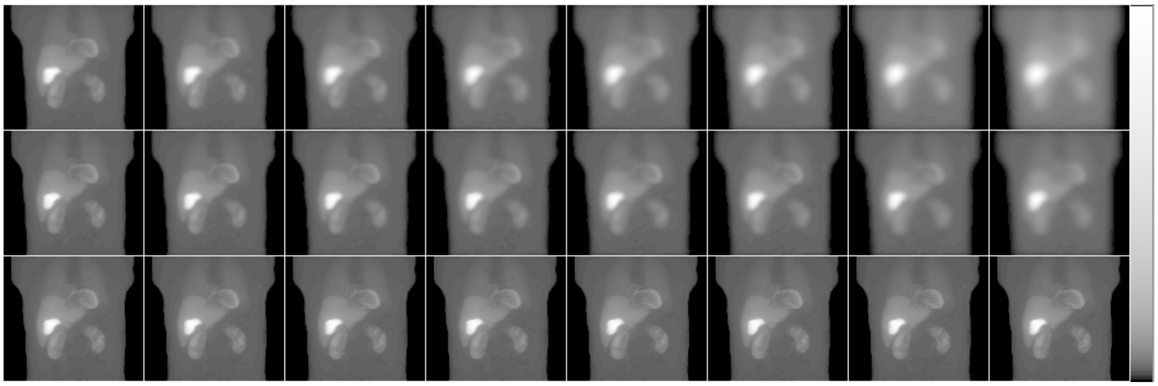

Figure 5-5. Sample noise-free projection images using the collimators C_1 to C_8 (from left to right) when modeling the full CDR (top), the GRF only (middle) and no CDR modeling (bottom). Images were displayed using a logarithmic map to better show the low activity organs.

5.2.3 Observer models

5.2.3.1 Application of the Ideal Observer (IO) and the Ideal Observer with Model Mismatch (IO-MM)

In SPECT imaging, given a continuous object, **f**, the projection data, **g**, are the result of the image formation process, and can be represented by:

$$\mathbf{g} = p_t(\mathbf{f}) + \mathbf{n}, \tag{5.1}$$

where $p_t(.)$ is a continuous-to-discrete projection operator that maps the object, **f,** to the projection space and **n** is the measurement noise.

In this work, we consider the task of detecting a fixed signal, $\mathbf{f}_s$, such as a perfusion defect, in a random background, $\mathbf{f}_b$. We define the background and signal projection images as:

$$\mathbf{b}_t = p_t(\mathbf{f}_b), \tag{5.2}$$

$$\mathbf{s}_t = p_t(\mathbf{f}_s). \tag{5.3}$$

For the binary detection task under consideration, the two hypotheses to be tested can be written as:

$$H_0: \ \mathbf{g} = \mathbf{b}_t + \mathbf{n},$$

$$H_1: \ \mathbf{g} = \mathbf{b}_t + \mathbf{s}_t + \mathbf{n},$$

where H_0 and H_1 mean signal absent and signal present, respectively.

The IO uses the likelihood ratio, $\Lambda(\mathbf{g})$, of defect-present vs. defect-absent as the test statistic. For the case where the background and signal are known exactly (SKE/BKE) and the only source of randomness is Poisson measurement noise, $\mathbf{n}$, the expression for the likelihood ratio is given by:

$$\Lambda_{\mathrm{BKE}}\left(\mathbf{g},\mathbf{b}_{\mathrm{t}}\right)=\frac{pr(\mathbf{g}\,|\,H_1)}{pr(\mathbf{g}\,|\,H_0)}=\prod_{\mathrm{i}}\left(1+\frac{\mathrm{s_t}\left(\mathrm{i}\right)}{\mathrm{b_t}\left(\mathrm{i}\right)}\right)^{\mathrm{g(i)}}\exp\left(-\mathrm{s_t}\left(\mathrm{i}\right)\right) \tag{5.4}$$

For a signal known exactly embedded in a background known statistically (SKE/BKS), the expression for the likelihood ratio is given by:

$$\Lambda_{\mathrm{BKS}}\left(\mathbf{g}\right)=\int\Lambda_{\mathrm{BKE}}(\mathbf{g},\mathbf{b}_t)\ \mathrm{pr}(\mathbf{b}_t\,|\,\mathbf{g},H_0)\mathrm{d}b \tag{5.5}$$

The idea of equation (5.5) is to average over the backgrounds sampled randomly from the posterior density $\mathrm{pr}(\mathbf{b}_t\,|\,\mathbf{g},H_0)$. However, the density $\mathrm{pr}(\mathbf{b}_t\,|\,\mathbf{g},H_0)$ is usually not known analytically and is hard to sample from using standard Monte Carlo integration method. Accordingly, methods based on Monte Carlo Markov Chain techniques have been developed to estimate the integral in (5.5) [33, 41].

We applied a previously developed method to efficiently estimate the likelihood ratio [41]. We parameterized the object with a parameter vector, $\vec{\theta}$, which was a combination of discrete anatomical parameters, *n*, *p, q* and *l* that specify the object gender, body size, heart size and fat level, respectively, and continuous organ activity parameters, A_{heart}, A_{liver} and A_{body}, corresponding to the uptake activities of the heart, liver and body, respectively. Thus, the background $\mathbf{b}_t(\vec{\theta})$ parameterized by the vector $\vec{\theta}$ was represented as:

$$\mathbf{b}_t\left(\vec{\theta}\right)=A_{\mathrm{heart}}\ \mathbf{prj}_{n,p,q,l}^{\mathrm{heart}}+A_{liver}\ \mathbf{prj}_{n,p,q,l}^{\mathrm{liver}}+A_{body}\ \mathbf{prj}_{n,p,q,l}^{\mathrm{body}}\ , \tag{5.6}$$

where $\mathbf{prj}^{\mathrm{heart}}$, $\mathbf{prj}^{\mathrm{liver}}$ and $\mathbf{prj}^{\mathrm{body}}$ were the projections of the heart, liver and the body, respectively, filled with unit activity for a given anatomy. It has been shown that, if $\mathbf{b}_t\left(\vec{\theta}\right)$ has a one-to-one relation with the parameter vector $\vec{\theta}$, the integral in (5.5) can be expressed as:

$$\Lambda_{\mathrm{BKS}}\left(\mathbf{g}\right)=\int \Lambda_{\mathrm{BKE}}(\mathbf{g},\mathbf{b}_t(\vec{\theta}))\ \mathrm{pr}(\vec{\theta}\,|\,\mathbf{g},H_0)\mathrm{d}\vec{\theta} \tag{5.7}$$

Adopting a Metropolis–Hastings approach to draw samples from the posterior distribution $pr(\vec{\theta}\,|\,\mathbf{g},H_0)$, we could then compute the ergodic average $\widetilde{\Lambda}_{\mathrm{BKS}}\left(\mathbf{g}\right)$.

To take into account the "mismatch" between the models used in reconstruction and the real physical process, we incorporated the mismatch into the IO. For the IO-MM and a binary decision task, the two hypotheses to be tested can be presented mathematically by:

$$H_0^*:\ \mathbf{g}=\mathbf{b}_m+\mathbf{n},$$

$$H_1^*:\ \mathbf{g}=\mathbf{b}_m+\mathbf{s}_m+\mathbf{n},$$

where **g** was the input projection image generated using (5.1) and the background and signal projection images $\mathbf{b}_m$ and $\mathbf{s}_m$, respectively, were defined as:

$$\mathbf{b}_m=p_m(\mathbf{f}_b), \tag{5.8}$$

$$\mathbf{s}_m=p_m(\mathbf{f}_s). \tag{5.9}$$

For the IO-MM, the expression of the likelihood ratio for the SKE/BKE case is given by:

$$\Lambda_{\mathrm{BKE,m}}\left(\mathbf{g},\mathbf{b}_{\mathrm{m}}\right)=\frac{pr(\mathbf{g}\,|\,H_1^*)}{pr(\mathbf{g}\,|\,H_0^*)}=\prod_{\mathrm{i}}\left(1+\frac{\mathrm{s_m}\left(\mathrm{i}\right)}{\mathrm{b_m}\left(\mathrm{i}\right)}\right)^{\mathrm{g(i)}}\ \exp\left(-\mathrm{s_m}\left(\mathrm{i}\right)\right). \tag{5.10}$$

When background variability is included, the expression of the likelihood ratio is given by:

$$\Lambda_{\mathrm{BKS,m}}\left(\mathbf{g}\right)=\int \Lambda_{\mathrm{BKE,m}}(\mathbf{g},\mathbf{b}_m)\ \mathrm{pr}(\mathbf{b}_m\,|\,\mathbf{g},H_0)\mathrm{d}b. \tag{5.11}$$

To compute the likelihood ratio for the IO-MM, we followed the same methodology as for the case of the IO. We parameterized the object with the parameter vector, $\vec{\theta}$, applied the MCMC method to sample from the posterior distribution, $pr(\vec{\theta}\,|\,\mathbf{g},H_0)$, and computed the ergodic average $\widetilde{\Lambda}_{\mathrm{BKS,m}}(\mathbf{g})$.

For the standard IO, we tested the hypothesis that a projection image **g** contained or did not contain a fixed defect in a random background where both the signal and the background images were generated using the true model of the image formation process. Thus, the IO had a perfectly matched model of all physical image-degrading processes. For the IO-MM, we tested the same hypothesis. However, the signal and the background images were generated using an approximate ("mismatched") model $p_m(.)$ of the image formation process.

For each collimator, we computed IO and IO-MM test statistics. The IO had, by definition, a model of all image-degrading factors, so we denoted it as IO-ASF (A and S stand for the inclusion of attenuation and scatter modeling, respectively). The IO-MM had either no model of the CDR (IO-MM-ASN) or a GRF model only (IO-MM-ASG). To generate the test statistics, we used the MCMC method for an ensemble of 6,480 pairs of defect-present and defect-absent projection images modeling different anatomical and uptake variations. The projection data were contained within a 64x24x60 pixel volume of interest centered over the heart centroid. This ensured that the whole heart was included inside the volume-of-interest. For each collimator, the IO and IO-MM test statistics were used as the input to the ROCkit code [99], which fits a binormal ROC curve to the input data to estimate the AUC value.

5.2.3.2 Application of the Channelized Hotelling Observer

We used an anthropomorphic CHO as a surrogate for human observer performance, and compared performance for the various collimators and the CDR compensation methods to those obtained from the IO and the IO-MM. We performed CHO studies on images reconstructed using the Ordered-Subsets Expectation-Maximization (OS-EM) algorithm for three combinations of compensations: (1) attenuation, scatter and full CDR modeling (CHO-ASF); (2) attenuation, scatter and spatially varying geometric response (CHO-ASG); and (3) attenuation, scatter and no CDR modeling (CHO-ASN). For CHO-ASF and CHO-ASG compensation methods, images for the first 10 iterations were saved for collimators C_1 to C_5, images for the first 20 iterations were saved for C_6, and images for the first 30 iterations were saved for collimators C_7 and C_8. Higher iterations with methods that included modeling either the full CDR model or the GRF only and lower resolution collimators were saved due to the fact that these reconstructions tend to converge more slowly. For CHO-ASN, we saved the first 10 iterations for all collimators since convergence was rapid. . We used twelve subsets with five projections/subset in the OS-EM algorithm. Figure 5-6 shows sample transaxial slices from images reconstructed using the different CDR compensation methods.

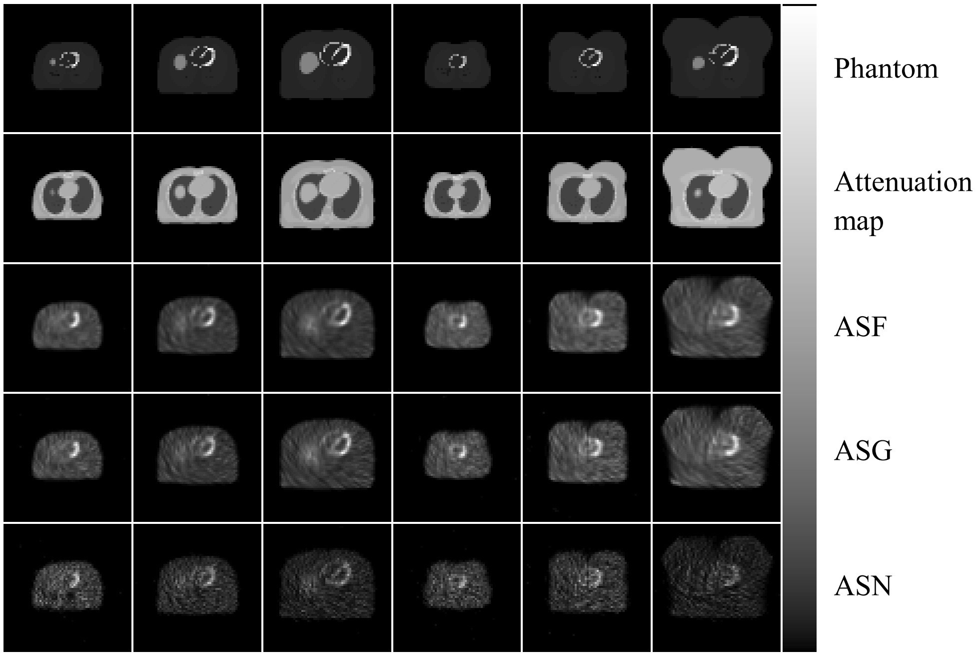

Figure 5-6. Sample transaxial images containing the center of mass of the heart centroid for different phantoms and the corresponding attenuation maps (rows 1 and 2). Rows 3 to 5 show the corresponding reconstructed image slices using collimator C_2 and ASF, ASG and ASN compensation methods after 36 updates.

For each collimator and the compensation methods ASG and ASN, we simulated 20 pairs of input projection images per defect per phantom, leading to a total of 6480 pairs of defect-present and defect-absent images. For the ASF compensation method, we limited the number of input projection images to 5 pairs per defect per phantom, leading to a total of 1620 pairs. We chose a smaller number of pairs because of the computational cost associated with incorporating the full CDR model into the reconstruction For each iteration, images were filtered using a low pass Butterworth filter with order 8 and cutoff frequencies of 0.08, 0.1, 0.12, 0.14, 0.16, 0.2 and 0.24 pixel^{-1}. We then extracted the short axis image containing the center of the defect and applied the CHO. In this study, we used four non-overlapping difference-of-mesa frequency channels with successively doubling widths and a starting frequency of 0.5 pixel^{-1}.

We estimated CHO performance using a leave-one-out technique in which the CHO was trained using all but one image and tested using the left-out image, producing one test statistic value. This process was repeated with each of the feature vectors being left out, resulting in a set of test statistics with as many elements as images. These test statistics were used as the input to the ROCkit code [99], to estimate the AUC. For each collimator and compensation method, the iteration and cutoff frequency giving the highest AUC were selected as optimal. A schematic diagram showing the steps of the CHO study is shown in Figure 5-7.

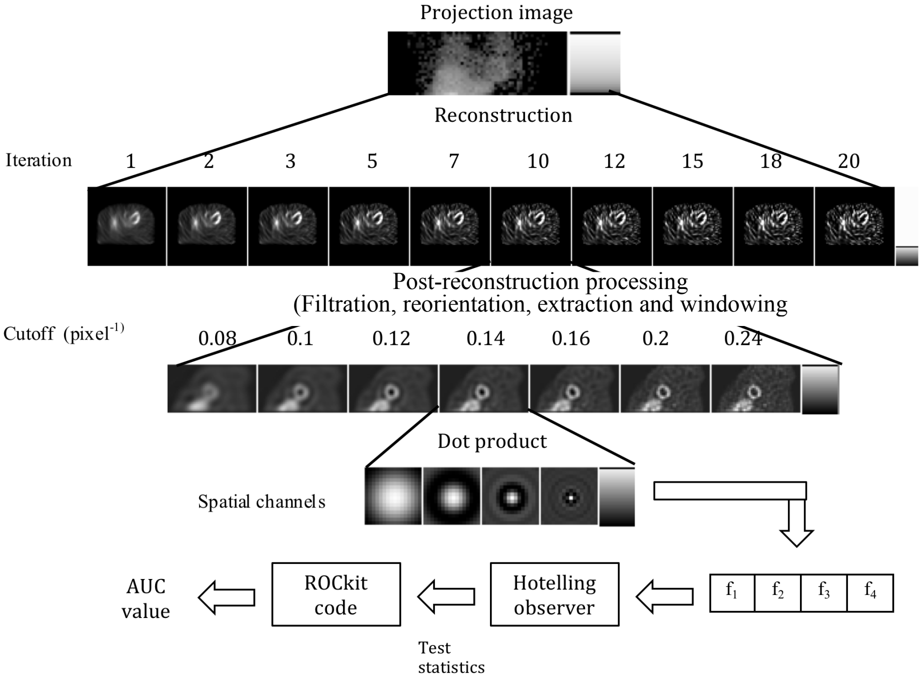

Figure 5-7. Schematic diagram showing the steps involved in the CHO study.

5.3 Results and Discussion

5.3.1 IO and IO-MM studies

Figure 5-8 shows a plot of the AUC values for the different collimators of the IO (i.e., the case where the observer used the full CDR model) and the IO-MM, for the cases where CDR was modeled using the GRF only and no model. Note that the error bars were very small (~0.003). The IO, which included the full CDR, suggested that a collimator with a full-width at half-maximum (FWHM) of 0.9-1.1cm (C_3-C_4) at 10 cm was optimal. Collimators with FWHM of 0.9 cm (C_3) and 0.7 cm (C_2) were optimal when the observer incorporated an approximate model (GRF only) or when it did not include a model for the CDR, respectively. We also noted that IO-MM observer performance degraded more for higher sensitivity/poorer resolution collimators, due to the progressively increased mismatch between the models incorporated in the IO-MM and the true full CDR model.

These results suggest that the closer the model used by the observer to the true model, the higher the observer performance, and the more the optimal collimator shifts toward poorer resolution. This also suggests that it is important to take into account the effects to be modeled in the reconstruction when optimizing the collimator. In other words, these data suggest simultaneously optimization of the reconstruction/compensation methods and instrumentation. We tested the statistical significance of the differences between the AUC value of the IO-ASF, at the optimal collimator (C_4), and the AUC values of the IO-MM-ASG and IO-MM-ASN at the corresponding optimal collimators, C_3 and C_2, respectively. The tests indicated that the differences between the AUC values when using the full and the geometric responses were not statistically significant, at 95% confidence level, with p-value of 0.34. However, the differences between the AUC values when using full and no CDR modeling were statistically significant with a p-value was less than 10^{-10}. ROC curves for the optimal collimators and the three CDR modeling methods are shown in Figure 5-9. These data suggest that, when using a good model of the CDR, poorer resolution/higher sensitivity collimators than the GE-LEHR collimator were optimal for MPS. This agrees with previous results as reported in [77, 82, 84, 111] for different clinical tasks.

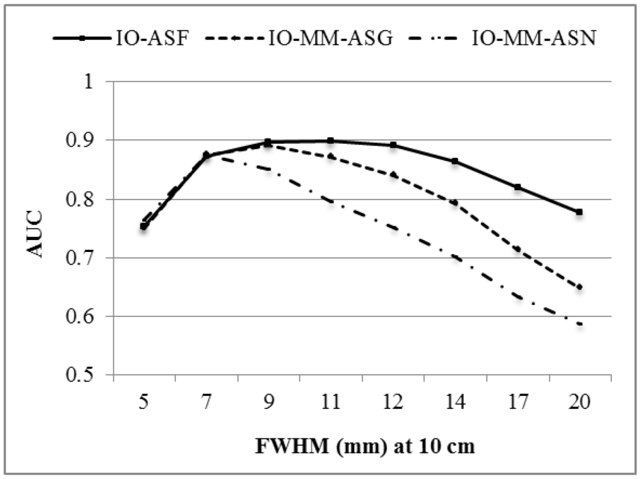

Figure 5-8. Performances of the IO and IO-MM observers as represented by the AUC for the different collimators and CDR modeling methods

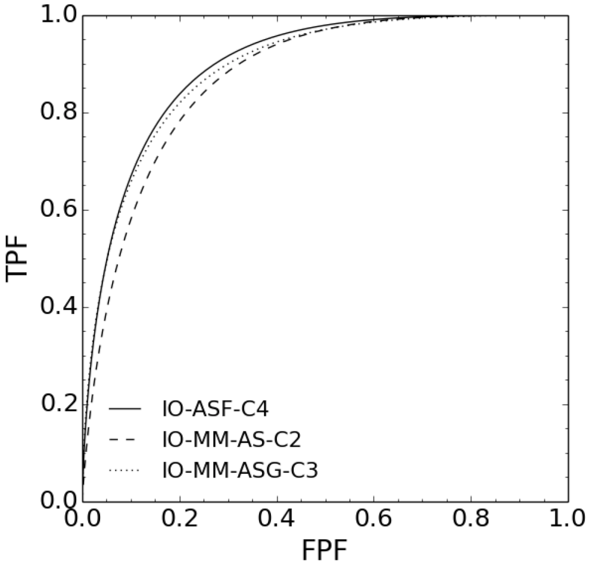

Figure 5-9. ROC curves for the optimal collimators for three different CDR modeling methods.

We analyzed observer performance as a function of defect location (Figure 5-10) and extent and severity (Figure 5-11). The observers performed better on detecting the anterolateral defects than on defects located at the inferior wall of the myocardium. This is likely because of the effect of high uptake in the liver, which reduced the visibility of inferior wall defects due to partial volume effects. The optimal collimators using the various CDR modeling methods did not change for the different locations. Figure 5-11, shows that the observers' performances degraded when the defect severity decreased. We also observed dependence of the optimal collimator on defect size; the optimal collimator shifted toward poorer resolution as the defect size increased.

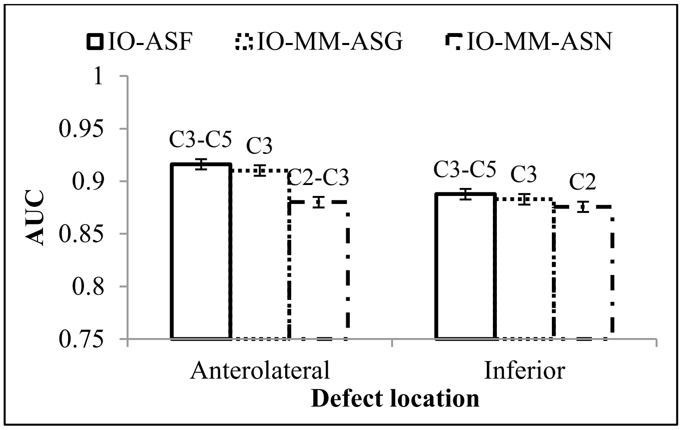

Figure 5-10. Observers' performances for the different defect locations.

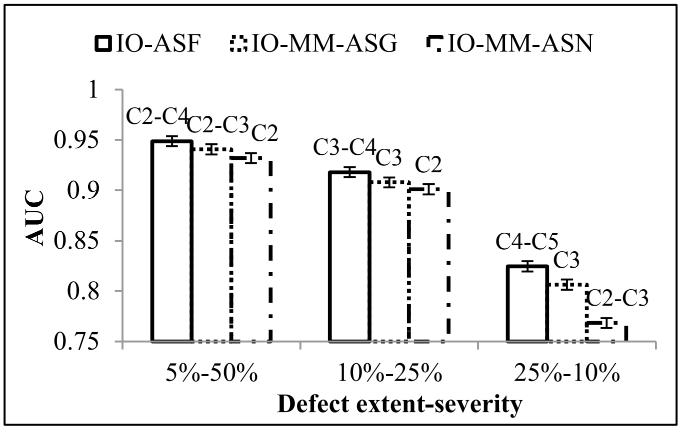

Figure 5-11. Observers' performances for the different defect extent-severity combinations.

5.3.2 CHO study

5.3.2.1 Optimization of reconstruction parameter

Figure 5-12 shows 2D contour plots of the AUC values as a function of the iteration number and the Butterworth post-reconstruction filter cutoff frequency for the different compensation methods. The plots correspond to collimators with FWHM of 1.1 (C_4), 0.9 (C_3) and 0.7 cm (C_2) at 10 cm for compensation methods ASF, ASG and ASN, respectively; as will be shown below, these collimators were optimal for each of these methods. Table 5-2 shows the optimal cutoff frequency and iteration for each collimator and compensation method. Figure 5-13 shows short axis images reconstructed using the different compensation methods and optimal reconstruction parameters. From the data in Table 5-2, more iterations were required for compensation methods that incorporated CDR compensation. The optimal number of iterations also increased for poorer resolution collimators. We observed that there was a relatively large region of near-optimal cutoff frequencies. This may be due to the fact that there was a range of defect sizes and a different cutoff frequency is optimal for each defect size.

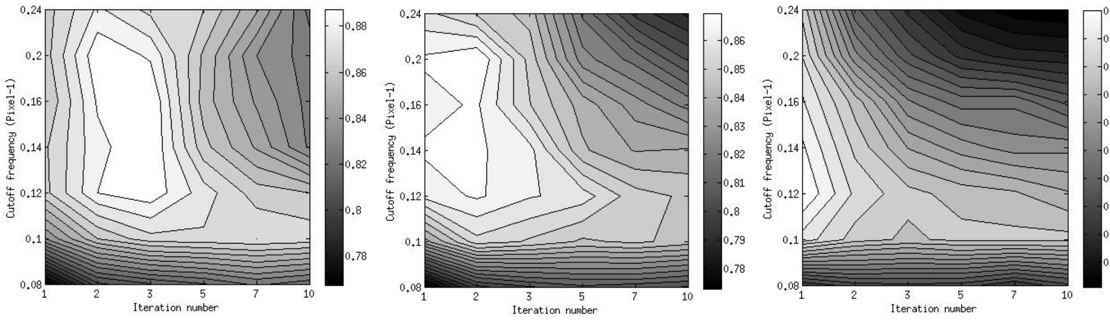

ASF ASG ASN

Figure 5-12. 2D contour plots of the AUC values as a function of the iteration number and the Butterworth filter cutoff frequency for the different compensation methods using the optimal collimators.

Table 5-2. Optimal reconstruction parameters for each compensation method.

Collimator FWHM (cm)	ASF		ASG		ASN	
	Iteration[1]	Cutoff	Iteration	Cutoff	Iteration	Cutoff
5	1	0.1	1	0.1-0.12	1	0.1
7	1-2	0.12-0.24	1	0.12-0.24	1	0.12-0.14
9	2-3	0.12-0.2	1-2	0.12-0.24	1	0.14-0.16
11	3-5	0.24	2-3	0.14-0.24	1	0.14-0.16
12	7	0.2	2-5	0.14-0.24	1	0.14-0.16
14	12	0.24	3-10	0.12-0.24	1-3	0.14-0.2
17	24-30	0.12-0.24	7-22	0.1-0.24	1-2	0.14-0.2
20	24-30	0.1-0.24	10-30	0.08-0.24	1	0.14-0.24

[1] Number of subsets = 12

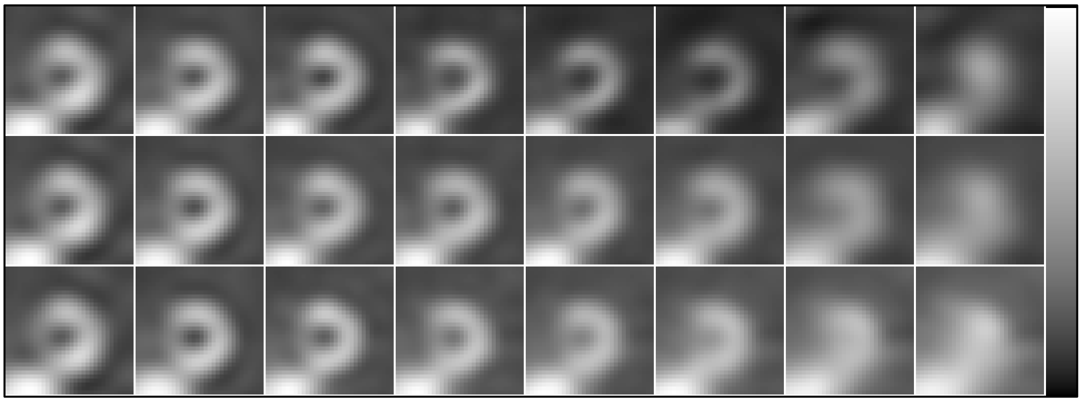

Figure 5-13. Sample short axis images corresponding to the optimal reconstruction parameters for collimators C_1 to C_8 (from left to right) reconstructed using compensation methods ASF (top), ASG (middle) and ASN (bottom).

5.3.2.2 Comparison of compensation methods

A plot of the AUC for the different collimators and compensation methods is shown in Figure 5-14. Again, as was the case with the IO, the error bars were very small (~0.004). CHO performance for the various compensation methods was very similar to the performance of the IO and IO-MM. The optimal collimator when compensating for the full CDR had a FWHM of 0.7-1.1 cm at a distance of 10 cm (C_2-C_4), and the differences between the AUC values of the three collimators were not statistically significant (p-values were less than 10^{-8}). As was observed with the IO and IO-MM, approximating the CDR by the GRF or when no model was used, the optimal collimator shifted toward higher resolution.

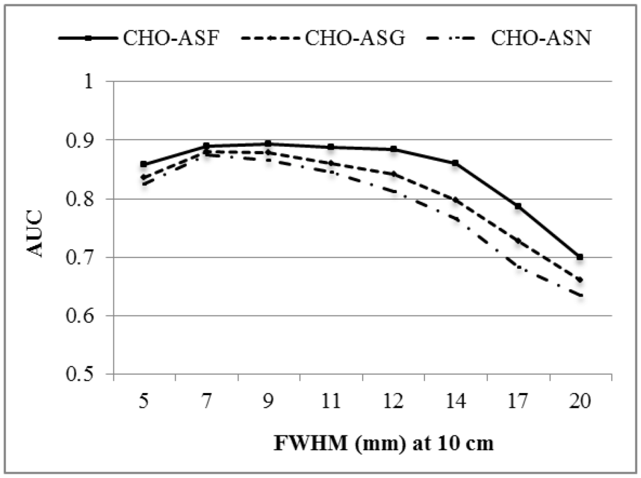

Figure 5-14. Plot of AUC values for the different collimators and CDR compensation methods using optimal reconstruction parameters.

We compared the optimal collimators obtained when using the IO and IO-MM versus the CHO to evaluate the different compensation methods, as shown in Table 5-3. We see that IO and IO-MM well predicted the "just the optimal" rankings of the CHO for the different compensation methods. However, estimating the IO and IO-MM performance on projection images was faster by factors of ~28, 8 and 2 than estimating the CHO operating on reconstructed images using ASF, ASG and ASN compensations, respectively. The results also suggested that compensating for the geometric response component of the CDR yielded similar performance as full CDR compensation, there was little benefit from computationally-expensive full CDR compensation.

Table 5-3. Optimal collimators for the IO, IO-MM and CHO

	ASF		ASG		ASN	
	AUC	Optimal FWHM (cm)	AUC	Optimal FWHM (cm)	AUC	Optimal FWHM (cm)
IO & IO-MM	0.899	0.9-1.1	0.892	0.9	0.875	0.7
CHO	0.893	0.7-1.1	0.881	0.9-1.1	0.875	0.7

5.4 Conclusions

In this work, we applied three different model observers for the optimization of parallel hole collimators and the evaluation of different CDR compensation methods in the context of MPS imaging. The analysis was performed using realistic simulated populations of BKS/SKE data. We first used the IO to select the optimal collimator for a fixed penetration criterion of 0.3%. The optimum collimator had FWHM of 0.9-1.1 cm at 10 cm, which is very similar to the optimal parameters suggested by the CHO when operating on images reconstructed using full CDR or geometric response compensation. However, the optimal parameters were different when compared to those obtained by the CHO when no CDR compensation was used. The IO provides a powerful tool for optimizing instrumentation and acquisition parameters in the projection domain provided that good models (i.e. small mismatch) of the image formation process are incorporated into the reconstruction algorithm.

The IO-MM and CHO had the same rankings of the CDR compensation methods and gave similar optimal collimators for the different compensation methods. For the case when no CDR model was used (i.e. the mismatch effect was bigger), the IO-MM showed better agreement with the CHO in terms of optimal parameters, where the IO did not. This indicates that the IO-MM may be useful as a surrogate for optimizing acquisition and instrumentation in cases where there is significant model mismatch in the reconstruction methods used to generate images for human observer MPS defect detection.

6. Optimization of energy window and evaluation of scatter compensation methods in MPS using the ideal observer with and without model mismatch and an anthropomorphic model observer

6.1 Introduction

Model observers have been widely used to perform task-based assessment of medical image quality. Two important categories of model observers are ideal and anthropomorphic observers. The ideal observer (IO) outperforms all other observers and sets an upper limit on task performance measured by figures of merit such as the area under the receiver operating characteristic (ROC) curve (AUC) [24]. The IO makes optimal use of all the information in the raw data. However, it requires full knowledge of the raw data statistics. Therefore, it is typically applied in the projection domain, where the quantum noise statistics are known and easier to analyze. Moreover, IO performance is not improved by linear operations on the raw data such as linear filtering or (linear) reconstruction algorithms, and it thus allows optimization of instrumentation or reconstruction parameters in the projection domain and provides an alternative to image domain optimization.

Anthropomorphic model observers, such as the channelized Hotelling observer (CHO) using anthropomorphic channels [43], are designed to predict how humans would perform. They have been extensively used in the evaluation and optimization of acquisition, instrumentation, reconstruction and compensation methods in the context of myocardial perfusion, bone, and hepatic SPECT [45-47]. The CHO has shown good agreement with human observers in a variety of clinical applications and tasks [44-52, 112]. For SPECT, the CHO is typically applied to reconstructed images. Since task performance for both humans and the CHO depends on details of compensation and regularization methods and parameters, comparing performance in this domain should be done with images that are optimized in terms of relevant reconstruction and regularization parameters, such as iteration number and the cutoff frequency of any post-reconstruction smoothing filter. This optimization requires significant computational resources, and it is thus simpler and more efficient to optimize imaging systems in the projection domain using the IO rather than in the reconstructed image domain using the CHO.

Despite the potential advantages of using the IO, it has rarely been rigorously applied to real imaging tasks due to the technical difficulty of estimating the performance for realistic background variability arising from variations in patient anatomy and uptake. Its application has been limited to cases where the background and signal models could be expressed analytically, which often do not capture the variability observed in clinical studies [38-40]. To overcome this limitation, methods based on Markov Chain Monte Carlo (MCMC) techniques have been developed and applied to estimate the IO test statistic, i.e., the likelihood ratio (LR), for realistic and general background and signal models for binary defect detection tasks [33, 34, 41].

Another difficulty in evaluating and optimizing imaging systems using the IO is that, since the IO has full knowledge of all the statistical information about the background and signal, it implicitly has a perfect model of the image formation process, including all physical processes and factors that degrade image quality (e.g., finite energy resolution, scatter, attenuation). One way to think about this phenomenon is that the image formation models embedded in the IO match perfectly the models used to form the projection images, $p_t(.)$ (Figure 6-1). In some sense, the IO can be viewed as providing ideal compensation for the various image degrading effects, and the task performance it achieves reflects the best achievable with perfect compensation. However, real reconstruction and compensation algorithms do not perfectly model the image formation process and, in fact, there are often physical effects for which no compensation is provided. The difference between the true model, $p_t(.)$, and that used in reconstruction, $p_m(.)$, is referred to as model mismatch (MM). This mismatch could lead to deviations in performance or performance rankings between the IO operating on projection images and human observers or CHO operating on reconstructed images [103]. In such cases it is not clear that system optimization using the IO would yield the same optimal paramters as optimizing using human or anthropomorphic model observers.

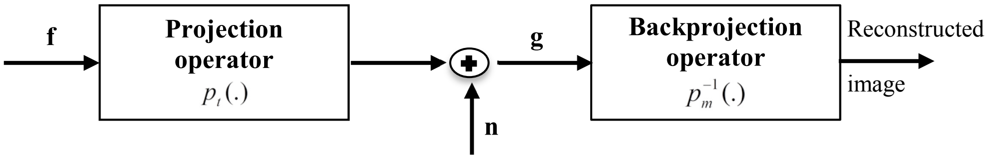

Model Mismatch: MM = $p_t(.) - p_m(.)$

Figure 6-1. A schematic diagram of the image formation process and the definition of model mismatch term

We have previously introduced the concept of including MM into the IO framework [3, 4]. We call this observer the IO with model mismatch (IO-MM). The IO-MM still uses the LR as the test statistic, but in the estimation of the LR it uses an approximate model of the image formation process ($p_m(.)$) instead of the true model ($p_t(.)$). In [4], we compared the performance of the IO and IO-MM with that of the CHO for the task of optimizing the energy window for myocardial perfusion SPECT imaging. The results for the IO-MM showed good agreement with that of the CHO. We have also used the IO and IO-MM to optimize the energy window in ^{90}Y bremsstrahlung SPECT for a detection task [110]. The optimal energy window was narrower when taking into account model-mismatch, and was similar to that obtained previously when optimized for estimation tasks [71].

In MPS imaging using Tc-99m, due to the interactions of the Tc-99m photons in the body and collimator-detector system and the limited energy resolution of scintillation cameras, the recorded energy spectrum is degraded, as shown in Figure 6-2. Detection of scattered photons degrades the final image quality and thus has a significant impact in limiting the diagnostic accuracy of readers interpreting the images. Therefore, it is desirable to reduce the effects of scatter on the final image quality, by either reducing the number of detected scattered photons or compensating for them.

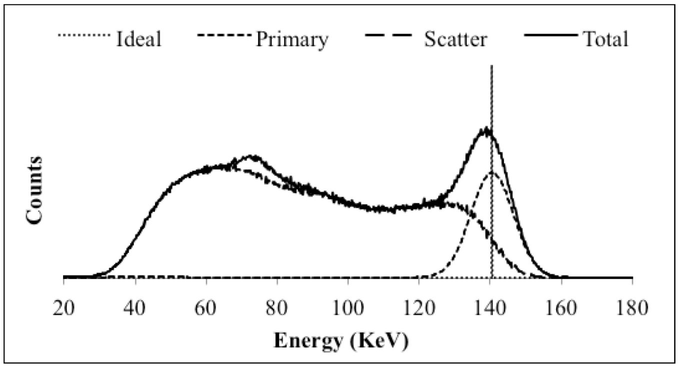

Figure 6-2. Tc-99m spectrum

One way to reduce the number of detected scattered photons is to use narrower acquisition energy windows. However, there is a tradeoff between the width of the acquisition energy window and image noise; reducing the width of the energy window decreases the number of detected primary and scattered photons concurrently. This would result in an increase of the noise in the projection data, which could degrade the performance of human observers operating on the final images. In this work, we seek the optimal acquisition energy window width that provides the best tradeoff between reducing scatter and increasing noise, as measured by performance on a perfusion defect detection task.

Scatter compensation can result in improved quantification, lesion detection, and contrast-to-noise ratios [17, 20, 46, 113, 114]. Current methods for scatter compensation can be divided into two general categories based on how the scatter component is estimated: energy and spatial estimation methods. In the former category, scatter in the photopeak image is estimated using information acquired in one or more additional energy windows [115]. The dual and triple energy window methods are examples of this approach, and have been widely adopted due to their simplicity and effectiveness [116]. In the dual energy window (DEW) method, an appropriately scaled projection image acquired in a relatively narrow energy window immediately below the photopeak window is used as an estimate of the scattered component of the photopeak window. For the triple energy window (TEW) method, images used for scatter estimation are acquired in energy windows below and above the photopeak window. A disadvantage of window-based methods is the noise in the scatter estimate that results from acquiring data in these narrow windows. Increasing the width of the scatter window reduces noise in the scatter estimate, but provides, in general, a more biased estimate of scatter in the photopeak window [117].

The alternative to energy-based scatter estimates is spatial modeling. Scatter modeling methods estimate the scatter component of the projection data based on an estimate derived from the reconstructed image [15, 118]. They can naturally be applied as part of iterative reconstruction algorithms. An example of model-based scatter estimation methods is the Effective Scatter Source Estimation (ESSE) method [118]. It uses a set of scatter kernels that are pre-calculated using Monte Carlo simulation methods to estimate an effective scatter source whose attenuated projection gives the scatter contribution in the projection data. It has previously been applied in a number of SPECT imaging applications for scatter, downscatter, and crosstalk estimation and provided accurate compensation [119, 120].

In this work, we extended the work introduced in [2] to compare different scatter estimation methods, including the DEW, TEW and ESSE methods in the context of MPS, and to find the optimal acquisition energy window width that provides the best performance on a binary defect detection task, using the IO and IO-MM. We also compared the performance of the IO and IO-MM to that of an anthropomorphic observer (CHO) applied to images reconstructed using the Ordered-Subset Expectation-Maximization (OS-EM) algorithm. In addition to providing information about optimal energy windows and scatter copensation strategies for MPS, this study investigates the use of the IO and IO-MM to perform projection-domain optimization of acquisition parameters in comparison to reconstructed image-domain optimization using an anthropmorphic CHO in the presence of varying degrees of model mismatch.

6.2 Methods

In this section, we introduce the key elements of task-based image quality assessment, including the task, object, imaging system models, observer and figure of merits [24]. We revisit the concept of MM and give a brief overview of the IO, the use of MCMC to estimate IO performance, and the modifications needed in the IO to take MM into account. Finally, we give a brief description of the CHO that was used as a surrogate for human observer performance.

6.2.1 Identification of the task

In this work, we focused on the task of detecting a fixed signal in a realistic, randomly varying background in the context of MPS. In a binary classification (detection) task, the observer is asked to classify a given image as either containing or not containing a signal, in this case a myocardial perfusion defect.

6.2.2 Object and imaging system models

It has been previously reported that variability in patients' anatomy and activity uptake are important factors that limit task performance, and it is thus important that the object model be realistic and represent the range of variability seen in clinical populations [31, 47, 66, 81, 89]. To this end, we have previously designed and developed a digital phantom population based on the 3D eXtended CArdiac Torso (XCAT) phantom, and generated the corresponding Tc-99m projection data [1]. The population consists of 54 phantoms including anatomical models for both genders and 3 variations (small, medium and large) in body habitus, subcutaneous adipose tissue thickness, and heart size. The anatomical parameters of the phantom population were obtained from the anatomical distributions in the Emory Cardiac Database (Barclay, Emory University), which includes anatomical measurements from 166 patients. The phantoms were digitized into 0.221 cm cubic voxels. We simulated anterolateral and inferior perfusion defects with a 10%

extent and 25% severity. The extent and severity are the fraction of the left ventricular volume and reduction of uptake in the perfusion defect relative to the normal myocardium, respectively. The extent and severity of the defect were chosen to be challenging and clinically relevant.

Projections of the phantom population were simulated using the SimSET Monte Carlo code [61] and angular response functions [23] to model interactions in the body and the collimator detector system, respectively. We modeled a GE Infinia dual-detector SPECT system with a GE low-energy high-resolution (LEHR) collimator and a 9.5 mm thick NaI(Tl) crystal. Projections were simulated using non-circular phantom-specific body-contouring orbits and acquired at 60 equispaced angles over a 180° acquisition arc extending from 45° right anterior oblique to 45° left posterior oblique. Projection images were binned in a 128x114 matrix with a pixel size of 0.442 cm.

To model uptake variability, we simulated low noise Tc-99m projection data for the heart, liver and body (including all other organs) for each phantom. This enabled us to separately scale the individual projection images of the different organs using random scale factors obtained from distributions that were based on data from a set of 34 patients who underwent MPS. We could then sum the scaled projections before simulating Poisson noise to generate an uptake realization. In this study, we modeled an injected activity of 10 mCi of Tc-99m to model a low-dose protocol.

Optimizing energy windows requires projection images acquired in various acquisition energy windows. The flexible and efficient design of the phantom population and the projection database in [1] permitted us to compute projections in any arbitrary energy window. The original projection data were simulated in 1 keV wide energy bins with no measurement-related energy blurring. We computed projections in different energy windows by summing the data from these narrow bins. The summing process took into account the energy-dependent energy resolution function. We investigated 11 acquisition energy windows, labeled W_1 to W_{11}, with the parameters shown in Table 6-1. Figure 6-3 shows sample low-noise and noisy projection images acquired in the different energy windows. Note the tradeoff between increasing scatter, which reduces the contrast of the myocardium, and reduced noise as the energy window width increases. The goal was to seek the window among those listed below that provides the best task performance.

Table 6-1. Investigated Tc-99*m* energy window settings

	W_1	W_2	W_3	W_4	W_5	W_6	W_7	W_8	W_9	W_{10}	W_{11}
Lower threshold (keV)	140	136	132	130	128	126	124	122	120	112	102
Upper threshold (keV)	141	145	149	151	153	155	157	159	161	169	179
Width (keV)	1	9	17	21	25	29	33	37	41	57	77
Width (%)	0.7	6.4	12.1	15	17.8	20.6	23.5	26.3	29.2	40.6	54.8

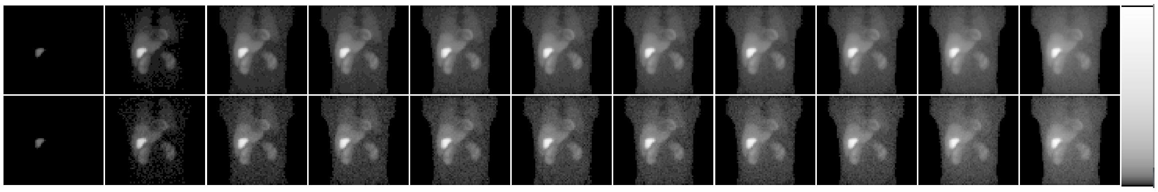

Figure 6-3. Sample low noise (top) and noisy (bottom) Monte Carlo simulated anterior projection images of a medium-sized male phantom with a medium-sized heart and fat level acquired in energy windows W_1 to W_{11} (from left to right). The images are displayed using a logarithmic gray scale to better show the lower uptake organs.

In order to evaluate different scatter estimation, and thus different compensation methods, we generated scatter estimates for the DEW, TEW and ESSE methods. For the DEW method, scatter estimates were generated in a 10 keV wide window below and adjacent to the photopeak window. Scatter estimates for the TEW method were acquired in two 5 keV wide windows immediately below and above the photopeak energy window. For both of the DEW and TEW methods, we calculated the scatter estimates using methods reported in [116]. For ESSE, the projections were calculated directly for the photopeak window using the appropriate scatter kernels. Figure **6-4** shows the true and estimated scatter projections obtained with the various methods.

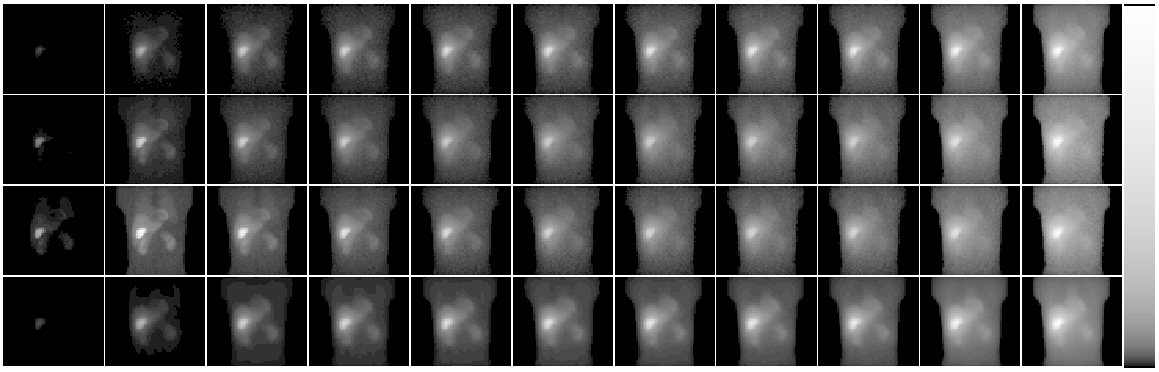

Figure 6-4. Scatter projection images generated using SimSET+ARF (true), DEW, TEW and ESSE methods (from top to bottom) for a medium sized male phantom with medium size heart and fat level acquired from anterior projection view in energy windows W_1 to W_{11} (from left to right). The images are displayed using a logarithmic gray scale to better show the lower uptake organs.

6.2.3 Observers models

6.2.3.1 Application of the Ideal Observer (IO) and the Ideal Observer with Model Mismatch (IO-MM)

In SPECT imaging, given a continuous object, **f**, the projection data, **g**, are the result of the image formation process, and can be represented by:

$$\mathbf{g} = p_t(\mathbf{f}) + \mathbf{n}, \tag{6.1}$$

where $p_t(.)$ is a continuous-to-discrete projection operator that maps the object, **f,** to the projection space and **n** is the measurement noise.

In this work, we consider the task of detecting a fixed signal, $\mathbf{f}_s$, such as a perfusion defect, in a random background, $\mathbf{f}_b$. We define the background and signal projection images as:

$$\mathbf{b}_t = p_t(\mathbf{f}_b), \tag{6.2}$$

$$\mathbf{s}_t = p_t(\mathbf{f}_s). \tag{6.3}$$

For a binary detection task, the two hypotheses to be tested can be written as:

$$H_0: \ \mathbf{g} = \mathbf{b}_t + \mathbf{n},$$

$$H_1: \ \mathbf{g} = \mathbf{b}_t + \mathbf{s}_t + \mathbf{n},$$

where H_0 and H_1 mean signal absent and signal present, respectively.

The IO uses the likelihood ratio, $\Lambda(\mathbf{g})$, of defect-present vs. defect-absent as the test statistic. For the case where the background and signal are known exactly (SKE/BKE) and the only source of randomness is Poisson measurement noise, $\mathbf{n}$, the expression for the likelihood ratio is given by:

$$\Lambda_{\mathrm{BKE}}\left(\mathbf{g},\mathbf{b}_{\mathrm{t}}\right)=\frac{pr(\mathbf{g}\,|\,H_1)}{pr(\mathbf{g}\,|\,H_0)}=\prod_{\mathrm{i}}\left(1+\frac{\mathrm{s}_{\mathrm{t}}\left(\mathrm{i}\right)}{\mathrm{b}_{\mathrm{t}}\left(\mathrm{i}\right)}\right)^{\mathrm{g(i)}}\exp\left(-\mathrm{s}_{\mathrm{t}}\left(\mathrm{i}\right)\right) \tag{6.4}$$

For a signal known exactly embedded in a background known statistically (SKE/BKS), the expression for the likelihood ratio is given by:

$$\Lambda_{\mathrm{BKS}}\left(\mathbf{g}\right)=\int\Lambda_{\mathrm{BKE}}(\mathbf{g},\mathbf{b}_t)\ \mathrm{pr}(\mathbf{b}_t\,|\,\mathbf{g},H_0)\mathrm{d}b \tag{6.5}$$

The idea of (6.5) is to average over the backgrounds sampled randomly from the posterior density $\mathrm{pr}(\mathbf{b}_t\,|\,\mathbf{g},H_0)$. However, the density $\mathrm{pr}(\mathbf{b}_t\,|\,\mathbf{g},H_0)$ is usually not known analytically and is hard to sample from using standard Monte Carlo integration method. Accordingly, methods based on Monte Carlo Markov Chain techniques have been developed to estimate the integral in (6.5) [33, 41].

We applied a previously developed method to efficiently estimate the likelihood ratio [41]. We parameterized the object with a parameter vector, $\vec{\theta}$, which was a combination of discrete anatomical parameters, n, p, q and l that specify the object gender, body size, heart size and fat level, respectively, and continuous organ activity parameters, A_{heart}, A_{liver} and A_{body}, corresponding to the uptake activities of the heart, liver and body, respectively. Thus, the background $\mathbf{b}_t(\vec{\theta})$ parameterized by the vector $\vec{\theta}$ was represented as:

$$\mathbf{b}_t\left(\vec{\theta}\right)=A_{\mathrm{heart}}\ \mathbf{prj}^{\mathrm{heart}}_{n,p,q,l}+A_{liver}\ \mathbf{prj}^{\mathrm{liver}}_{n,p,q,l}+A_{body}\ \mathbf{prj}^{\mathrm{body}}_{n,p,q,l}\ , \tag{6.6}$$

where $\mathbf{prj}^{\mathrm{heart}}$, $\mathbf{prj}^{\mathrm{liver}}$ and $\mathbf{prj}^{\mathrm{body}}$ were the projections of the heart, liver and the body, respectively, filled with unit activity for a given anatomy. The advantage of this approach is that the projections can be precalculated so that the background can be estimated very rapidly simply by scaling and summing the set of 3 projection images.

It has been shown that, if $\mathbf{b}_t\left(\vec{\theta}\right)$ has a one-to-one relation with the parameter vector $\vec{\theta}$, the integral in (6.5) can be expressed as:

$$\Lambda_{\mathrm{BKS}}\left(\mathbf{g}\right)=\int \Lambda_{\mathrm{BKE}}(\mathbf{g},\mathbf{b}_t(\vec{\theta}))\ \mathrm{pr}(\vec{\theta}\,|\,\mathbf{g},H_0)\mathrm{d}\vec{\theta} \tag{6.7}$$

Adopting a Metropolis–Hastings approach to draw samples from the posterior distribution $pr(\vec{\theta}\,|\,\mathbf{g},H_0)$, we could then compute the ergodic average $\widetilde{\Lambda}_{\mathrm{BKS}}\left(\mathbf{g}\right)$, which gives an estimate of the integral in (6.7).

It is relatively straightforward to use this formulation to take into account the "mismatch" between the models used in reconstruction and the real physical image formation process. For the IO-MM and a binary decision task, the two hypotheses to be tested were represented mathematically by:

$$H_0^*:\ \mathbf{g}=\mathbf{b}_m+\mathbf{n},$$

$$H_1^*:\ \mathbf{g}=\mathbf{b}_m+\mathbf{s}_m+\mathbf{n},$$

where **g** was the input projection image generated using (6.1), and the background and signal projection images $\mathbf{b}_m$ and $\mathbf{s}_m$, respectively, were defined as:

$$\mathbf{b}_m=p_m(\mathbf{f}_b), \tag{6.8}$$

$$\mathbf{s}_m=p_m(\mathbf{f}_s). \tag{6.9}$$

For the IO-MM, the expression for the likelihood ratio for the SKE/BKE case is given by:

$$\Lambda_{\mathrm{BKE,m}}\left(\mathbf{g},\mathbf{b}_{\mathrm{m}}\right)=\frac{pr(\mathbf{g}\,|\,H_1^*)}{pr(\mathbf{g}\,|\,H_0^*)}=\prod_{\mathrm{i}}\left(1+\frac{\mathrm{s_m}\left(\mathrm{i}\right)}{\mathrm{b_m}\left(\mathrm{i}\right)}\right)^{\mathrm{g(i)}}\exp\left(-\mathrm{s_m}\left(\mathrm{i}\right)\right). \tag{6.10}$$

When background variability was included, the expression for the likelihood ratio becomes:

$$\Lambda_{\mathrm{BKS,m}}\left(\mathbf{g}\right)=\int \Lambda_{\mathrm{BKE,m}}(\mathbf{g},\mathbf{b}_m)\ \mathrm{pr}(\mathbf{b}_m\,|\,\mathbf{g},H_0)\mathrm{d}b. \tag{6.11}$$

To compute the likelihood ratio for the IO-MM, we followed the same methodology as for the case of the IO. We parameterized the object with the parameter vector, $\vec{\theta}$, applied the MCMC method to sample from the posterior distribution, $pr(\vec{\theta} \mid \mathbf{g}, H_0^*)$, and computed the ergodic average $\widetilde{\Lambda}_{\mathrm{BKS,m}}(\mathbf{g})$. This was implemented using the same computer code as for the IO, by providing a database of organ projections that included the desired model mismatch instead of the true projections.

In the standard IO, we tested the hypothesis that a projection image, **g,** contains or does not contain a fixed defect in a random background, where both the signal and the background images were generated using the true model of the image formation process. Thus, the IO had a perfectly matched model of all physical image-degrading processes. For the IO-MM, we still tested the same hypothesis. However, the signal and the background images provided to the observer were generated using an approximate model $p_m(.)$ of the image formation process. In both cases the input projection data was generated using the true model.

For each energy window, we computed the IO and IO-MM (in the cases where the observer had an approximate model of scatter based on the ESSE, DEW and TEW methods) test statistic using the MCMC method for an ensemble of 2,160 pairs of defect-present and defect-absent projection images modeling different anatomical and uptake variations. The projection data contained a 64x24x60 pixel region of interest centered over the centroid of the heart. This ensured that the whole heart was included inside the region-of-interest. For each energy window, the IO test statistics were used as the input to the ROCkit code [99], which fits a binormal ROC curve to the input set of LRs, to estimate the AUC.

6.2.3.2 Channelized Hotelling Observer study

We used an anthropomorphic CHO as a surrogate for human observer performance, and compared optimal energy window settings and the different scatter compensation methods to those obtained from the IO and the IO-MM.

6.2.3.2.1 Image reconstruction

We performed CHO studies on images reconstructed using the Ordered-Subsets Expectation-Maximization (OS-EM) algorithm with four combinations of compensations: attenuation only (A), attenuation, spatially varying geometric response and scatter using the ESSE scatter modeling (AG-ESSE), attenuation, spatially varying geometric response and scatter using the DEW method (AG-DEW) and attenuation, spatially varying geometric response and scatter using the TEW method (AG-TEW). Figure 6-5 shows sample transaxial slices from images reconstructed using the different compensation methods. For each energy window and compensation method, we used 10 pairs of projection datasets per defect position per phantom, leading to a total of 1,080 pairs of defect-present and -absent images. We used twelve subsets with five projections per subset in the OS-EM algorithm. We considered iterations 1, 2, 3, 5, 7, 10, 12, 15, 18 and 20 in choosing the optimal one.

6.2.3.2.2 Post-reconstruction processing

After reconstruction, images from each of the iterations identified above were filtered using a low pass Butterworth filter with order 8 and cutoff frequencies of 0.08, 0.1, 0.12, 0.14, 0.16, 0.2 and 0.24 pixels^{-1}. We reoriented the filtered transaxial images to the short axis view. For each filtered and reoriented image, we extracted the short axis slice containing the center of the defect (or the same slice in the defect-absent short axis image). Following the methodologies adopted in [46, 54], the pixel values in the filtered, reoriented images were windowed to 256 gray levels by scaling the image so the maximum value in the heart was 255, and negative values were set to zero.

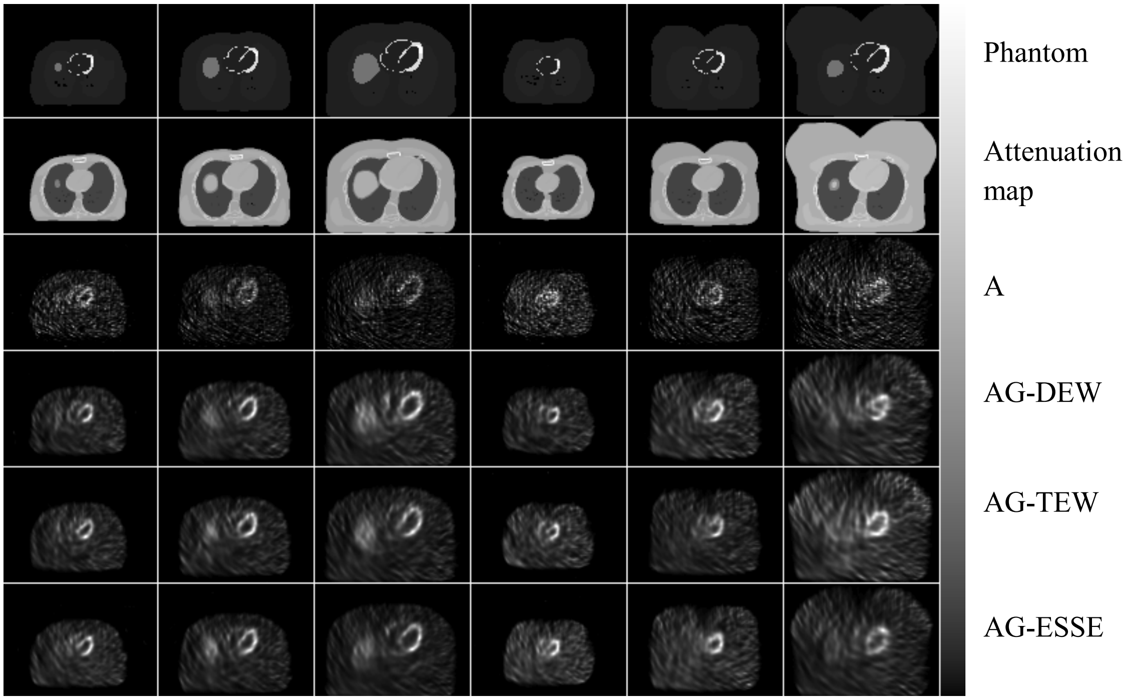

Figure 6-5. Sample transaxial images located at the heart centroid for different phantoms and the corresponding attenuation maps (rows 1 and 2). Rows 3 to 6 show the reconstructed slices obtained using A, AG-DEW, AG-TEW and AG-ESSE compensation methods after the third iteration with 12 subsets per iteration.

6.2.3.2.3 Application of the Channelized Hotelling Observer

In this study, we used four non-overlapping difference-of-mesa frequency channels with successively doubling widths and a starting frequency of 0.5 pixels^{-1}. We estimated CHO performance using a leave-one-out technique in which the CHO was trained using all but one image and tested using the left-out image, producing one test statistic value. This process was repeated with each of the feature vectors being left out, resulting in a set of test statistics with as many members as images. These test statistics were used as inputs to the ROCkit code to estimate the AUC. For each energy window and compensation method, the iteration and cutoff frequency giving the highest AUC were selected as optimal. A schematic diagram showing the steps of the CHO study was shown in Chapter 5, Figure 5-7.

6.3 Results

6.3.1 IO and IO-MM studies

Figure 6-6 shows a plot of the AUC values of the IO, i.e., the case where the observer used a perfect scatter model for the detection task, as a function of acquisition window width. The standard deviations, estimated by ROCkit, were very small (~0.003) and thus were not plotted. The performance of the IO operating on the images acquired in energy window, W_1, a 1 keV wide energy window, was poor. This was a case where quantum noise was dominant, due to fewer detected photons, and significantly limited the observer performance. We observed that the IO performance in the range of energy window widths 9 to 41 keV (W_2 to W_9) did not change substantially, indicating that the observer could handle moderate amounts of scatter. Despite the fact that the IO had a perfect scatter model, the performance was slightly worse for energy windows of widths more than 41 keV (W_{10} and W_{11}). This is likely because the amount of scatter was very high and resulted from very large angle and multiple scatter, thus adding little information relevant to the task. These results suggest that there is no benefit to increasing the acquisition energy window width to more than ~41 keV (W_9), even when incorporating a perfect scatter model.

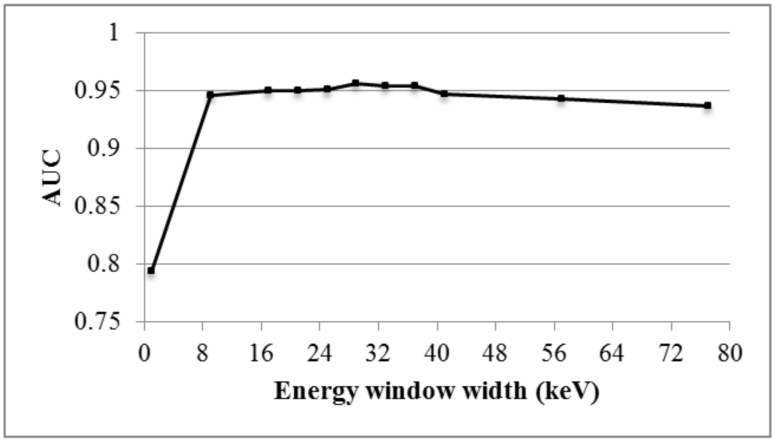

Figure 6-6. The IO performance measured in terms of the AUC value for the different acquisition energy windows.

AUC values of the IO and IO-MM for the cases when scatter was modeled using the ESSE, DEW and TEW methods are shown in Table 6-2. The standard deviations of the AUC values for all methods were, again, very small (~0.004). We note that the maximum AUC value for the IO and IO-MM for the different cases was for an energy window width of 29 keV (W_6). For each scatter modeling method (perfect, ESSE, DEW and TEW), we tested the statistical significance of the difference between the AUC value for a width of 29 keV (W_6) and the rest of the energy windows under investigation. The corresponding *p*-values are shown in Table 6-3. The gray-shaded cells indicate cases where the differences were not statistically significant at the p=0.05 level. The results in Table 6-2 and Table 6-3 indicated that, for the IO, acquisition energy windows of widths between 17 keV (W_3) and 41 keV (W_9) were near-optimal in the sense that we could not reject the hypothesis that the AUC values were less than that for the 29 keV wide window. When the IO-MM incorporated a scatter model based on the DEW, TEW and ESSE methods, the near-optimal range of energy window widths was between 21 and 33 keV (W_4-W_7), 25 and 33 keV (W_5-W_7), 25 and 37 keV (W_5-W_8), respectively.

Table 6-2. AUC values for the IO and IO-MM

Energy window width	IO *(Perfect)*	IO-MM *DEW*	IO-MM *TEW*	IO-MM *ESSE*
1	0.794	0.792	0.723	0.789
9	0.946	0.943	0.855	0.941
17	0.949	0.949	0.938	0.946
21	0.949	0.949	0.954	0.948
25	0.951	0.948	0.957	0.949
29	0.956	0.955	0.960	0.958
33	0.954	0.951	0.959	0.958
37	0.954	0.947	0.954	0.956
41	0.947	0.948	0.950	0.953
57	0.949	0.928	0.931	0.940
77	0.937	0.926	0.924	0.935

Table 6-3. p-values for hypothesis that the AUC for the indicated energy window was different than that for the 29 keV width energy window (W6).

Energy window width	IO (Perfect)		IO-MM (DEW)		IO-MM (TEW)		IO-MM (ESSE)	
	ΔAUC	p-value	ΔAUC	p-value	ΔAUC	p-value	ΔAUC	p-value
1	0.162	0	0.163	0	0.237	0	0.169	0
9	0.010	0.004	0.012	0	0.105	0	0.017	0.023
17	0.006	0.062	0.006	0.012	0.022	0	0.012	0.048
21	0.006	0.633	0.006	0.472	0.006	0.014	0.010	0.013
25	0.004	0.065	0.007	0.095	0.003	0.661	0.009	0.07
29	0	1	0	1	0	1	0	1
33	0.002	0.243	0.004	0.063	0.001	0.371	0	0.572
37	0.002	0.278	0.008	0.002	0.006	0.012	0.002	0.578
41	0.009	0.479	0.007	0.006	0.010	0	0.005	0.026
57	0.013	0.022	0.027	0	0.029	0	0.018	0
77	0.019	0.001	0.029	0	0.036	0	0.023	0

Note: *p*-values less than 10^{-5} are shown as 0

We compared the performance of the IO and IO-MM when incorporating each of the different scatter models for each energy window. Table 6-4 shows the *p*-values for the hypothesis that the AUCs were the same for the various energy windows. We see that the IO-MM that used the ESSE scatter model was statistically indistinguishable (had a *p*-value > 0.05) from the IO, which implicitly had a perfect scatter model, for all the energy windows. This indicates that the information about the scatter provided by ESSE was very similar to that in the true scatter in terms of its effect on defect detection. The performances of the IO-MMs that used the DEW and TEW scatter models were statistically indistinguishable from that of the IO for energy windows W_6 to W_9 and W_4 to W_9, respectively. However, the performance was significantly worse than the IO for energy window of widths more than 41 keV (W_{10} and W_{11}). These data suggest that using an accurate scatter estimate, such as that from ESSE, would allow for the use of a wider energy window without degrading task performance. The DEW or TEW estimates resulted in performance similar to that achieved by the IO when the appropriate acquisition energy windows were used.

Table 6-4. Statistical significance of the differences between the AUC values of the IO and IO-MM for each scatter model.

Energy window width	Perfect Vs. DEW		Perfect Vs. TEW		Perfect Vs. ESSE	
	ΔAUC	p-value	ΔAUC	p-value	ΔAUC	p-value
1	0.002	0.002	0.071	0	0.005	0.457
9	0.003	0.007	0.090	0	0.004	0.185
17	0	0.001	0.012	0.020	0.003	0.327
21	0.001	0.001	-0.007	0.113	0.001	0.531
25	0.003	0.004	-0.006	0.068	0.002	0.258
29	0	0.785	-0.005	0.063	-0.002	0.268
33	0.002	0.618	-0.005	0.066	-0.004	0.341
37	0.005	0.313	-0.001	0.073	-0.002	0.108
41	-0.001	0.392	-0.003	0.388	-0.006	0.819
57	0.005	0.008	0.001	0.001	0.003	0.532
77	0.011	0	0.003	0.006	0.002	0.099

Note: *p*-values less than 10^{-5} are shown as 0

6.3.2 CHO study

6.3.2.1 Optimization of reconstruction parameters

Figure 6-7 shows 2D contour plots of the AUC values as a function of the iteration number and the Butterworth post-reconstruction filter cutoff frequency for the different scatter compensation methods. The plots correspond to energy window widths of 21 keV (W_4), 25 keV (W_5), 25 keV (W_5) and 33 keV (W_7) for the scatter compensation methods A, AG-DEW, AG-TEW and AG-ESSE, respectively. We also observed similar trends for the rest of the energy windows and compensation methods. Table 6-5 shows the optimal cutoff frequency and iteration number for each energy window and compensation method. Figure 6-8 shows short axis images reconstructed using the different compensation methods and optimal reconstruction parameters.

For all methods and energy windows, we observed that the CHO performance was best for 2-3 iterations. Beyond that number of iterations, the AUC values changed slowly with iteration number. The optimal cutoff frequency was between 0.12 and 0.16 pixels^{-1}. This was very similar to what was reported in previous studies [46, 47].

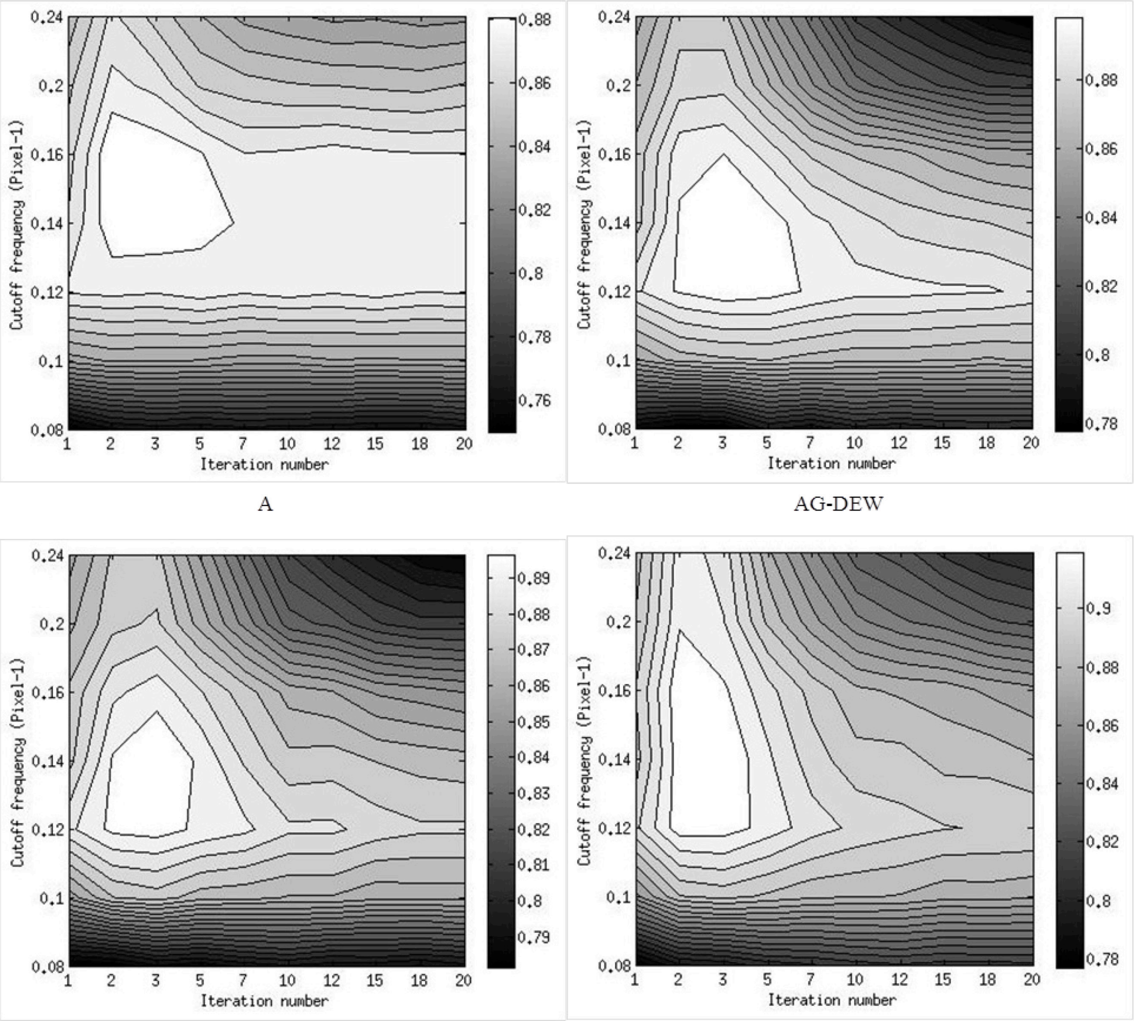

A

AG-DEW

AG-TEW

AG-ESSE

Figure 6-7. 2D contour plots of the AUC values as a function of the iteration number and the Butterworth filter cutoff frequency for the different compensation methods. In the above, A indicates attenuation alone and AG-X indicates attenuation and geometric detector response and scatter compensation using the scatter estimated with method X, where X is either DEW, TEW, or ESSE.

Table 6-5. Optimal reconstruction parameters for each compensation method

Energy window width	A		AG-DEW		AG-TEW		AG-ESSE	
	Iteration[1]	Cutoff	Iteration	Cutoff	Iteration	Cutoff	Iteration	Cutoff
1	1	0.1-0.12	1-3	0.1-0.12	2-7	0.08-0.1	1-5	0.1-0.12
9	1-2	0.12-0.16	2-3	0.12-0.14	3-7	0.1-0.12	2-3	0.12-0.14
17	2-5	0.14	2-5	0.12-0.14	2-5	0.12	2-3	0.12-0.14
21	2-5	0.14-0.16	2-5	0.12-0.16	2-5	0.12	2-3	0.12-0.14
25	2-5	0.14-0.16	2-5	0.12-0.14	2-3	0.12-0.14	2-3	0.12-0.16
29	2-5	0.14-0.16	2-5	0.12-0.14	2-5	0.12-0.14	2-3	0.12-0.16
33	2-3	0.14-0.16	3-5	0.12-0.14	2-5	0.12-0.14	2-3	0.12-0.16
37	2-3	0.14-0.16	2-5	0.12-0.14	2-5	0.12-0.14	2-3	0.12-0.16
41	2-5	0.14-0.16	2-5	0.12-0.14	2-5	0.12-0.14	2-3	0.12-0.16
57	2-7	0.14-0.16	1-5	0.12-0.14	1-7	0.12	2-3	0.12-0.16
77	2-7	0.14-0.16	1-3	0.12	1-5	0.12	2-3	0.12-0.16

[1] Number of subsets = 12

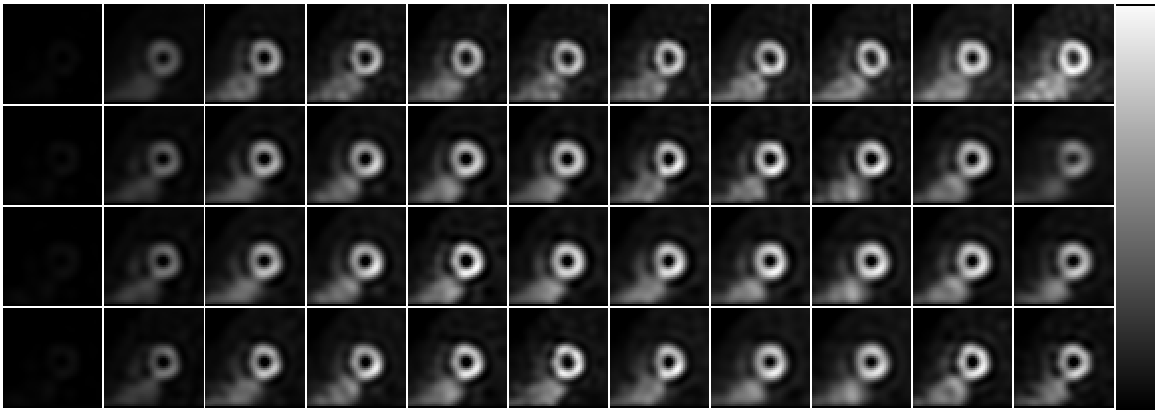

Figure 6-8. Sample short axis image corresponding to the optimal reconstruction parameters for energy windows W_1 to W_{11} (from left to right) reconstructed using compensation methods A, AG-DEW, AG-TEW and AG-ESSE (from top to bottom).

6.3.2.2 Comparison of compensation methods

A plot of the AUC as a function of energy window width for the different compensation methods is shown in Figure **6-9**. Again, as was the case with the IO, the standard deviations were very small (~0.004) and so error bars are not plotted. From these data, we see that scatter compensation using AG-DEW, AG-TEW or AG-ESSE provided better performance than when only attenuation compensation was included. This agreed with previous studies as reported in [46, 47]. These results also indicate that ESSE scatter modeling provided better observer performance than the DEW and TEW methods. This agreed with results of previous human observer studies [121]. The observer performance, when using ESSE scatter compensation, was less sensitive to the changes in the energy window width. This agreed with the results from the IO-MM when using the ESSE scatter model.

For each compensation method, we tested the statistical significance of the differences between the AUC value of the window that had the highest AUC value and that of the rest of energy windows. We computed the *p*-values, given in Table 6, for the hypothesis that the AUC values were different. Gray shaded cells indicate that the differences were not statistically significant at the level p=0.05. Acquisition energy window widths of 17-25 keV (W_3-W_5) were near-optimal for attenuation compensation alone. However, when scatter compensation was incorporated into the reconstruction algorithm, the optimal energy window width was larger than for attenuation compensation only. Thus, scatter compensation enabled the use of wider energy windows. We also observed that the range of the near-optimal energy window widths changed with the compensation method. These data suggest that acquisition energy windows of widths 21-29 keV (W_4-W_6), 25-33 keV (W_5-W_7) and 29-37 (W_6-W_8) keV were near optimal for the AG-DEW, AG-TEW and AG-ESSE compensation methods, respectively.

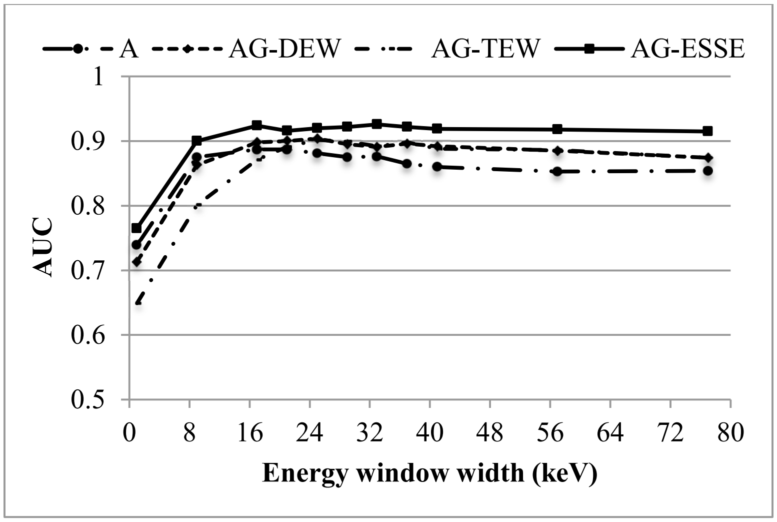

Figure 6-9. Plot of AUC values for the CHO for the different energy windows and scatter compensation methods using optimal reconstruction parameters.

Table 6-6. Results of testing hypothesis that the highest window is optimal for various compensation methods using the CHO.

Energy window width	A	AG-DEW	AG-TEW	AG-ESSE
1	0	0	0	0
9	0.023	0	0	0
17	**1**	0.03	0	0
21	0.239	0.427	0.036	0
25	0.367	**1**	**1**	0
29	0	0.099	0.567	0.635
33	0	0	0.196	**1**
37	0.012	0	0.008	0.071
41	0	0	0.031	0.048
57	0	0	0	0
77	0	0	0	0

Note: (1) In each column the *p*-values are for the difference with respect to the window with the highest AUC, indicated by the cell in dark gray.

(2) *p*-values less than 10^{-5} are shown as 0.

6.3.2.3 Comparison between IO-MM and CHO

We compared the near-optimal energy window settings and the ranking of the different compensation methods obtained when using the IO-MM and the CHO, as shown in Figure 6-10. We see that the IO-MM had similar performance with the three scatter estimation methods for energy windows in the near-optimal range. However, the CHO favored the ESSE method over the DEW and TEW methods and had similar performance when using the DEW and TEW methods. The range of near-optimal energy windows was larger for the IO-MM than the CHO when using the DEW or ESSE scatter models.

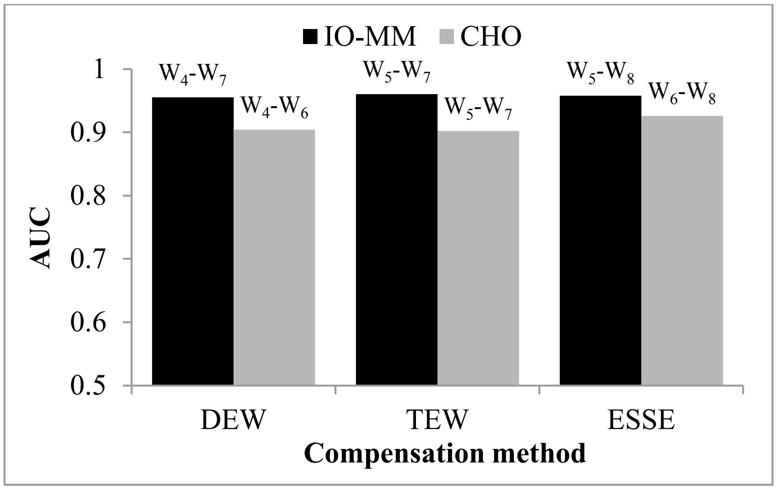

Figure 6-10. Comparison of the IO-MM and CHO performances for the different compensation methods

6.4 Discussion

In addition to the optimal energy windows and rankings of compensation methods, this Chapter provides information on the use of projection domain observers, the IO and IO-MM, as an alternative to optimizing energy windows in the reconstructed image domain using an anthropomorphic model observer. In the case of MPS, the diagnosis is made by human observers interpreting reconstructed images. Clearly, it is desirable that images be optimized in this domain. However, optimizing reconstructed images is computationally intensive due to the computational cost of image reconstruction and the need to optimize regularization parameters. Thus, projection-domain optimization using the IO or IO-MM would be a significant benefit.

The data in this Chapter indicate that projection domain optimization using the IO can give suboptimal parameter values when model mismatch is present. The IO suggested a broad optimal range of energy window widths between 17 keV and 41 keV, with the maximum AUC obtained at a width of 29 keV. On the other hand, the CHO indicated that the optimal energy window width depended on whether scatter was modeled in the reconstruction and on the scatter model used. For example, when scatter compensation was not used (i.e. attenuation only); the optimal energy window width suggested by the CHO was 17 keV. In addition, when scatter compensation was included the difference between the optimal window for the IO and CHO was smaller. This was particularly true for ESSE, the scatter estimation method with the most accurate scatter estimates and thus the least model mismatch. The IO-MM was partially effective in accounting for model mismatch during the optimization: the ranges of the optimal energy window widths for the various scatter modeling methods were narrower than with the IO and very similar to those obtained using the CHO, but the IO-MM and CHO did not predict the same rankings of the scatter estimation methods.

6.5 Conclusions

In this work, we applied three different model observers for the optimization of Tc-99m acquisition energy window width and the evaluation of different scatter estimation methods in the context of myocardial perfusion SPECT defect detection. Performance was evaluated in terms of the area under the ROC curve. The near-optimal range of energy window widths was broader for the IO than for the other observers. This is because the IO, which has the highest performance of any observer, implicitly has perfect knowledge of the image formation process and all physical image-degrading factors. The IO-MM is an observer that allows the incorporation of non-ideal forward models in the optimization process and evaluates them in terms of the IO performance. We used this ability of the IO-MM to compare the DEW, TEW and ESSE scatter estimation methods. The IO-MM had poorer performance than the IO, as expected. The results showed that the ESSE scatter estimation method provided very similar performance to the perfect scatter model implicit in the IO. We also applied the CHO, an established surrogate for a human observer, and compared the optimal energy window settings and the ranking performance of the different scatter compensation methods to those obtained from the IO and the IO-MM. The IO-MM showed good agreement with the CHO for myocardial perfusion SPECT (MPS) energy window optimization and the evaluation of scatter modeling methods. The results of this study also demonstrated that the disagreement between the optimal energy window between the IO and the CHO was smallest when the model mismatch was smallest. This suggests that the IO may be appropriate for projection domain optimization in cases where the model of the image formation process used in image reconstruction is a good representative of the true image formation process.

7. Optimization and evaluation of dual isotope imaging protocols in MPS

7.1 Introduction

Myocardial Perfusion SPECT (MPS) is a well-established noninvasive method for the detection and characterization of coronary artery disease (CAD). Most myocardial perfusion protocols involve the use of Tl-201 and/or Tc-99m labeled compounds. Single-isotope imaging protocols for tracers using both of these radionuclides as well as dual-isotope protocols with separate acquisition of stress and rest images are well established in routine clinical cardiac imaging [10]. Dual-isotope simultaneous-acquisition (DISA) stress Tc-99m/rest Tl-201 is an appealing cardiac SPECT protocol that allows for simultaneous evaluation and characterization of the stress and rest states of myocardial perfusion [122-124]. In addition to providing perfect registration of the rest and stress images in space and time, DISA techniques promise to provide reduced acquisition time, improved patient comfort, and better clinical throughput than single or dual isotope techniques using separate acquisitions (Figure 7-1). In MPS, the stress and rest images are used to classify the patient as being normal (where there is no defect in either image), having a fixed perfusion defect (where there is a defect in both the rest and stress images) or having a reversible defect (where there is a defect in the stress image but not the rest).

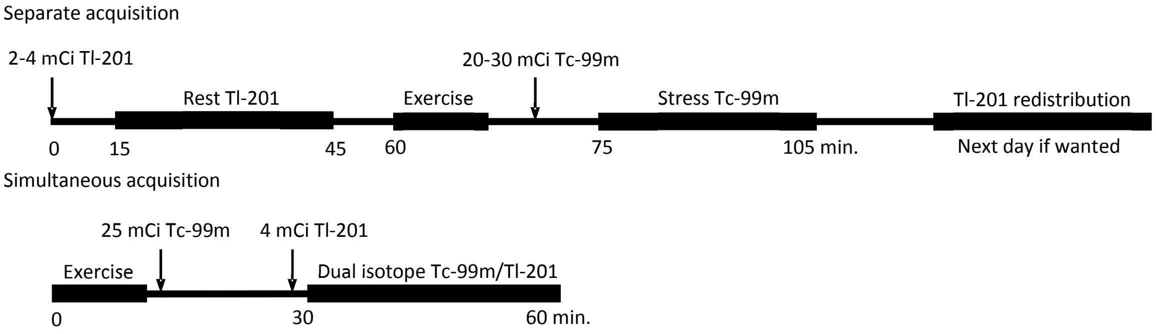

Figure 7-1. Sample protocols for separate and simultaneous acquisition Tl-201/Tc-99m dual-isotope imaging.

A major image-degrading factor in DISA SPECT is crosstalk, where photons from one radionuclide are detected in the photopeak energy window of the other radionuclide [125, 126]. Crosstalk results from a number of physical processes, including Compton scatter in the patient, collimator, or crystal or Pb x-ray production in the collimator or simply the inclusion of the 135 keV Tl-201 photopeak in the Tc-99m energy window. There is substantial crosstalk from Tc-99m into the Tl-201 photopeak window, but the contribution of Tl-201 to the Tc-99m energy window is negligible (~2.9%). This is demonstrated by the sample Tc-99m and Tl-201 energy spectra shown in Figure 7-2.The spectra in Figure 7-2 correspond to injected activities of 30 mCi and 3 mCi of Tc-99m and Tl-201, respectively. This crosstalk results in a reduction in image quality that limits both quantitative accuracy and the ability to detect abnormalities and classify patients based on the simultaneously acquired images [126, 127].

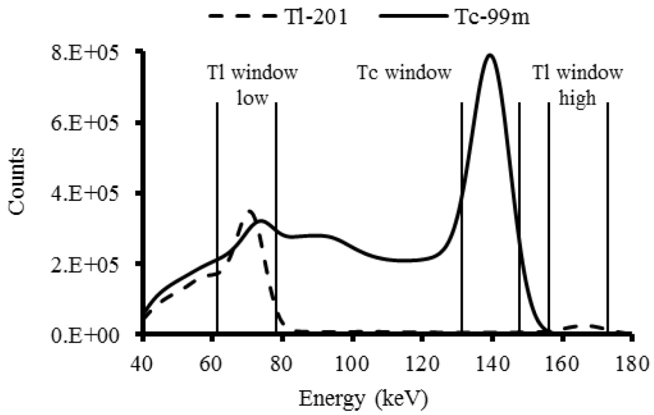

Figure 7-2. Sample energy spectrum indicating detected Tc-99m photons, Tl-201 photons.

Techniques for compensating for crosstalk include estimating and subtracting it prior to reconstruction or reconstruction-based compensation. This can be done either in the spatial domain using crosstalk models [120, 128-132] or using measurements in multiple energy windows [133-135]. However, even with an ideal crosstalk estimation method, it is impossible to remove the statistical noise that crosstalk photons contribute and limit image quality. One approach to further improve image quality is to reduce the amount of crosstalk by optimizing the acquisition parameters, such as the relative injected activity, defined as the ratio of Tc-99m to Tl-201 injected activities, and the acquisition energy windows. However, there are a number of tradeoffs involved, as will be discussed in more detail below. It is thus essential to balance these effects in terms of the performance on the task that will be performed with the images. For MPS, the relevant task is the 3-class classification task described above.

The task-based optimization of DISA acquisition parameters requires taking into account the 3-class nature of the diagnostic task because there is an inverse relationship between image qualities for the rest and stress images. For example, if the Tl-201 injected activity is fixed, then decreasing the Tc-99m injected activity decreases the crosstalk contamination of the rest image, and thus improves the rest image quality at the expense of noisier stress images; similarly, increasing the Tc-99m injected activity improves the stress image quality at the cost of more crosstalk contamination in the rest images.

He et al. [136-139] derived a 3-class ROC analysis method that extends and unifies the decision theory, linear discriminant analysis, and psychophysical foundations of binary ROC analysis in a 3-class paradigm assuming an equal error utility (EEU), i.e., the utilities of making the two possible incorrect decisions are the same for a given class. The decision variable that maximizes the expected utility under the EEU assumption was the log-likelihood ratio; the corresponding decision structure was as shown in Figure 7-3. This is thus the 3-class Ideal Observer (IO).

Task performance is characterized by the 3-class ROC surface, obtained by sweeping the decision structure across the log-likelihood decision plane and calculating the triplet (T1F, T2F and T3F), defined as the true class fractions, for every position of the critical point, i.e., the intersection of the 3 rays in the decision structure. The volume under the 3-class ROC surface (VUS) was proposed as a figure-of-merit (FOM) for task performance. This method was used to investigate the optimal relative injected activity of Tc-99m with respect to this 3-class diagnostic task. The optimization was performed using reconstructed images and a Channelized Hotelling Observer (CHO) [140]. This optimization is very computationally intensive, as it requires simulation of full SPECT data, reconstruction of many noise realizations of projection data, and optimization of the number of iterations and post-reconstruction cutoff filter.

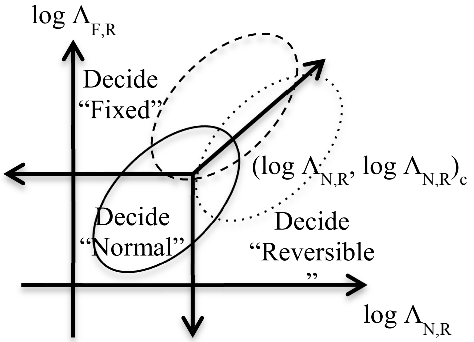

Figure 7-3. Log likelihood ratio decision plane and the decision structure for the practical 3-class ROC analysis method.

Another protocol parameter that can be varied to optimize the quality of DISA images is the energy window used to acquire projection data for each isotope. Wang et al [141] studied the optimal energy windows for Tc-99m/Tl-201 DISA using a signal known exactly (SKE), background know exactly (BKE) task combined with a somewhat ad hoc observer, the no-low-frequency ideal observer. They reported that the optimal energy windows for simultaneous and separate acquisition protocols were different.

In this work, we implemented rigorous and practical projection-domain-based optimization methods for performing the requisite 3-class optimization using the ideal observer operating on realistic data generated from a population of phantoms. We have also compared the performance for the dual isotope simultaneous and separate acquisition protocols.

7.2 Methods

7.2.1 Phantom population and projection data

We have previously developed a realistic digital phantom population for myocardial perfusion SPECT imaging research [1]. In this section, we give a brief overview of the population and the generation of the corresponding Tc-99m and Tl-1201 projections. The population is based on the 3D XCAT phantom with organ size parameters sampled from the Emory PET Torso Model Database [96]. The population consists of 54 phantoms and includes variations in gender, body size, heart size and subcutaneous adipose tissue thickness. Anterolateral and inferior perfusion defects are available for each phantom; in this work we used a defect with 10% extent and 25% severity.

Projections of the XCAT phantoms were simulated using the SimSET Monte Carlo code and angular response functions to model interactions in the body and the collimator detector system (including Pb x-rays, septal penetration and scatter), respectively [23, 61]. For each phantom, low noise Tc-99m and Tl-201 projection data for the heart, liver and body (including all other organs) are available, to allow modeling of organ uptake variability by post-simulation scaling and summing of the individual sets of projections followed by simulating Poisson noise. Organ uptakes are based on data from a set of 34 patients who underwent sequential-acquisition dual isotope MPS. In the clinical data, patients were injected with 30 mCi of Tc-99m and 3 mCi of Tl-201, corresponding to total effective dose of 25 mSv [142, 143]. The durations at each view for the clinical acquisitions were 26 and 30 seconds for the Tc-99m and Tl-201 acquisitions, respectively, at a total of 60 projection views. Projection images were simulated at 60 equispaced angles over a 180° acquisition arc extending from 45° right anterior oblique (RAO) to 45° left posterior oblique (LPO) binned in a 128x114 matrix with a pixel size of 0.442 cm. We simulated a patient specific non-circular body-contouring orbit. We modeled a GE low-energy high-resolution (LEHR) collimator and a 9.5 mm thick Sodium Iodide (NaI) crystal with a 9% energy resolution at 140 keV and $E^{-1/2}$ energy dependence.

Optimizing relative injected activity and the width of acquisition energy window requires projection data generated in various energy windows and injected activities for both Tc-99m and Tl-201. The flexible design of the projection database in [1] allowed us to rapidly generate projections for various combinations of Tc-99m and Tl-201 injected activities and acquisition windows. To study the effect of the relative injected activity, we varied Tl-201 activity from 1 to 2.5 mCi in increments of 0.25 mCi. We calculated the activity of Tc-99m so that the total effective dose was kept constant at 13.5 mSv [142, 143]. We selected this as the dose level for investigation given current concerns over patient radiation dose. The count levels in this study could also be achieved by a lower dose, e.g., 10 mSv, with longer acquisition duration, e.g., 35% longer than the standard acquisition duration. Table 7-1 shows the different injected activities of Tc-99m and T-201, labeled as R_1 to R_7, modeled in this study. To study the effects of window widths, we varied the width of the Tl-201 energy window from 4 to 40 keV in 4 keV increments with the window center fixed at 72 keV; these windows are labeled W_1 to W_{10} as shown in Table 7-2. Also note that, for all the investigated Tl-201 energy windows, we added the detected counts in a 156-180 keV window to the lower acquisition energy window to include the contribution of the 167 keV Tl-201 photopeak. Due to the negligible contribution of Tl-201 to Tc-99m image as illustrated by Figure 7-4, we did not optimize Tc-99m window width. We used a 20% window centered at 140.5 keV, a typical recommended energy window for Tc-99m imaging and one we have found to be in the optimal range in previous work [4]. Sample projections from Tc-99m and Tl-201 acquired in a 20 keV wide Tl-201 energy window for the different relative injected activities are shown in

Figure 7-5. Note the increasing amount of Tc-99m downscatter in the Tl-201 window from left to right as well as the decreased noise in the Tl-201 images as the Tl-201 activity increases (from right to left). Figure 7-6 demonstrates the tradeoff between noise and amount of scatter when increasing the width of the Tl-201 acquisition energy window.

Table 7-1. Tl-201 and Tc-99m activities

	Tc-99m activity (mCi)	Tl-201 activity (mCi)	Relative injected activity
R_1	1.7	2.5	0.8
R_2	5.9	2.25	2.6
R_3	10	2	5
R_4	14.1	1.75	8.1
R_5	18.2	1.5	12.1
R_6	22.3	1.25	17.8
R_7	26.5	1	26.5

Table 7-2. Investigated Tl-201 energy window settings.

	W_1	W_2	W_3	W_4	W_5	W_6	W_7	W_8	W_9	W_{10}
Lower threshold (keV)	70	68	66	64	62	60	58	56	54	52
Upper threshold (keV)	74	76	78	80	82	84	86	88	90	92
Width (keV)	4	8	12	16	20	24	28	32	36	40
Width (%)	5.5	11.1	16.7	22.2	27.8	33.3	38.9	44.4	50	55.6

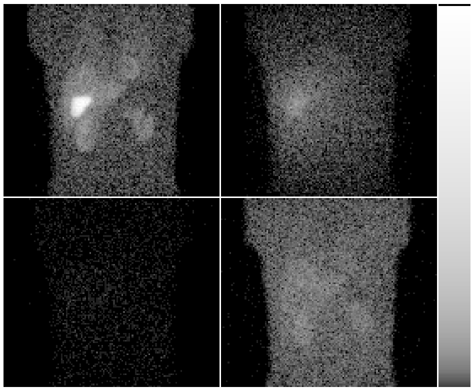

Figure 7-4. Sample noisy projection images for Tc-99m (Top row) and Tl-201 (bottom row) acquired in a 20% wide Tc-99m energy window (left) and 28% wide Tl-201 energy window, W_5 (right). Activities of Tc-99m and Tl-201 correspond to configuration R_3. Images are displayed on a logarithmic gray scale to show more clearly the lower uptake organs.

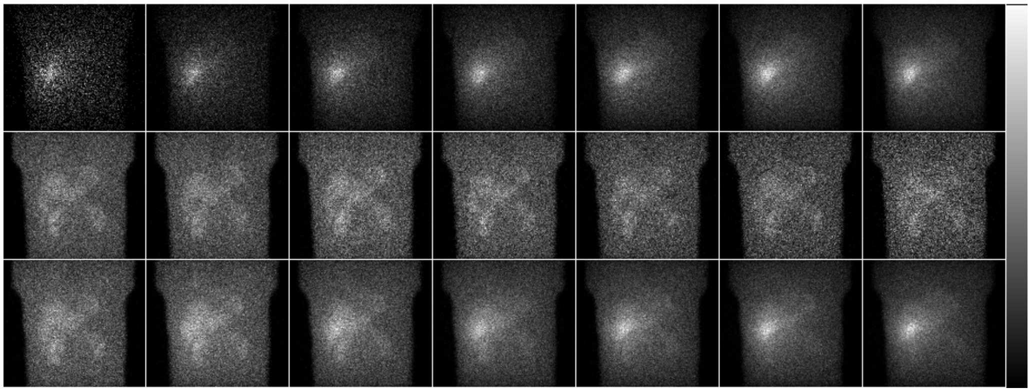

Figure 7-5. Sample noisy Tc-99m (top), Tl-201 (middle) and summed (bottom) projection images acquired in a 20 keV wide Tl-201 energy window (W_5). The Tc-99m and Tl-201 activities correspond to the activity combinations R_1 to R_7 from left to right.

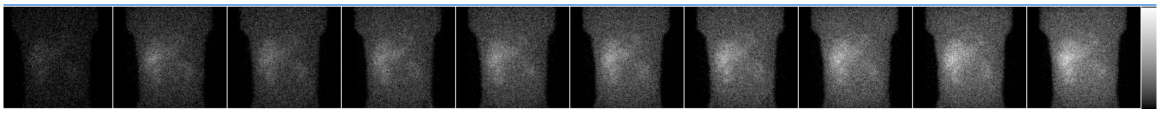

Figure 7-6. Sample noisy projection images acquired in Tl-201 energy windows W_1 to W_{10} from left to right including crosstalk from Tc-99m into the Tl-201 window.

7.2.2 Three-class ideal observer study

In this section, we review the ideal decision strategy and accompanying ideal observer for the 3-class detection task. In a binary detection task, the goal is to determine whether or not a signal is present based on the measured data. However, for the 3-class MPS detection task the observer is required to classify the patient as being normal (class 1) or having a fixed (class 2) or reversible (class 3) perfusion defect. The 3-class hypotheses to be tested can be represented mathematically by:

$$H_N : \mathbf{g} = \mathbf{b} + \mathbf{n},$$

$$H_F : \mathbf{g} = \mathbf{b} + \mathbf{s}_F + \mathbf{n},$$

$$H_R : \mathbf{g} = \mathbf{b} + \mathbf{s}_R + \mathbf{n},$$

where $\mathbf{g}, \mathbf{b}, \mathbf{s}_F, \mathbf{s}_R$ **and** $\mathbf{n}$ are the noisy projection, background, fixed defect, reversible defect and noise vectors, respectively and the hypotheses H_N, H_F **and** H_R mean signal absent, fixed and reversible defects present, respectively.

The ideal observer uses the likelihood ratio, or any monotonic transformation thereof such as the log-likelihood ratio, of defect-present vs. defect-absent as the decision variable. To construct the 3-class ROC surface and compute the VUS, it is necessary to calculate the log-likelihood ratios $\mathbf{\log \Lambda_{N,R}(g)}$ and $\mathbf{\log \Lambda_{F,R}(g)}$ defined as,

$$\log \Lambda_{\mathrm{N,R}}(\mathbf{g} \mid \mathrm{b}) = \log \frac{pr(\mathbf{g} \mid H_{\mathrm{R}})}{pr(\mathbf{g} \mid H_{\mathrm{N}})}, \tag{7.1}$$

$$\log \Lambda_{\mathrm{F,R}}(\mathbf{g} \mid \mathrm{b}) = \log \frac{pr(\mathbf{g} \mid H_{\mathrm{R}})}{pr(\mathbf{g} \mid H_{\mathrm{F}})}. \tag{7.2}$$

Although using the IO to optimize the acquisition protocols is theoretically appealing, it is technically difficult to calculate the IO test statistics (log-likelihood ratios) for realistic populations of realistic objects. The expression for the log-likelihood ratio in the case when background variability is included would be the average over the backgrounds with the posterior densities $\mathbf{pr(g \mid H_N)}$ and $\mathbf{pr(g \mid H_F)}$, densities that are usually complex and unknown and thus hard to sample from [24]. Markov Chain Monte Carlo (MCMC) methods have been developed to allow estimating the log-likelihood ratios using Monte Carlo methods [33, 34, 111].

To apply this method, we parameterized the objects, and thus the projection data arising from them, by the object parameter vector, $\vec{\theta} = \left[n, p, q, l, A_{\text{heart}}, A_{\text{liver}}, A_{\text{body}} \right]$. $\vec{\theta}$ was a combination of discrete and continuous parameters: n, p, q and l were integer parameters specifying the object gender, body size, heart size and subcutaneous adipose tissue thickness, and A_{heart}, A_{liver} and A_{body} were scalar parameters representing the total activity in the heart, liver and body, respectively. Thus, the total projection, $\mathbf{prj}\left(\vec{\theta}\right)$, given the object parameter vector, $\vec{\theta}$, was represented as:

$$\mathbf{prj}\left(\vec{\theta}\right) = A_{\text{heart}} \mathbf{prj}_{n,p,q,l}^{heart} + A_{liver} \mathbf{prj}_{n,p,q,l}^{liver} + A_{body} \mathbf{prj}_{n,p,q,l}^{body} \tag{7.3}$$

where $\mathbf{prj}^{\mathbf{heart}}$, $\mathbf{prj}^{\mathbf{liver}}$ **and** $\mathbf{prj}^{\mathbf{body}}$ were the projections of the heart, liver and the body (including other organs), respectively, filled with unit activity for the anatomy specified by n, p, q and l.

We adopted a Metropolis–Hastings approach to draw samples, $\vec{\theta}^{(0)}, \vec{\theta}^{(1)}, \ldots, \vec{\theta}^{(k)}, \ldots, \vec{\theta}^{(N)}$ where N is the number of iterations (N=50x10^3), from the posterior distributions $pr(\vec{\theta} \mid \mathbf{g}, H_N)$ and $pr(\vec{\theta} \mid \mathbf{g}, H_F)$ for the expressions 7.1 and 7.2 respectively, and computed the ergodic averages $\log \tilde{\Lambda}_{\mathrm{N,R}}\left(\mathbf{g} \mid \mathrm{b}\right)$ and $\log \tilde{\Lambda}_{\mathrm{F,R}}\left(\mathbf{g} \mid \mathrm{b}\right)$. We discarded the first 20,000 iterations, which are referred to as the burn-in iterations, to ensure the stabilization of each Markov chain. To efficiently apply MCMC IO estimation, we precomputed the noise-free projection images $\mathbf{prj}_{n,p,q,l}^{heart}$, $\mathbf{prj}_{n,p,q,l}^{liver}$ and $\mathbf{prj}_{n,p,q,l}^{body}$ for each phantom in the population. This constituted a database of 54 different anatomies. For a given parameter vector, $\vec{\theta}^{(k)}$, we located the corresponding anatomy using the indexes n, p, q and l and the signal-absent (background) projection image could then be generated by scaling and summing the three organ projections using the scalar activity parameters $A_{\mathbf{heart}}$, $A_{\mathbf{liver}}$ **and** $A_{\mathbf{body}}$.

Figure 7-7 shows the log-likelihood ratios, $\mathbf{log}\,\boldsymbol{\Lambda}_{\mathbf{N,R}}\left(\mathbf{g}\right)$ and $\mathbf{log}\,\boldsymbol{\Lambda}_{\mathbf{F,R}}\left(\mathbf{g}\right)$ for one sample input projection image as a function of the iteration number. The input projection image had a fixed perfusion defect in the antero-lateral wall of the heart, i.e., a defect that was present in both the stress and rest images.

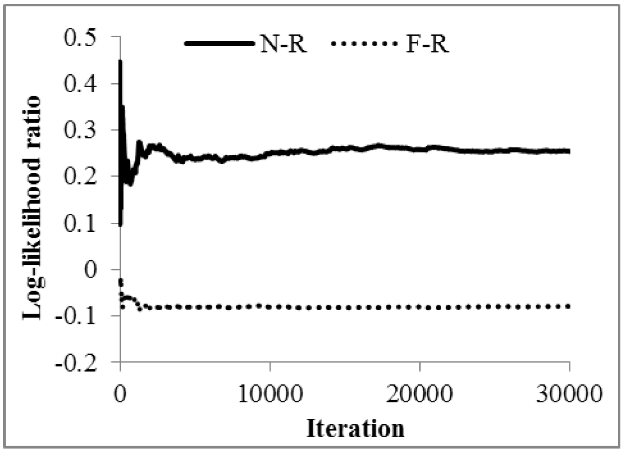

Figure 7-7. A plot of the log-likelihood ratio versus iteration number for an input projection image with a fixed perfusion defect in the anterolateral wall.

For each combination of energy window and relative injected activity, we computed the IO test statistic using the MCMC method for an ensemble of 1,620 (54 phantoms x 2 defect locations x 15 uptake realizations) triplets of fixed and reversible and normal noisy images, $\mathbf{g}$, modeling variations in anatomical and organ uptake. Figure 7-8 shows the decision plane with a scatter plot of the pairs of test statistics for each class. Each projection image, $\mathbf{g}$, was comprised of two images, the rest and stress images, stacked together. Each of the stress and rest projection data contained a 64x24x60 pixel region of interest centered over the heart centroid. This ensured that the whole heart was included inside the region-of-interest. This gave a set of 4,860 test statistics (1,620 for each of the 3 classes) for each energy window and injected activity combination that was then analyzed using 3-class ROC methodology to estimate the VUS [136, 139]. The VUS was estimated using a bootstrap procedure that also provided estimates of the standard deviation of the VUS.

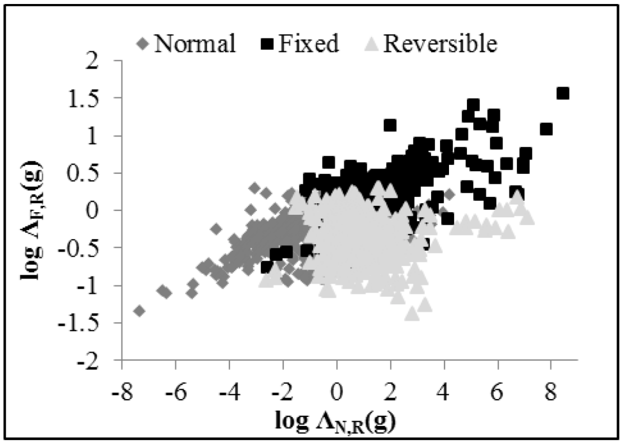

Figure 7-8. Decision plane for simulated dual-isotope MPS images for relative injected activity R_3 and acquisition energy window W_5.

7.3 Results and discussion

7.3.1 Dual isotope imaging with simultaneous acquisition

In this section, we present results for the case of simultaneous acquisition of the stress and rest images.

7.3.1.1 Stress Tc-99m and rest Tl-201 image qualities

In simultaneous acquisition, the quality of the stress image has a direct relationship to the injected activity of Tc-99m. However, the quality of the rest image degrades with increasing injected activity of Tc-99m due to crosstalk. Thus, there is an inverse relationship between the qualities of the stress and rest images. We performed a binary observer study to assess the quality of each of the stress and rest images with respect to a binary detection task. For the stress image, we pooled the defect–present images from the fixed and reversible classes and used the normal class images as defect–absent. For the rest image, we used the fixed class images as defect-present and pooled the defect–absent images from the normal and reversible classes.

Figure 7-9 shows the IO performance for the rest and stress images for the different relative injected activities and Tl-201 energy windows. The error bars on the AUC values were small (typically on the order of 5×10^{-3}). The quality of the stress Tc-99m image improved when the Tc-99m injected activity increased (from left to right). The improvement in performance was small for higher injected activities and was, as expected, independent of the Tl-201 acquisition energy window. This agrees with results previously reported in [4, 66]. For the rest Tl-201 image, we see that the performance improved as the Tl-201 injected activity increased (from right to left), corresponding to a concurrent reduction of the Tc-99m crosstalk. The rest image detection performance had a broad maximum in the center of the range of investigated Tl-201 energy windows. This is explained by the tradeoff between image noise, which decreases with increasing window width, and the amount of Tl-201 self-scatter and Tc-99m crosstalk, which increase as the width of Tl-201 energy window increases.

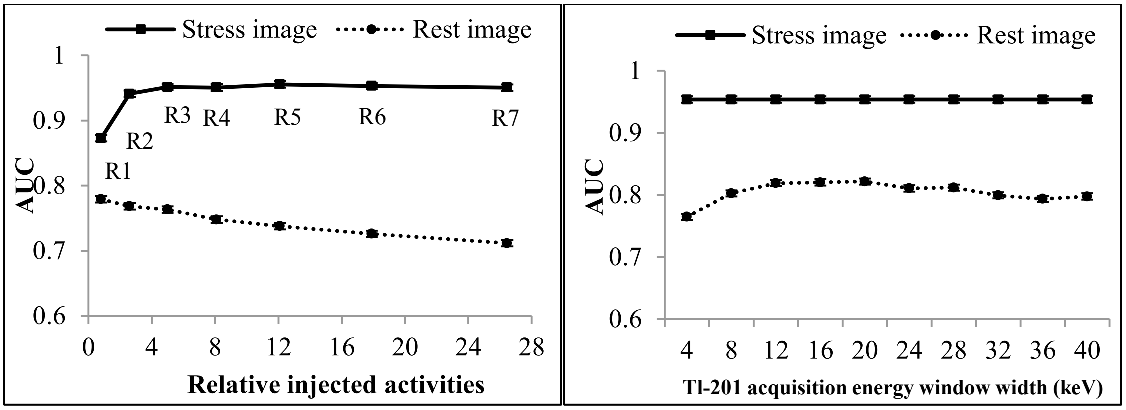

(a) (b)

Figure 7-9. Comparison of IO performances in a binary observer study to assess the qualities of stress Tc-99m and rest Tl-201 images for dual isotope simultaneous acquisition for (a) the different injected activities and energy window W_5 and (b) the Tl-201 energy window widths and relative injected activity R_3.

7.3.1.2 Pairwise comparison of the 3 classes

To shed light on the underlying tradeoffs and difficulty of distinguishing the classes, we performed binary observer studies that involved pairwise comparisons of the classes, i.e., normal versus fixed defect (N-F), reversible versus fixed defect (R-F), and normal versus reversible defect (N-R). In all cases, both the rest and stress images were provided to the IO. Figure 7-10 shows the AUC values for the three pairs of classes for (a) the different relative injected activities and (b) the Tl-201 acquisition energy window widths.

To understand the trends in these figures, first consider the effect of the quality of the rest and stress images on these different tasks. Table 7-3 shows the different defect statuses in the rest and stress images for each pair of classes. Distinguishing between normal and a fixed defect involves a difference in defect status in both the rest and stress images. Distinguishing between normal and reversible involves a change in only the stress image. Distinguishing between reversible and fixed involves only a change in the rest image.

Table 7-3. Change in defect status in Rest and Stress Images for the pairs of classes

Classes (1 vs. 2)	Rest*	Stress*
Fixed vs. Normal	+, –	+,–
Fixed vs. Reversible	+, –	+,+
Normal vs. Reversible	–,–	–,+

*In these columns the first symbol indicates the presence (+) or absence (–) of a defect in the first class and the second symbol indicates the presence or absence in the second class.

Consider first the effect of relative injected activities. From Figure 7-10 (a), performance in distinguishing reversible and fixed defects increased with increasing Tl-201 activity (right to left). This reflects the fact that detecting this difference depends on detecting the defect in the rest image: increasing Tl-201 activity both decreased noise in the Tl-201 image and reduced crosstalk from Tc-99m. Also note that performance for this pair of classes was worse than for the other pairs of classes in the cases where the relative injected activity was less than 2.6. For the cases of normal versus fixed and normal versus reversible, the IO performance decreased as Tl-201 activity increased (from right to left). However, the performance decrease was greater for the case of normal versus reversible, which depends only on the stress image. In this case the reduction in noise and crosstalk in the rest image did not offset the degraded quality in the stress image due to less Tc-99m activity and thus greater noise. However, for the normal versus fixed case, improvement in the rest image quality partially offsets the degraded image quality of the stress image.

Figure 7-10 (b) shows the effects of varying the Tl-201 energy window width on performance for the 3 pairs of 2-class tasks. For the cases of normal versus fixed and normal versus reversible, performance decreased modestly with increasing Tl-201 energy window width, with the decrease somewhat larger for the normal versus reversible case. For the case of reversible versus fixed, there was a range of optimal energy windows (W_3-W_4), indicating that there is a balance between noise, which decreases, and scatter and crosstalk, which increase with increasing Tl-201 energy window width.

The results in Figure 7-9 and Figure 7-10 confirm that it was impossible to determine the optimal parameters for dual isotope imaging using a 2-class optimization paradigm. For example, in Figure 9(a), rest image quality degrades while stress image quality increases with increasing relative injected activity. Similarly, in Figure 10(b), discrimination between no defect and fixed defect or no defect and reversible defect is best with the narrowest Tl-201 energy window while discrimination of the reversible versus fixed defects was best for an intermediate energy window width. The optimal tradeoff between these factors is not clear, and it was thus important to consider the 3-class nature of the problem.

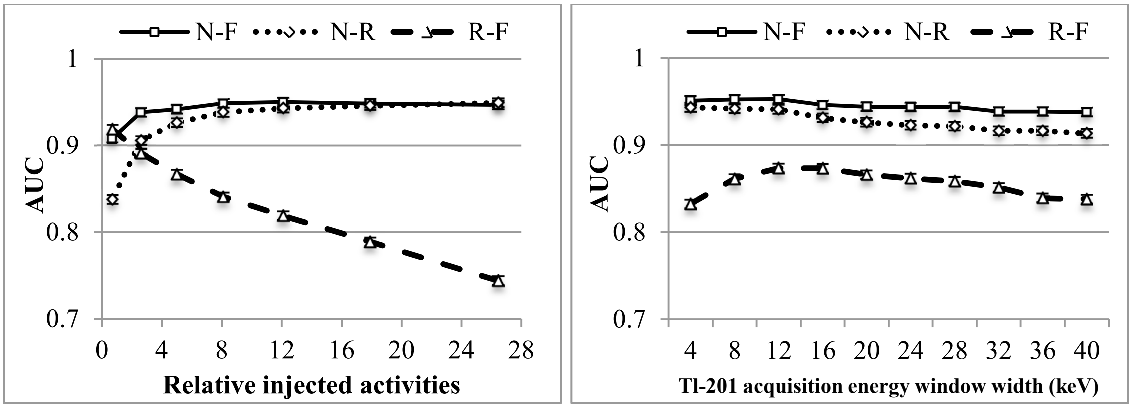

(a) (b)

Figure 7-10. Comparison of pairwise binary observer performance and three-class observer performance for dual isotope simultaneous acquisition for (a) the different injected activities and energy window W_5 and (b) the various Tl-201 energy window widths and relative injected activity R_3.

7.3.1.3 3-Class IO study

Figure 7-11 shows a 2D contour plot of the VUS values for the different relative injected activities and Tl-201 acquisition energy windows. The standard deviation of the VUS values was about 0.01. The data suggest that optimal relative injected activities of 2.6-5 (R_2-R_3) and acquisition energy window widths of 8-16 keV (W_2-W_4) were optimal (VUS = 0.806). Also note that the optimal injected activities were the same for the different acquisition windows, as indicated by the shape of the contours. We tested the statistical significance of the differences between the VUS value of the configuration that had the maximum VUS (i.e. a 2.6 relative injected activity and a 12 keV Tl-201 energy window wide) and that of the relative injected activities from 0.8 to 8.1 (R_1-R_4) and acquisition energy windows with widths from 4 to 20 keV (W_1-W_5) on a pair-wise basis. The corresponding *p*-values, indicating the probability that differences between VUS_1 and VUS_2 were due to chance, are shown in Table 7-4. The gray-shaded cells indicate that the differences between the VUS values were not significant at the level p=0.05.

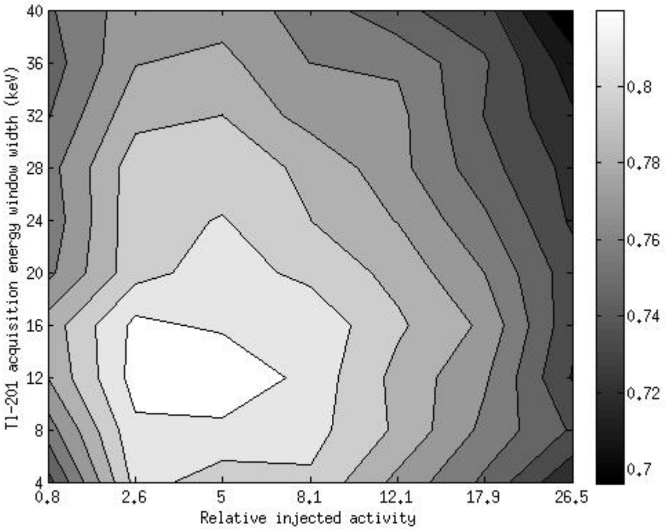

Figure 7-11. 2D contour plot of the VUS values for the different injected activities and acquisition energy windows for dual isotope simultaneous acquisition.

Table 7-4. Results of statistical significance tests for the optimal VUS value and the different configurations

Energy window width (keV) / Relative injected activity	0.8	2.6	5	8.1
4	1.15E-13	8.41E-04	7.11E-07	9.43E-04
8	6.20E-14	9.36E-03	2.89E-01	4.02E-02
12	1.55E-09	Max	7.00E-01	3.40E-02
16	1.59E-05	4.02E-01	7.03E-02	1.32E-02
20	5.54E-11	7.48E-03	4.09E-02	1.79E-06

7.3.2 Dual isotope imaging with separate acquisition

We studied the case of separate acquisition of the stress and rest images, i.e., where there was no crosstalk between the two images and thus the qualities of the stress and rest images were independent of each other. The goal of this study was to compare the optimal acquisition parameters to the case of simultaneous acquisition and determine if there was significant improvement for using the separate acquisition over the simultaneous acquisition.

7.3.2.1 Stress Tc-99m and rest Tl-201 image qualities

We performed a binary observer study to evaluate the performance of the IO in assessing the qualities of the rest Tl-201 and stress Tc-99m images interpreted separately. Figure 7-12 shows IO performance as a function of the relative injected activities where images were acquired in a 20 keV wide Tl-201 window (W_5). We observed similar patterns for the different energy windows. The results shown in Figure 12 indicate that increasing the injected activity of Tl-201 (from right to left) results in an improvement of rest image quality but a decrease in stress image quality (due to the reduction in Tc-99m activity needed to maintain a constant effective radiation dose).

Examining Figure 9(a) and Figure 12 shows that the observer performed better on the rest image in the simultaneous acquisition case (when crosstalk was present) than in the separate acquisition case. This unexpected result can be understood by considering the images used by the observer. For the simultaneous acquisition case, the rest (Tl-201) defect absent images were from both the normal and reversible classes, while the defect present images were from the fixed defect class. The crosstalk in the Tl-201 image is a low-frequency version of the Tc-99m image. Thus, for the defect present case, crosstalk represents the ‘same’ perfusion state and does not degrade the observer's interpretation of the rest image; indeed, it could theoretically improve it by adding counts. For the defect absent case, the same is true for images from the normal class. That is, it is only for the defect absent case with images from the reversible class where the rest and stress images represented a different perfusion state and thus where crosstalk would have degraded observer performance. Apparently, the fact that crosstalk could actually reinforce the information about defect status in the rest image in two of the three cases was enough to improve overall rest defect detection performance.

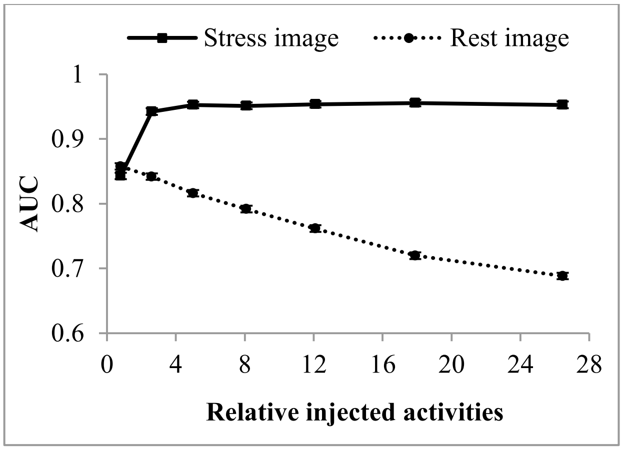

Figure 7-12. Comparison of IO performances in a binary observer study to assess the qualities of stress Tc-99m and rest Tl-201 images for dual isotope separate acquisition.

7.3.2.2 Pairwise comparison of the 3 classes

As was the case with simultaneous acquisition, we compared performances for the binary task of distinguishing between the various pairs of classes. Figure 7-13 shows the IO performance for the three pairs of classes in terms of AUC for the different relative injected activities, acquired with Tl-201 acquisition energy window W_5. The trends were similar to those for simultaneous acquisition, though the degradation in the IO performance for distinguishing between reversible and fixed defects was greater for the simultaneous acquisition as the Tc-99m injected activity increased (left to right).

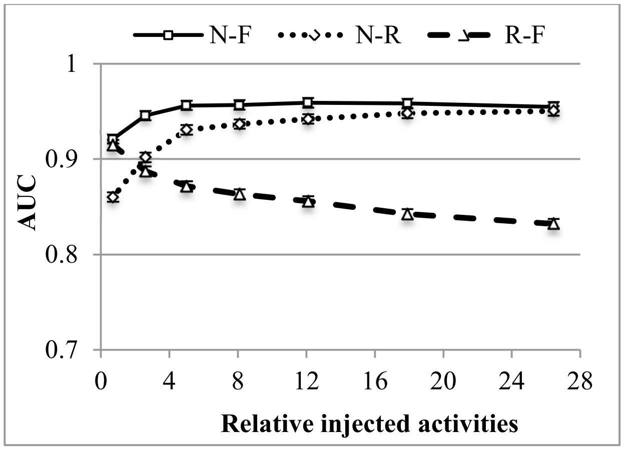

Figure 7-13. Comparison of pairwise binary observer performance (measured in terms of AUC) with three-class observer performance (measured in terms of VUS) for dual isotope separate acquisition.

7.3.2.3 3-Class IO study

The optimal injected activity could, in principle, vary as a function of Tl energy window. Figure 7-14 shows a 2D contour plot of the VUS values for the different relative injected activities and Tl-201 acquisition energy windows. The standard deviation of the VUS values was about 0.01. The plot shows that the IO had a maximum VUS value (VUS =0.809) when performing on images acquired using a relative injected activity of 8.1 (R_4) and an 8 keV wide acquisition energy window (W_2). However, the differences between the VUS value for the configuration (R_4, W_2) and that of many of the other configurations were not statistically significant at a confidence level of p=0.05, as shown in Table 7-5 (the gray-shaded cells indicate that the differences between the VUS values were not significant). Therefore, there was a much wider range of near-optimal injected activities and Tl-201 energy windows than for simultaneous acquisition.

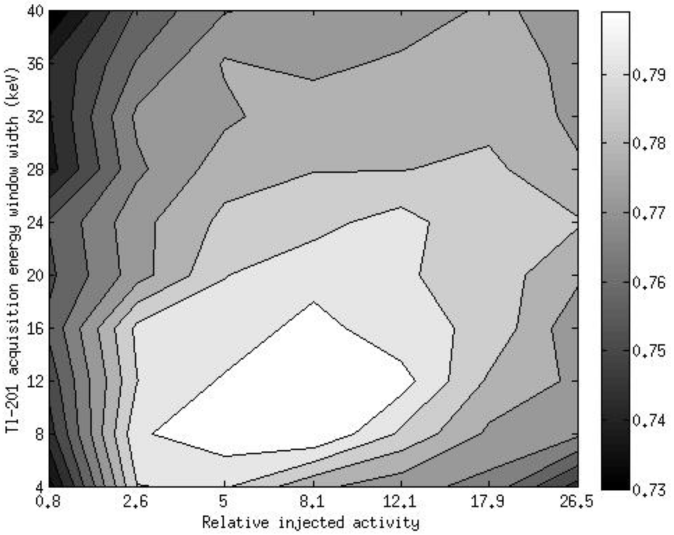

Figure 7-14. 2D contour plot of the VUS values for the different injected activities and acquisition energy windows for dual isotope separate acquisition

Table 7-5. Results of statistical significance tests for the optimal VUS value and the different configurations

Energy window width (keV) / Relative injected activity	0.8	2.6	5	8.1	12.1	17.8
4	3.97E-10	2.08E-03	3.27E-02	1.39E-04	2.34E-07	5.52E-05
8	4.12E-08	3.09E-01	8.17E-01	Max	5.68E-03	6.18E-04
12	1.04E-08	2.32E-03	4.97E-01	1.83E-01	8.16E-01	1.05E-04
16	1.68E-08	1.44E-02	1.10E-02	5.79E-01	1.28E-01	1.96E-03
20	2.47E-07	3.74E-05	2.00E-03	2.99E-02	2.63E-04	1.82E-03

7.3.3 Comparison between simultaneous and separate acquisition protocols

We compared the optimal parameters that yielded the best performance for both simultaneous and separate acquisition protocols. Table 7-6 shows the ranges of optimal acquisition parameters for simultaneous and separate acquisitions as well as the observer performance for the binary and 3-class defect detection tasks. The observer favored higher Tc-99m injected activities (less Tl-201) for separate acquisition than simultaneous acquisition.

The reduced Tc-99m would reduce the effect of crosstalk on image quality for simultaneous acquisition. As shown in Table 7-6, there was an inverse relation between the stress and rest image qualities for simultaneous and separate acquisitions. The observer performance on the rest image for simultaneous acquisition was better than that for separate acquisition. The inverse was also true for the stress image.

In the simultaneous acquisition case, the optimal injected activities were the same for the different acquisition windows. Similarly, the optimal energy windows were the same for the different injected activities. However, for the separate acquisition case, we observed dependence between the optimal relative injected activity and the acquisition energy window, as indicated by the shape of the contours. That is, when the injected activity of Tl-201 decreased (increasing the relative injected activity and producing better stress images and noisier rest images), the IO tended to perform better with wider Tl-201 acquisition energy windows, i.e., acquired more photons to compensate for the reduction in Tl-201 count level. Similarly, when the injected Tl-201 activity increased (reduced relative injected activity) the IO performed better with narrower energy windows.

We also observed that the degradation in the IO performance as a function of Tl-201 energy window width for simultaneous acquisition was higher than that of separate acquisition, as indicated in Figure 7-11 and Figure 7-14. This can be explained by the additional negative effect that crosstalk has on observer performance beyond Tl-201 self-scatter. As the energy window width increased, the amount of Tc-99m crosstalk increased, which is an image-degrading factor that only affects image quality in dual isotope imaging with simultaneous acquisition.

Also note that the performance of the observer when operating on images acquired using separate or simultaneous acquisition was similar ($VUS_{Simultaneous}=0.806$, $VUS_{Separate}= 0.809$). We tested the statistical significance of the difference between the VUS values for both protocols and the corresponding p-value at 95% confidence level was equal to 0.92, i.e., the difference was not statistically significant. This suggests that DISA methods can potentially provide image quality as good as that obtained with separate acquisition with a factor of ~2 reduction in total acquisition time, while also providing reduced time for patient positioning and perfect stress and rest image registration.

7.3.4 Comparison between optimized and clinical acquisition protocols

In this work, we investigated various injected activities of Tc-99m and Tl-201 so that the total effective dose was kept constant at 13.5 mSv. This is about half the effective dose that is currently given to patients undergoing dual isotope imaging with sequential acquisition. We selected this as the dose level for investigation given current concerns over patient radiation dose. In this section, we compare between separate acquisition protocols using the optimal acquisition parameters (i.e., Tl-201 acquisition energy window and Tc-99m/Tl-201 relative injected activity) and the clinical protocols currently used for dual isotope imaging with separate acquisition. The goal of this experiment was to determine if the existing protocols provide better task performance as measured by the IO performance on the binary and 3-class tasks. We measured the performance on images acquired using 30 mCi of Tc-99m and 3 mCi of Tl-201. Stress images were acquired in a 20% acquisition energy window, centered at 140 keV, while rest images were acquired in a 27% wide Tl-201 energy window. These acquisition parameters correspond to those used to acquire the clinical data for patients in a dual isotope imaging protocol with separate stress and rest acquisitions.

As shown in Table 7-6, the clinical protocol provided better task performance for both binary and 3-class tasks. This is because of the improved rest and stress image qualities due to higher injected Tc-99m and Tl-201 activities. However, we observed only modest improvement in the stress image quality, as measured by the observer performance, although the injected activity of Tc-99m was 30 mCi compared to 14 mCi used in the optimized protocol. This can be explained by the fact that the IO performance saturates for high Tc-99m injected activity, as shown in Figure 7-9 and Figure 7-12. Thus, there was no need to increase Tc-99m activity beyond 14 mCi. This also explains the modest improvement in observer performance in distinguishing normal versus fixed and normal versus reversible defects. These pairs of classes primarily depend on the change of defect status in the stress images, as indicated in Table 7-3. The IO performance on the three-class for the clinical protocol was substantially better than for the optimized low-dose protocol. This was mainly due to improvement in the rest image quality.

Table 7-6. Acquisition parameters and observer performance for the optimized and clinical dual isotope protocols

	Optimized protocol		Clinical protocol
Acquisition type:	Simultaneous	Separate**	Separate
Acquisition parameters:			
(a) Injected activities (mCi):			
Tc-99m	5.9-10*	5.9-18.2*	30
Tl-201	2-2.25*	1.5-2.25*	3
Relative injected activity	2.6-5*	2.6-12.1*	10
Total effective dose (mSv)	13.5	13.5	27.5
(b) Energy window width (%):			
Tc-99m	20	20	20
Tl-201	16.6-22.2*	11.1-22.2*	27.8
2-class IO performance:			
(a) Rest and stress image qualities			
Rest Tl-201	0.819	0.751	0.792
Stress Tc-99m	0.938	0.951	0.953
(b) Pairwise comparison between the 3 classes			
Normal Vs. Fixed	0.949	0.960	0.961
Normal Vs. Reversible	0.919	0.944	0.947
Reversible Vs. Fixed	0.892	0.862	0.875
3-Class IO performance:			
VUS	0.805	0.809	0.82

* Range of optimal acquisition parameter

** Note the dependence of optimal Tl-201 injected activity, (and thus Tc-99m activity) and Tl-201 energy window width

7.4 Conclusion

Dual isotope simultaneous acquisition Tc-99m stress/ Tl-201 rest MPS is an appealing protocol that offers a number of advantages over separate acquisition, including reduction in imaging time and an associated increase in patient comfort, inherent registration of the rest and stress images, and an increase in clinical throughput. However, crosstalk contamination, where photons emitted by Tc-99m contribute to the Tl-201 image due to interactions in the patient and gamma camera, degrades image quality. In this work, we optimized the Tl-201 energy window width and relative injected activities, in the context of a 3-class detection task, to reduce the impact of crosstalk. The optimization was performed using the IO and a SKE/BKS task operating on a realistic population of phantoms that included anatomical and background variations. The results indicated that relative injected activities of 2.6-5 and an acquisition energy window width of 8-16 keV centered at 72 keV were optimal. For separate acquisition, we observed a broader range of optimal relative injected activities, 2.6 to 12.1, and acquisition energy window of widths of 8-16 keV. For the separate acquisition case, we observed a negative correlation between Tl-201 injected activity and the width of the Tl energy window within the above-mentioned ranges. The results also showed that, with optimal energy windows and relative injected activities, the IO performance was very similar (VUS=0.809 and 0.806) for separate and simultaneous acquisition. This indicates that, with appropriate compensation and reconstruction methods, DISA methods can provide equivalent performance compared to separate acquisition while providing the benefits identified above. We have also compared the observer performances for the optimized protocol and the current clinical protocol using separate acquisition. The current clinical protocols provided better performance in the context of binary and three-class defect detection tasks, at a cost of injecting the patient with approximately double the injected activity of Tc-99m and Tl-201, resulting in substantially increased radiation dose.

8. Conclusions

This chapter first summarizes the results of this work, discusses its contributions and finally gives some directions for future work suggested by this research.

8.1 Summary of results

Single-Photon Emission Computed Tomography (SPECT) has been widely used to assess myocardial perfusion and to provide diagnostic information regarding coronary artery disease (CAD) status. A SPECT system consists of one or more gamma cameras that are rotated around the patient. The cameras acquire planar (projection) images of the three dimensional (3-D) distribution of a radioactive labeled perfusion agent at different projection views. Transaxial reconstructed images are formed using tomographic image reconstruction methods from these projections. However, the quality of the reconstructed images is affected by the instrumentation, acquisition parameters and reconstruction /compensation methods used. It is thus desirable to build instruments and develop acquisition protocols and reconstruction methods that yield the best image quality.

Ultimately, we would like to use patient data to evaluate system design, acquisition parameters and reconstruction methods so the results would be clinically relevant. However, due to radiation concerns and difficulty in obtaining true perfusion status, it is impractical to optimize the large number of instrumentation and acquisition parameters that affect image quality with human, animal or physical phantoms studies. A practical alternative is using computer simulations. In order for the results of simulation studies to be clinically relevant, they must realistically model the clinical situation, including modeling patient populations and clinical imaging systems. In this work, we designed, developed and used a realistic digital phantom population using full Monte Carlo simulations of the image formation process. The design of the population and the methods used to make full MC simulations feasible are summarized in section 8.1.1. We used the phantom population to optimize and evaluate the major acquisition and instrumentation parameters for MPS. These include collimator design (section 8.1.2), which controls the resolution-noise tradeoff, and the acquisition energy window (section 8.1.3), which controls the tradeoff between scatter, which reduces image contrast, and noise. For dual isotope imaging (section 8.1.4), the tradeoffs are more complex, since crosstalk from one radionuclide degrades the images of the other. For the dual isotope case we thus optimized the rest Tl-201 acquisition energy window and the Tc-99m and Tl-201 injected activities ratios under the constraint of fixed total effective radiation dose.

We developed and applied task-based image quality assessment methods and metrics. These methods and metrics were used to optimize and evaluate the instrumentation, acquisition parameters and compensation methods in terms of performance on the diagnostic tasks relevant to MPS.

8.1.1 Design of a digital phantom population for myocardial perfusion SPECT imaging

Digital phantoms and Monte Carlo simulations have become important tools for optimizing and evaluating instrumentation, acquisition and processing methods for MPS. In this work, we designed a new adult digital phantom population and generated corresponding Tc-99m and Tl-201 projections for use in MPS research. The population is based on the 3D eXtended Cardiac Torso (XCAT) phantom with organ parameters sampled from the Emory PET Torso Model Database. Phantoms included 3 variations each in body size, heart size, and subcutaneous adipose tissue level, for a total of 27 phantoms of each gender. These three parameters were varied because they were expected to have an impact on MPS image quality. The SimSET MC code and angular response functions were used to model interactions in the body and the collimator-detector system, respectively. These methods provide very realistic simulations of the physical image degrading effects present in real SPECT imaging systems. We divided each phantom into seven organs, each simulated separately, allowing use of post-simulation summing to efficiently model uptake variations. Also, we adapted and used a criterion based on the relative Poisson effective count level to determine the required number of simulated photons for each simulated organ. This technique provided a quantitative estimate of the true noise in the simulated projection data, including residual MC simulation noise. This provided a quantitative criterion for determining the simulation length and was important in enabling the large scale simulations undertaken here while ensuring that the resulting noise levels faithfully represented protocol parameters such as the injected activity and acquisition time rather than residual MC simulation noise. Projections were generated in 1 keV wide energy windows from 48-184 keV assuming perfect energy resolution to permit study of the effects of window width, energy resolution, and crosstalk in the context of dual isotope MPS by computationally efficient and physically realistic weighting and summing of the data in the 1 keV wide bins. Taken together, we have developed a comprehensive method for efficiently simulating realistic projections for a realistic population of phantoms in the context of MPS imaging. The phantom population and realistic database of simulated projections were useful in this work and will be useful in the future in performing mathematical and human observer studies to evaluate various acquisition and processing methods such as optimizing the energy window width, investigating the effect of energy resolution on image quality and evaluating compensation methods for degrading factors such as crosstalk in the context of single and dual isotope MPS.

8.1.2 Collimator optimization in MPS

In SPECT imaging, collimators are a major factor limiting image quality and largely determine the noise and resolution of the SPECT images. Chapters 4 and 5 addressed the collimator optimization problem. As with the rest of the work in this chapter, we sought to make the work clinically relevant by using the realistic phantom population described in Chapter 3 as well as relevant tasks and rigorous analysis of image quality. In Chapter 4, we sought the collimator with the optimal tradeoff between image noise and resolution with respect to performance on two tasks related to MPS: perfusion defect detection and joint detection and localization. We used the Ideal Observer (IO) operating on realistic background known statistically (BKS) and signal known exactly (SKE) data. We used the areas under the receiver operating characteristic (ROC) and localization ROC (LROC) curves, respectively, as the figures of merit for both tasks. These figures of merit have the advantage that they are independent of disease prevalence and the costs of various diagnostic errors. We used the population of 54 phantoms described in Chapter 3. The population was based on the XCAT phantom and included variations in gender, body size, heart size and subcutaneous adipose tissue level. For each phantom, organ uptakes were varied randomly based on distributions observed in patient data. We simulated perfusion defects at six different locations with extents and severities of 10% and 25%, respectively, which represented challenging but clinically relevant defects. We generated projection data using an analytical projector that modeled attenuation, scatter, collimator-detector response effects, a 9% energy resolution at 140 keV, and a 4 mm full-width at half maximum (FWHM) intrinsic spatial resolution. We investigated a family of eight collimators that spanned a large range of sensitivity-resolution tradeoffs. For each collimator and defect location, we computed the IO test statistic using a Markov Chain Monte Carlo (MCMC) method for an ensemble of 540 pairs of defect-present and -absent images that included the aforementioned anatomical and uptake variability. Sets of test statistics were computed for both tasks and analyzed using ROC and LROC analysis methodologies. The results of this study suggest that collimators with somewhat poorer-resolution and higher sensitivity than that of a typical low-energy high-resolution (LEHR) collimator used clinically for MPS appear optimal for both the defect detection and joint detection and localization tasks for the range of defect sizes investigated. This study also indicates that optimizing instrumentation for a detection task may provide near-optimal performance on the more complicated detection-localization task.

A limitation of the IO is that, since it has perfect knowledge of the image formation process, its performance reflects the best achievable with perfect compensation. When human observers interpret SPECT images that are reconstructed with imperfect or no compensation, the optimum reconstruction parameters and ultimate performance may thus differ from those identified by the IO. To address this, we developed and applied the Ideal Observer with Model Mismatch (IO-MM), an observer that allows optimization of acquisition and instrumentation parameters in the absence or presence of non-ideal compensation methods and evaluate the m in terms of the IO. Like the IO, it allows optimization in the projection data and uses all the statistical information about defect status available in the data. In MPS imaging, the collimator-detector response (CDR) is the primary factor that determines the spatial resolution of SPECT images. It is desirable to compensate for the various components of CDR including geometric, septal penetration and scatter, and detector intrinsic resolution. One question is whether the optimal collimator is the same when compensating for these as compared to no compensation. In chapter 5, we used the IO and IO-MM to find the optimal collimator and evaluate various CDR modeling and compensation methods such as modeling the full CDR, geometric response only and when no model of the CDR was included. The IO suggested that a collimator with a resolution of 0.9-1.1 cm FWHM at 10 cm was optimal. When the IO-MM used an approximate or no model of the CDR, the optimal collimator shifted toward higher resolution (FWHMs of 0.9 cm and 0.7 cm at 10 cm, respectively) than that obtained using the IO, where the observer implicitly used a true CDR model. Results also indicated that the optimal collimator in terms of defect detection performance when modeling the geometric response only, was very similar to the case of using the true CDR. We also compared the performance of the IO and IO-MM with an anthropomorphic model observer, the Chanelized Hotelling Observer (CHO). The IO-MM and CHO had the same rankings of the CDR compensation methods and gave similar optimal collimators for the different compensation methods. This indicates that the IO-MM may be useful as a surrogate for optimizing acquisition and instrumentation in cases where threre is significant model mismatch in the reconstruction methods used to generate images for human observer MPS defect detection.

8.1.3 Optimization of Tc-99m acquisition energy window in MPS

In MPS imaging, detection of scattered photons reduces the contrast of perfusion defects and thus has a significant impact in limiting the diagnostic accuracy of readers interpreting the images. Since photon energy descreases after scatter, energy window width is a parameter available to reduce the amount of scatter in the images. However, because of the finite energy resolution of SPECT systems, using narrow energy windows to reject scatter also rejects a significant fraction of unscattered (primary) photons, resulting in an increase in image noise. There will thus always a significant fraction of the projection data that is due to scattered photons, and is desirable to compensate for scatter in order to reduce its effects on task performance. In this work, we used the IO and IO-MM to optimize the Tc-99m acquisition energy window and evaluate various scatter modeling and compensation methods, including the dual and triple energy window and the model-based Effective Source Scatter Estimation (ESSE) methods. The optimal energy window range when the IO-MM used an approximate model of scatter was narrower than that obtained using the IO, i.e., when the observer used the true scatter distribution. Results also indicated that the ESSE scatter model was similar to using the true scatter in terms of its effect on defect detection. We also compared the performance of the IO and IO-MM with an anthropomorphic model observer, the Chanelized Hotelling Observer (CHO) using difference-of-mesa channels. The IO-MM and CHO had the same performance rankings of the scatter estimation methods, with the ESSE method being the best and equal performance achieved when using the dual and triple energy window methods. The agreement of rankings for the IO-MM and CHO suggests that the IO-MM may be useful for optimization tasks, where there is significant model mismatch, due to its substantially reduced computational burden compared to the CHO.

8.1.4 Optimization and evaluation of dual isotope imaging protocols in MPS

Dual-isotope simultaneous-acquisition (DISA) rest-stress myocardial perfusion SPECT protocols offer a number of advantages over separate acquisition. However, crosstalk contamination, due to scatter in the patient and interactions in the collimator, degrades image quality. We have previously developed crosstalk compensation effects that provide good models of the crosstalk. While compensation can reduce the effects of crosstalk, it does not entirely eliminate image degradations. In particular, even compensation that perfectly models the imaging physics cannot remove the residual noise contributed by the crosstalk. Optimizing acquisition parameters (energy window width and relative injected activities) could thus further reduce the impact of crosstalk. The IO has been previously suggested for acquisition protocol optimization, but due to technical difficulties, it has not been seriously applied to data with realistic object variability. In this work we selected the IO as the observer since available crosstalk models are good and model mismatch is thus not a major issue. We modified and applied a previously proposed fast MCMC technique to estimate the IO test statistics using a realistic digital phantom population and Monte Carlo simulated Tc-99m and Tl-201 projections. We compared performance on a perfusion defect detection task for Tl-201 acquisition energy windows varying from (70-74) keV to (52-92) keV with increments of 4 keV in window width for a camera with a 9% energy resolution. We also investigated 7 different relative injected activities, defined as the ratio of Tc-99m and Tl-201 activities. We varied the Tl-201 activity from 1 to 2.5 mCi with increments of 0.25 mCi and calculated the activity of Tc-99m so that the total effective dose, a measure of the biological impact of radiation, was kept constant at 13.5 mSv. For each energy window and relative injected activity, we computed the IO test statistics using the MCMC-based method for an ensemble of 1,620 triplets of fixed and reversible defect-present, and defect–absent noisy images modeling realistic random variations in organ uptakes. The volume under the 3-class ROC surface was estimated and served as the figure of merit. For simultaneous acquisition, the IO suggested that relative injected Tc to Tl activity ratios of 2.6-5 and acquisition energy window widths of 16-22% were optimal. For separate acquisition, we observed a broader range of optimal relative injected activities from 2.6 to 12.1 and acquisition energy window of widths 11% to 22%. A negative correlation between Tl-201 injected activity and the width of the energy window was observed in these ranges. The results also suggested that DISA methods could potentially provide image quality as good as that obtained with separate acquisition protocols.

8.2 Summary of technical and methodological contributions

As described in sections 1.1 and 8.1, this dissertation produced a number of results that could have a significant clinical impact on myocardial perfusion imaging. In addition, the research presented in this dissertation made a number of contributions and innovations that are summarized below.

First, we performed a large and physically realistic simulation study using a realistic digital phantom population. In the study we generated a database of both Tc-99m and Tl-201 projections. Since the phantoms were based on the 3-D XCAT phantom, the population provides a highly realistic model of human anatomy. The Tc-99m and Tl-201 projection databases were generated in 1 keV wide energy windows. This allows modeling any desired energy resolution function and acquisition energy window by appropriately scaling and summing the 1 keV wide projections. To make the simulation of the phantom population computationally feasible, we developed and used several techniques to efficiently simulate realistic projections for such a population. This included using efficient MC simulation methods such as SimSET and angular response functions. We have also developed methods based on the relative Poisson effective count level to characterize residual MC noise and determine the required number of simulated photons for each simulated organ. This was essential to ensure that we simulated an adequate number of photons but not too many to make the simulation computationally infeasible. Another technique that we used to make the phantom library general and the simulation computationally feasible was to simulate the organs separately. This enabled modeling of organ uptake variability by scaling and summing the projection data from the individual organs.

Despite all the methods used and developed to make the simulation computationally feasible, the production of the population and the projection database required ~800 CPU years and a total of 2.6 TB of disk space. It thus represents a simulation scope that is unprecedented in nuclear medicine imaging research. The set of digital phantoms, the simulation methods themselves, and the database of simulated MPS projections provide tools and methods needed to expand the applications of realistic simulation in the optimization and evaluation of nuclear medicine and SPECT imaging as has been shown in Chapters 4 to 7.

Second, the application of the IO to optimize instrumentation and acquisition protocols is theoretically appealing. For example, for a binary detection task, it requires computation of the requisite likelihood functions under the hypotheses that the image contains or does not contain a perfusion defect. However, it has rarely been rigorously applied to real imaging tasks including realistic background variability, as the ones used in this work, due to the technical difficulty of estimating the IO test statistic, i.e. the likelihood ratio. In this work, we extended and modified methods based on MCMC techniques [33, 111] to estimate the likelihood ratio for both binary detection and joint detection and localization tasks using realistic background variability in the context of single and dual isotope MPS. This involved numerical and methodological refinement of the MCMC IO estimation procedure. These enhancements included casting it in terms of linear algebra operations in order to speed it up and improve its numerical performance. We have also made use of the fact the IO performance is not altered under linear operations by scaling the input projection, background and signal images required for computing the likelihood ratio. Appropriate scaling was used to improve the numerical performance and avoiding numerical over or under flow errors that can occur when computing the likelihood ratio. Without these enhancements the likelihood ratio estimates were unreliable.

Finally, a major innovation in this dissertation was the development of the IO-MM. As previously mentioned, the IO implicitly has perfect knowledge about the image formation process relating the imaged object to the projection data. Thus using the IO to optimize imaging systems could lead to differences in optimal parameters compared to those optimized for humans interpreting SPECT images that are reconstructed with imperfect or no compensation. The IO-MM is a model observer that allows incorporating imperfect system models into the IO optimization process. Our results in Chapter 5 and Chapter 6 indicated that the IO-MM had good agreement with the CHO, as a surrogate for human observer, in terms of the range of optimal Tc-99m acquisition energy window widths, optimal collimators and the ranking of scatter and CDR compensation methods. This is potentially important and suggests that the IO-MM may be useful for optimization of instrumentation and acquisition due to its substantially reduced computational burden compared to the CHO and its ability to incorporate the effects of model mismatch.

8.3 Future work

Results of this dissertation suggest several possible future research directions such as parameters that have not yet been fully optimized or hypotheses generated by this work.

8.3.1 Optimization of SPECT using variable acquisition duration

It is well known that different projection views contain different amounts and quality of information for most nuclear medicine studies. For example, in myocardial perfusion SPECT imaging, 180° projection arcs are used by many sites, because data from the posterior views have few counts from the heart and a high scatter-to-primary ratio. In whole body bone scanning anterior and posterior views are collected because they provide better visualization of high uptake regions in anterior and posterior regions of the body, respectively. This observation suggests another parameter that can be optimized is the acquisition duration for each projection view. We have preliminary results that suggest that there is a great deal of difference in the amount of information about the presence or absence of myocardial perfusion defects in the various projection views, as measured by IO performance. Using a somewhat ad hoc optimization scheme to select the optimal acquisition time per view for a given total projection time, we demonstrated an increase in performance for the IO. An abstract based on this work has been presented at the Society of Nuclear Medicine and Molecular Imaging (SNMMI) 2011 annual meeting [144].

8.3.2 Investigating the effect of improved energy resolution on image quality

Another way to decrease the amount of scatter in the projection data is to improve the energy resolution of the detector, but this requires the use of different detector materials such as a semiconductor detector Cd(Zn)Te (CZT) or a scintillator with high light output such as $LaBr_3$. Such materials are either not widely available or are substantially more expensive than NaI(Tl). The flexible design of the projection database in [1] allows us to generate projection images for any arbitrary energy window and energy resolution. In a preliminary study [3], we compared the performance of a detector with perfect energy resolution, current NaI(Tl) detectors and a CZT detector with realistic modeling of the energy-dependent energy resolution function. The comparison was made using the same observers and data used for the other work in this dissertation, i.e. the Ideal Observer and the Ideal Observer with Model Mismatch when no scatter model was included. Results suggested that IO performance when using CZT detectors was better than that for NaI for narrow energy windows, but they had similar optimal windows, and CZT had no performance advantage over NaI with optimal windows. However, in that study, we used one phantom that modeled a male patient with a medium sized body, heart and subcutaneous adipose tissue levels. It would be interesting to see if this result holds when using the entire phantom population.

8.3.3 Explore decision theoretic implications of the Ideal Observer with model mismatch

The IO-MM provides an efficient and powerful tool for system, acquisition parameter and reconstruction/compensation optimization in the projection domain. However, at present it is a practical approach to incorporating model mismatch into the IO framework, but it is unclear in what sense it is the optimal observer. It would be interesting to study the decision theoretic implications of the IO-MM and its relation with the IO. It would be also of interest to study the cases where the IO and IO-MM performances do not match and the relation to measures of the distance between the true and the approximate models used by the IO and IO-MM, respectively.

REFERENCES

[1] M. Ghaly, Y. Du, G. S. Fung, B. M. Tsui, J. M. Links, and E. Frey, "Design of a digital phantom population for myocardial perfusion SPECT imaging research," *Phys Med Biol,* vol. 59, pp. 2935-53, Jun 21 2014.

[2] M. Ghaly, J. Links, and E. Frey, "Comparison of scatter compensation methods using the ideal observer with model mismatch," *Society of Nuclear Medicine Annual Meeting Abstracts,* vol. 54, p. 266, 2013.

[3] M. Ghaly, J. Links, Y. Du, and E. Frey, "Importance of including model mismatch in ideal observer-based acquisition parameter optimization in SPECT," *Society of Nuclear Medicine Annual Meeting Abstracts,* vol. 53, p. 326, 2012.

[4] M. Ghaly, J. M. Links, Y. Du, and E. C. Frey, "Model mismatch and the ideal observer in SPECT," in *SPIE Medical Imaging*, 2013, pp. 86730K-86730K-9.

[5] M. Ghaly and E. Frey, "Optimization of energy windows and injected activities for dual-isotope simultaneous-acquisition (DISA) myocardial perfusion SPECT using ideal observer (IO) and realistic background variations," *Society of Nuclear Medicine Annual Meeting Abstracts,* vol. 52, p. 2014, 2011.

[6] S. L. Murphy, J. Xu, and K. D. Kochanek, "Deaths: final data for 2010," *Natl Vital Stat Rep,* vol. 61, pp. 1-117, May 8 2013.

[7] G. A. Beller and S. R. Bergmann, "Myocardial perfusion imaging agents: SPECT and PET," *Journal of nuclear cardiology,* vol. 11, pp. 71-86, 2004.

[8] E. S. Crawford and S. S. Husain, *Nuclear cardiac imaging: terminology and technical aspects*: Snmmi, 2010.

[9] P. Kailasnath and A. J. Sinusas, "Comparison of Tl-201 with Tc-99m–labeled myocardial perfusion agents: technical, physiologic, and clinical issues," *Journal of Nuclear Cardiology,* vol. 8, pp. 482-498, 2001.

[10] M. J. Henzlova, M. D. Cerqueira, J. J. Mahmarian, S. S. Yao, and C. Quality Assurance Committee of the American Society of Nuclear, "Stress protocols and tracers," *J Nucl Cardiol,* vol. 13, pp. e80-90, Nov 2006.

[11] E. G. DePuey and E. V. Garcia, "Updated imaging guidelines for nuclear cardiology procedures," *J Nucl Cardiol,* vol. 8, pp. G1-G58, 2001.

[12] S. R. Cherry, J. A. Sorenson, and M. E. Phelps, *Physics in nuclear medicine*: Elsevier Health Sciences, 2012.

[13] J. L. Prince and J. M. Links, *Medical imaging signals and systems*: Pearson Prentice Hall Upper Saddle River, NJ, 2006.

[14] H. M. Deloar, H. Watabe, K. M. Kim, T. Aoi, E. Kunieda, H. Fujii*, et al.*, "Optimization of the width of the photopeak energy window in the TDCS technique for scatter correction in quantitative SPECT," *Ieee Transactions on Nuclear Science,* vol. 51, pp. 625-630, Jun 2004.

[15] F. J. Beekman, H. W. A. M. de Jong, and E. T. P. Slijpen, "Efficient SPECT scatter calculation in non-uniform media using correlated Monte Carlo simulation," *Physics in Medicine and Biology,* vol. 44, pp. N183-N192, Aug 1999.

[16] J. B. Xiao, T. C. de Wit, W. Zbijewski, S. G. Staelens, and F. J. Beekman, "Evaluation of 3D Monte Carlo-based scatter correction for Tl-201 cardiac perfusion SPECT," *Journal of Nuclear Medicine,* vol. 48, pp. 637-644, Apr 2007.

[17] J. B. Xiao, T. C. de Wit, S. G. Staelens, and F. J. Beekman, "Evaluation of 3D Monte Carlo-based scatter correction for Tc-99m cardiac perfusion SPECT," *Journal of Nuclear Medicine,* vol. 47, pp. 1662-1669, Oct 2006.

[18] A. Kojima, A. Takaki, T. Noguchi, M. Matsumoto, N. Katsuda, S. Tomiguchi*, et al.*, "Optimum energy window setting on Hg-201 x-rays photopeak for effective T1-201 imaging," *Annals of Nuclear Medicine,* vol. 19, pp. 541-547, Oct 2005.

[19] E. C. Frey and B. M. W. Tsui, "A new method for modeling the spatially-variant, object-dependent scatter response function in SPECT," *1996 Ieee Nuclear Science Symposium - Conference Record, Vols 1-3,* pp. 1082-1086, 1997.

[20] F. J. Beekman, C. Kamphuis, and E. C. Frey, "Scatter compensation methods in 3D iterative SPECT reconstruction: A simulation study," *Physics in Medicine and Biology,* vol. 42, pp. 1619-1632, Aug 1997.

[21] B. M. W. Tsui, E. C. Frey, X. Zhao, D. S. Lalush, R. E. Johnston, and W. H. Mccartney, "The Importance and Implementation of Accurate 3d Compensation Methods for Quantitative Spect," *Physics in Medicine and Biology,* vol. 39, pp. 509-530, Mar 1994.

[22] P. H. Pretorius, M. A. King, T. S. Pan, D. J. de Vries, S. J. Glick, and C. L. Byrne, "Reducing the influence of the partial volume effect on SPECT activity quantitation with 3D modelling of spatial resolution in iterative reconstruction," *Physics in Medicine and Biology,* vol. 43, pp. 407-420, Feb 1998.

[23] X. Song, W. P. Segars, Y. Du, B. M. Tsui, and E. C. Frey, "Fast modelling of the collimator-detector response in Monte Carlo simulation of SPECT imaging using the angular response function," *Phys Med Biol,* vol. 50, pp. 1791-804, Apr 21 2005.

[24] H. H. Barrett and K. J. Myers, "Foundations of image science," *Foundations of Image Science, by Harrison H. Barrett, Kyle J. Myers, pp. 1584. ISBN 0-471-15300-1. Wiley-VCH, October 2003.,* vol. 1, 2003.

[25] L. A. Shepp and Y. Vardi, "Maximum likelihood reconstruction for emission tomography," *Medical Imaging, IEEE Transactions on,* vol. 1, pp. 113-122, 1982.

[26] K. Lange and R. Carson, "EM reconstruction algorithms for emission and transmission tomography," *Journal of computer assisted tomography,* vol. 8, pp. 306-316, 1984.

[27] H. M. Hudson and R. S. Larkin, "Accelerated image reconstruction using ordered subsets of projection data," *Medical Imaging, IEEE Transactions on,* vol. 13, pp. 601-609, 1994.

[28] D. S. Lalush and B. M. W. Tsui, "Performance of ordered-subset reconstruction algorithms under conditions of extreme attenuation and truncation in myocardial SPECT," *Journal of Nuclear Medicine,* vol. 41, pp. 737-744, Apr 2000.

[29] J. C. Dainty, R. Shaw, and L. Cutrona, "Image science: principles, analysis and evaluation of photographic-type imaging processes," *Physics Today,* vol. 29, p. 71, 1976.

[30] R. F. Wagner and D. G. Brown, "Overview of a Unified SNR Analysis of Medical Imaging Systems," *IEEE Trans Med Imaging,* vol. 1, pp. 210-3, 1982.

[31] J. P. Rolland and H. H. Barrett, "Effect of Random Background Inhomogeneity on Observer Detection Performance," *Journal of the Optical Society of America a-Optics Image Science and Vision,* vol. 9, pp. 649-658, May 1992.

[32] M. A. Kupinski, E. Clarkson, J. W. Hoppin, L. Chen, and H. H. Barrett, "Experimental determination of object statistics from noisy images," *J Opt Soc Am A Opt Image Sci Vis,* vol. 20, pp. 421-9, Mar 2003.

[33] M. A. Kupinski, J. W. Hoppin, E. Clarkson, and H. H. Barrett, "Ideal-observer computation in medical imaging with use of Markov-chain Monte Carlo techniques,"

Journal of the Optical Society of America a-Optics Image Science and Vision, vol. 20, pp. 430-438, Mar 2003.

[34] S. Park, M. A. Kupinski, E. Clarkson, and H. H. Barrett, "Ideal-observer performance under signal and background uncertainty," *Information Processing in Medical Imaging, Proceedings,* vol. 2732, pp. 342-353, 2003.

[35] W. P. Segars, G. Sturgeon, S. Mendonca, J. Grimes, and B. M. Tsui, "4D XCAT phantom for multimodality imaging research," *Med Phys,* vol. 37, pp. 4902-15, Sep 2010.

[36] C. E. Metz and J. H. Shen, "Gains in Accuracy from Replicated Readings of Diagnostic Images - Prediction and Assessment in Terms of Roc Analysis," *Medical Decision Making,* vol. 12, pp. 60-75, Jan-Mar 1992.

[37] P. Khurd and G. Gindi, "Decision strategies that maximize the area under the LROC curve," *Ieee Transactions on Medical Imaging,* vol. 24, pp. 1626-1636, Dec 2005.

[38] L. L. Zhou and G. Gindi, "Collimator optimization in SPECT based on a joint detection and localization task," *Physics in Medicine and Biology,* vol. 54, pp. 4423-4437, Jul 21 2009.

[39] K. Gross, M. A. Kupinski, and J. Y. Hesterman, "A fast model of a multiple-pinhole SPECT imaging system," *Medical Imaging 2005: Image Perception, Observer Performance, and Technology Assessment,* vol. 5749, pp. 118-127, 2005.

[40] K. Gross, M. A. Kupinski, T. Peterson, and E. Clarkson, "Optimizing a multiple-pinhole SPECT system using the ideal observer," *Medical Imaging 2003: Image Perception, Observer Performance, and Technology Assessment,* vol. 5034, pp. 314-322, 2003.

[41] X. He, B. S. Caffo, and E. C. Frey, "Toward realistic and practical ideal observer (IO) estimation for the optimization of medical imaging systems," *IEEE Trans Med Imaging,* vol. 27, pp. 1535-43, Oct 2008.

[42] K. Fukunaga, *Introduction to statistical pattern recognition*: Academic press, 1990.

[43] K. J. Myers and H. H. Barrett, "Addition of a Channel Mechanism to the Ideal-Observer Model," *Journal of the Optical Society of America a-Optics Image Science and Vision,* vol. 4, pp. 2447-2457, Dec 1987.

[44] S. D. Wollenweber, B. M. W. Tsui, D. S. Lalush, E. C. Frey, K. J. LaCroix, and G. T. Gullberg, "Comparison of hotelling observer models and human observers in defect detection from myocardial SPECT imaging," *Ieee Transactions on Nuclear Science,* vol. 46, pp. 2098-2103, Dec 1999.

[45] H. C. Gifford, M. A. King, D. J. de Vries, and E. J. Soares, "Channelized hotelling and human observer correlation for lesion detection in hepatic SPECT imaging," *Journal of Nuclear Medicine,* vol. 41, pp. 514-521, Mar 2000.

[46] E. C. Frey, K. L. Gilland, and B. M. W. Tsui, "Application of task-based measures of image quality to optimization and evaluation of three-dimensional reconstruction-based compensation methods in myocardial perfusion SPECT," *IEEE Transactions on Medical Imaging,* vol. 21, pp. 1040-1050, Sep 2002.

[47] X. He, E. C. Frey, J. M. Links, K. L. Gilland, W. P. Segars, and B. M. W. Tsui, "A mathematical observer study for the evaluation and optimization of compensation methods for myocardial SPECT using a phantom population that realistically models patient variability," *Ieee Transactions on Nuclear Science,* vol. 51, pp. 218-224, Feb 2004.

[48] J. Oldan, S. Kulkarni, Y. X. Xing, P. Khurd, and G. Gindi, "Channelized hotelling and human observer study of optimal smoothing in SPECT MAP reconstruction," *Ieee Transactions on Nuclear Science,* vol. 51, pp. 733-741, Jun 2004.

[49] K. L. Gilland, B. M. W. Tsui, Y. J. Qi, and G. T. Gullberg, "Comparison of channelized hotelling and human observers in determining optimum OS-EM reconstruction parameters for myocardial SPECT," *Ieee Transactions on Nuclear Science,* vol. 53, pp. 1200-1204, Jun 2006.

[50] H. C. Gifford, M. A. King, P. H. Pretorius, and R. G. Wells, "A comparison of human and model observers in multislice LROC studies," *Ieee Transactions on Medical Imaging,* vol. 24, pp. 160-169, Feb 2005.

[51] J. Yao and H. H. Barrett, "Predicting Human-Performance by a Channelized Hotelling Observer Model," *Mathematical Methods in Medical Imaging,* vol. 1768, pp. 161-168, 1992.

[52] T. H. Farncombe, H. C. Gifford, M. V. Narayanan, P. H. Pretorius, E. C. Frey, and M. A. King, "Assessment of scatter compensation strategies for Ga-67 SPECT using numerical observers and human LROC studies," *Journal of Nuclear Medicine,* vol. 45, pp. 802-812, May 2004.

[53] R. G. Swensson, "Unified measurement of observer performance in detecting and localizing target objects on images," *Medical Physics,* vol. 23, pp. 1709-1725, Oct 1996.

[54] K. J. LaCroix, B. M. Tsui, E. C. Frey, and R. J. Jaszczak, "Receiver operating characteristic evaluation of iterative reconstruction with attenuation correction in 99mTc-sestamibi myocardial SPECT images," *Journal of nuclear medicine: official publication, Society of Nuclear Medicine,* vol. 41, pp. 502-513, 2000.

[55] W. P. Segars, B. M. Tsui, D. S. Lalush, E. C. Frey, M. A. King, and D. Manocha, "Development and application of the new dynamic Nurbs-based Cardiac-Torso (NCAT) phantom.," *Journal of Nuclear Medicine,* vol. 42, pp. 7p-7p, May 2001.

[56] W. P. Segars and B. M. W. Tsui, "Study of the efficacy of respiratory gating in myocardial SPECT using the new 4-D NCAT phantom," *Nuclear Science, IEEE Transactions on,* vol. 49, pp. 675-679, 2002.

[57] T. Funk, D. L. Kirch, J. E. Koss, E. Botvinick, and B. H. Hasegawa, "A novel approach to multipinhole SPECT for myocardial perfusion imaging," *Journal of Nuclear Medicine,* vol. 47, pp. 595-602, 2006.

[58] W. P. Segars and B. M. W. Tsui, "MCAT to XCAT: The Evolution of 4-D Computerized Phantoms for Imaging Research," *Proceedings of the Ieee,* vol. 97, pp. 1954-1968, Dec 2009.

[59] G. S. Fung, W. P. Segars, T.-S. Lee, T. Higuchi, A. I. Veress, G. T. Gullberg*, et al.*, "Realistic simulation of regional myocardial perfusion defects for cardiac SPECT studies," in *Nuclear Science Symposium Conference Record (NSS/MIC), 2010 IEEE*, 2010, pp. 3061-3064.

[60] A. Barclay, R. Eisner, and E. DiBella, "PET thorax model database," ed, 2005.

[61] T. K. Lewellen, R. L. Harrison, and S. Vannoy, "The simset program," ed: Bristol: Institute of Physics Publishing, 1998, pp. 77-92.

[62] Y. Du, E. C. Frey, W. T. Wang, C. Tocharoenchai, W. H. Baird, and B. M. W. Tsui, "Combination of MCNP and SimSET for Monte Carlo simulation of SPECT with medium- and high-energy photons," *Ieee Transactions on Nuclear Science,* vol. 49, pp. 668-674, Jun 2002.

[63] W. T. Wang, E. C. Frey, B. M. W. Tsui, C. Tocharoenchai, and W. H. Baird, "Parameterization of Pb X-ray contamination in simultaneous Tl-201 and Tc-99m dual-isotope imaging," *Ieee Transactions on Nuclear Science,* vol. 49, pp. 680-692, Jun 2002.

[64] B. He, Y. Du, X. Y. Song, W. P. Segars, and E. C. Frey, "A Monte Carlo and physical phantom evaluation of quantitative In-111SPECT," *Physics in Medicine and Biology,* vol. 50, pp. 4169-4185, Sep 7 2005.

[65] N. Song, Y. Du, B. He, and E. C. Frey, "Development and evaluation of a model-based downscatter compensation method for quantitative I-131 SPECT," *Medical Physics,* vol. 38, pp. 3193-3204, Jun 2011.

[66] X. He, J. M. Links, and E. C. Frey, "An investigation of the trade-off between the count level and image quality in myocardial perfusion SPECT using simulated images: the effects of statistical noise and object variability on defect detectability," *Physics in Medicine and Biology,* vol. 55, pp. 4949-4961, Sep 7 2010.

[67] R. J. LeClair, Y. Wang, P. Zhao, M. Boileau, L. Wang, and F. Fleurot, "An analytic model for the response of a CZT detector in diagnostic energy dispersive x-ray spectroscopy," *Med Phys,* vol. 33, pp. 1329-37, May 2006.

[68] G. F. Knoll, *Radiation detection and measurement*, 4th ed. Hoboken, N.J.: John Wiley, 2010.

[69] S. R. Cherry, J. A. Sorenson, and M. E. Phelps, *Physics in nuclear medicine*, 4th ed. Philadelphia: Elsevier/Saunders, 2012.

[70] X. Song, E. C. Frey, W. T. Wang, Y. Du, and B. M. W. Tsui, "Validation and evaluation of model-based crosstalk compensation method in simultaneous Tc-99m stress and Tl-201 rest myocardial perfusion SPECT," *Ieee Transactions on Nuclear Science,* vol. 51, pp. 72-79, Feb 2004.

[71] X. Rong, Y. Du, M. Ljungberg, E. Rault, S. Vandenberghe, and E. C. Frey, "Development and evaluation of an improved quantitative (90)Y bremsstrahlung SPECT method," *Med Phys,* vol. 39, pp. 2346-58, May 2012.

[72] E. L. Keller, "Optimum Dimensions of Parallel-Hole Multi-Aperture Collimators for Gamma-Ray Cameras," *Journal of Nuclear Medicine,* vol. 9, pp. 233-&, 1968.

[73] S. Swann, D. Palmer, L. Kaufman, C. B. Lim, and P. B. Hoffer, "Optimized Collimators for Scintillation Cameras," *Journal of Nuclear Medicine,* vol. 17, pp. 50-53, 1976.

[74] R. N. Beck and L. D. Redtung, "Collimator Design Using Ray-Tracing Techniques," *Ieee Transactions on Nuclear Science,* vol. 32, pp. 865-869, 1985.

[75] Y. H. Lau, B. F. Hutton, and F. J. Beekman, "Choice of collimator for cardiac SPET when resolution compensation is included in iterative reconstruction," *European Journal of Nuclear Medicine,* vol. 28, pp. 39-47, Jan 2001.

[76] Y. Inoue, I. Shirouzu, T. Machida, Y. Yoshizawa, F. Akita, M. Minami*, et al.*, "Collimator choice in cardiac SPECT with I-123-labeled tracers," *Journal of Nuclear Cardiology,* vol. 11, pp. 433-439, Jul-Aug 2004.

[77] S. C. Moore, M. F. Kijewski, and G. El Fakhri, "Collimator optimization for detection and quantitation tasks: Application to gallium-67 imaging," *Ieee Transactions on Medical Imaging,* vol. 24, pp. 1347-1356, Oct 2005.

[78] S. J. McQuaid, S. Southekal, M. F. Kijewski, and S. C. Moore, "Joint optimization of collimator and reconstruction parameters in SPECT imaging for lesion quantification," *Phys Med Biol,* vol. 56, pp. 6983-7000, Nov 7 2011.

[79] B. M. W. Tsui, "Correction to a Comparison of Optimum Detector Spatial-Resolution in Nuclear Imaging Based on Statistical-Theory and Observer Performance," *Physics in Medicine and Biology,* vol. 23, pp. 1203-1205, 1978.

[80] B. M. W. Tsui, C. E. Metz, and R. N. Beck, "Optimum Detector Spatial-Resolution for Discriminating between Tumor Uptake Distributions in Scintigraphy," *Physics in Medicine and Biology,* vol. 28, pp. 775-788, 1983.

[81] K. J. Myers, J. P. Rolland, H. H. Barrett, and R. F. Wagner, "Aperture Optimization for Emission Imaging - Effect of a Spatially Varying Background," *Journal of the Optical Society of America a-Optics Image Science and Vision,* vol. 7, pp. 1279-1293, Jul 1990.

[82] S. C. Moore, D. J. Devries, B. Nandram, M. F. Kijewski, and S. P. Mueller, "Collimator Optimization for Lesion Detection Incorporating Prior Information About Lesion Size," *Medical Physics,* vol. 22, pp. 703-713, Jun 1995.

[83] M. V. Narayanan, H. C. Gifford, M. A. King, P. H. Pretorius, T. H. Farncombe, P. Bruyant*, et al.*, "Optimization of iterative reconstructions of Tc-99m cardiac SPECT studies using numerical observers.," *2001 Ieee Nuclear Science Symposium, Conference Records, Vols 1-4,* pp. 2156-2160, 2002.

[84] G. S. L. Zeng and G. T. Gullberg, "A channelized-hotelling-trace collimator design method based on reconstruction rather than projections," *Ieee Transactions on Nuclear Science,* vol. 49, pp. 2155-2158, Oct 2002.

[85] B. Zhang and G. L. Zeng, "High-Resolution Versus High-Sensitivity SPECT Imaging With Geometric Blurring Compensation for Various Parallel-Hole Collimation Geometries," *Ieee Transactions on Information Technology in Biomedicine,* vol. 14, pp. 1121-1127, Jul 2010.

[86] H. H. Barrett, J. Yao, J. P. Rolland, and K. J. Myers, "Model Observers for Assessment of Image Quality," *Proceedings of the National Academy of Sciences of the United States of America,* vol. 90, pp. 9758-9765, Nov 1 1993.

[87] C. E. Metz, "Basic principles of ROC analysis," *Semin Nucl Med,* vol. 8, pp. 283-98, Oct 1978.

[88] H. C. Gifford, "A visual-search model observer for multislice-multiview SPECT images," *Med Phys,* vol. 40, p. 092505, Sep 2013.

[89] C. K. Abbey and H. H. Barrett, "Human- and model-observer performance in ramp-spectrum noise: effects of regularization and object variability," *Journal of the Optical Society of America a-Optics Image Science and Vision,* vol. 18, pp. 473-488, Mar 2001.

[90] H. C. Gifford, "Efficient visual-search model observers for PET," *Br J Radiol,* vol. 87, p. 20140017, Jul 2014.

[91] R. F. Wagner, D. G. Brown, and C. E. Metz, "On the multiplex advantage of coded source/aperture photon imaging," in *Conference on Digital Rdiography*, 1981, pp. 72-76.

[92] K. J. Myers, R. F. Wagner, D. G. Brown, and H. H. Barrett, "Efficient utilization of aperture and detector by optimal coding," in *1989 Medical Imaging*, 1989, pp. 164-175.

[93] H. H. Barrett and C. K. Abbey, "Bayesian detection of random signals on random backgrounds," *Information Processing in Medical Imaging,* vol. 1230, pp. 155-166, 1997.

[94] S. Park, E. Clarkson, M. A. Kupinski, and H. H. Barrett, "Efficiency of the human observer detecting random signals in random backgrounds," *Journal of the Optical Society of America a-Optics Image Science and Vision,* vol. 22, pp. 3-16, Jan 2005.

[95] L. Zhou, P. Khurd, S. Kulkarni, A. Rangarajan, and G. Gindi, "Aperture optimization in emission imaging using ideal observers for joint detection and localization," *Physics in Medicine and Biology,* vol. 53, pp. 2019-2034, Apr 21 2008.

[96] A. B. Barclay, R. L. Eisner, and E. V. DiBella. *PET thorax model database*. Available: http://www.emory.edu/CRL/abb/thoraxmodel/Contents.html

[97] M. D. Cerqueira, K. C. Allman, E. P. Ficaro, C. L. Hansen, K. J. Nichols, R. C. Thompson*, et al.*, "Recommendations for reducing radiation exposure in myocardial perfusion imaging," *Journal of nuclear cardiology,* vol. 17, pp. 709-718, 2010.

[98] J. Albert, "Bayesian Computation with R, Second Edition," *Bayesian Computation with R, Second Edition,* pp. 1-298, 2009.

[99] C. E. Metz, B. A. Herman, and C. A. Roe, "Statistical comparison of two ROC-curve estimates obtained from partially-paired datasets," *Medical Decision Making,* vol. 18, pp. 110-121, 1998.

[100] L. Zhou, B. Liu, and G. Gindi, "System and reconstruction optimization in SPECT using model observers for different tasks," in *Nuclear Science Symposium Conference Record (NSS/MIC), 2010 IEEE*, 2010, pp. 3581-3583.

[101] M. D. Cerqueira, N. J. Weissman, V. Dilsizian, A. K. Jacobs, S. Kaul, W. K. Laskey*, et al.*, "Standardized myocardial segmentation and nomenclature for tomographic imaging of the heart a statement for healthcare professionals from the cardiac imaging committee of the Council on Clinical Cardiology of the American Heart Association," *Circulation,* vol. 105, pp. 539-542, 2002.

[102] X. He, E. C. Frey, J. M. Links, X. Song, and B. M. W. Tsui, "Comparison of penetration and scatter effects on defect contrast for GE and siemens LEHR collimators in myocardial perfusion SPECT - A simulation study," *IEEE Transactions on Nuclear Science,* vol. 52, pp. 1359-1364, Oct 2005.

[103] L. Zhou, S. Kulkarni, B. Liu, and G. Gindi, "Strategies to jointly optimize SPECT collimator and reconstruction parameters for a detection task," in *Biomedical Imaging: From Nano to Macro, 2009. ISBI'09. IEEE International Symposium on*, 2009, pp. 394-397.

[104] E. Frey and B. Tsui, "Collimator-detector response compensation in SPECT," in *Quantitative analysis in nuclear medicine imaging*, ed: Springer, 2006, pp. 141-166.

[105] G. L. Zeng and G. T. Gullberg, "Frequency-Domain Implementation of the 3-Dimensional Geometric Point Response Correction in Spect Imaging," *Ieee Transactions on Nuclear Science,* vol. 39, pp. 1444-1453, Oct 1992.

[106] C. E. Metz, F. B. Atkins, and R. N. Beck, "The Geometric Transfer-Function Component for Scintillation Camera Collimators with Straight Parallel Holes," *Physics in Medicine and Biology,* vol. 25, pp. 1059-1070, 1980.

[107] B. M. Tsui, H.-B. Hu, D. R. Gilland, and G. T. Gullberg, "Implementation of simultaneous attenuation and detector response correction in SPECT," *Nuclear Science, IEEE Transactions on,* vol. 35, pp. 778-783, 1988.

[108] P. H. Pretorius, M. A. King, T. S. Pan, D. J. de Vries, S. J. Glick, and C. L. Byrne, "Reducing the influence of the partial volume effect on SPECT activity quantitation with 3D modelling of spatial resolution in iterative reconstruction," *Phys Med Biol,* vol. 43, pp. 407-20, Feb 1998.

[109] H. C. Gifford, M. A. King, R. G. Wells, W. G. Hawkins, M. V. Narayanan, and P. H. Pretorius, "LROC analysis of detector-response compensation in SPECT," *Ieee Transactions on Medical Imaging,* vol. 19, pp. 463-473, May 2000.

[110] X. Rong, M. Ghaly, and E. C. Frey, "Optimization of energy window for 90Y bremsstrahlung SPECT imaging for detection tasks using the ideal observer with model-mismatch," *Med Phys,* vol. 40, p. 062502, Jun 2013.

[111] X. He, B. S. Caffo, and E. C. Frey, "Toward realistic and practical ideal observer (IO) estimation for the optimization of medical imaging systems," *Ieee Transactions on Medical Imaging,* vol. 27, pp. 1535-1543, Oct 2008.

[112] S. Sankaran, E. C. Frey, K. L. Gilland, and B. M. Tsui, "Optimum compensation method and filter cutoff frequency in myocardial SPECT: a human observer study," *J Nucl Med,* vol. 43, pp. 432-8, Mar 2002.

[113] I. Buvat, M. C. De Sousa, M. Di Paola, M. Ricard, J. Lumbroso, and B. Aubert, "Impact of scatter correction in planar scintimammography: a phantom study," *J Nucl Med,* vol. 39, pp. 1590-6, Sep 1998.

[114] E. Frey and B. Tsui, "A practical method for incorporating scatter in a projector-backprojector for accurate scatter compensation in SPECT," *Nuclear Science, IEEE Transactions on,* vol. 40, pp. 1107-1116, 1993.

[115] R. J. Jaszczak, K. L. Greer, C. E. Floyd, C. C. Harris, and R. E. Coleman, "Improved Spect Quantification Using Compensation for Scattered Photons," *Journal of Nuclear Medicine,* vol. 25, pp. 893-900, 1984.

[116] K. Ogawa, Y. Harata, T. Ichihara, A. Kubo, and S. Hashimoto, "A practical method for position-dependent Compton-scatter correction in single photon emission CT," *IEEE Trans Med Imaging,* vol. 10, pp. 408-12, 1991.

[117] D. R. Haynor, M. S. Kaplan, R. S. Miyaoka, and T. K. Lewellen, "Multiwindow scatter correction techniques in single-photon imaging," *Med Phys,* vol. 22, pp. 2015-24, Dec 1995.

[118] E. C. Frey, B. M. W. Tsui, and D. J. Kadrmas, "A new method for modeling the spatially-variant, object-dependent scatter response function in SPECT," presented at the IEEE Nuclear Science Symposium Conference Record, Anaheim, CA, IEEE Nuclear Science Symposium Conference Record, Anaheim, CA, 1996.

[119] Y. Du, B. M. Tsui, and E. C. Frey, "Model-based compensation for quantitative 123I brain SPECT imaging," *Phys Med Biol,* vol. 51, pp. 1269-82, Mar 7 2006.

[120] D. J. Kadrmas, E. C. Frey, and B. M. Tsui, "Simultaneous technetium-99m/thallium-201 SPECT imaging with model-based compensation for cross-contaminating effects," *Phys Med Biol,* vol. 44, pp. 1843-60, Jul 1999.

[121] M. V. Narayanan, P. H. Pretorius, S. T. Dahlberg, J. A. Leppo, N. Botkin, J. Krasnow*, et al.*, "Evaluation of scatter compensation strategies and their impact on human detection performance Tc-99m myocardial perfusion imaging," *Ieee Transactions on Nuclear Science,* vol. 50, pp. 1522-1527, Oct 2003.

[122] E. C. Frey, B. M. W. Tsui, and J. R. Perry, "Simultaneous Acquisition of Emission and Transmission Data for Improved Tl-201 Cardiac Spect Imaging Using a Tc-99m Transmission Source," *Journal of Nuclear Medicine,* vol. 33, pp. 2238-2245, Dec 1992.

[123] M. Nakamura, K. Takeda, T. Ichihara, N. Motomura, H. Shimizu, Y. Saito*, et al.*, "Feasibility of simultaneous stress Tc-99m-sestamibi/rest (201)T1 dual-isotope myocardial perfusion SPECT in the detection of coronary artery disease," *Journal of Nuclear Medicine,* vol. 40, pp. 895-903, Jun 1999.

[124] M. Fukushima, Y. Seino, S. Kumita, H. Nakajo, K. Cho, and T. Takano, "Dual-isotope myocardial SPECT in patients with redefined myocardial infarction," *International Journal of Cardiology,* vol. 104, pp. 204-212, Sep 30 2005.

[125] H. Ando, T. Fukuyama, W. Mitsuoka, S. Egashira, Y. Imamura, H. Masaki*, et al.*, "Influence of downscatter in simultaneously acquired thallium-201/technetium-99m-PYP SPECT," *Journal of Nuclear Medicine,* vol. 37, pp. 781-785, May 1996.

[126] H. Kiat, G. Germano, J. Friedman, K. Van Train, G. Silagan, F. P. Wang*, et al.*, "Comparative feasibility of separate or simultaneous rest thallium-201/stress technetium-99m-sestamibi dual-isotope myocardial perfusion SPECT," *J Nucl Med,* vol. 35, pp. 542-8, Apr 1994.

[127] V. J. Lowe, K. L. Greer, M. W. Hanson, R. J. Jaszczak, and R. E. Coleman, "Cardiac phantom evaluation of simultaneously acquired dual-isotope rest thallium-201/stress technetium-99m SPECT images," *J Nucl Med,* vol. 34, pp. 1998-2006, Nov 1993.

[128] K. Knesaurek, "A new dual-isotope convolution cross-talk correction method: a Tl-201/Tc-99m SPECT cardiac phantom study," *Med Phys,* vol. 21, pp. 1577-83, Oct 1994.

[129] D. J. Kadrmas, E. C. Frey, J. A. Ziffer, and B. M. W. Tsui, "Iterative reconstruction of simultaneously acquired Tc-99m Sestamibi Tl-201 cardiac SPECT data with compensation for cross-contaminating effects.," *Journal of Nuclear Medicine,* vol. 38, pp. 327-327, May 1997.

[130] H. W. A. M. de Jong, W. T. Wang, E. C. Frey, M. A. Viergever, and F. J. Beekman, "Efficient simulation of SPECT down-scatter including photon interactions with crystal and lead," *Medical Physics,* vol. 29, pp. 550-560, Apr 2002.

[131] H. W. A. M. de Jong, F. J. Beekman, M. A. Viergever, and P. P. van Rijk, "Simultaneous Tc-99m/Tl-201 dual-isotope SPET with Monte Carlo-based down-scatter correction," *European Journal of Nuclear Medicine and Molecular Imaging,* vol. 29, pp. 1063-1071, Aug 2002.

[132] T. Kangasmaa, J. Kuikka, and A. Sohlberg, "Optimisation of simultaneous tl-201/tc-99m dual isotope reconstruction with monte-carlo-based scatter correction," *Int J Mol Imaging,* vol. 2012, p. 695632, 2012.

[133] S. C. Moore, R. J. English, C. Syravanh, D. E. Tow, R. E. Zimmerman, K. H. Chan*, et al.*, "Simultaneous Tc-99m/Tl-201 Imaging Using Energy-Based Estimation of the Spatial Distributions of Contaminant Photons," *Ieee Transactions on Nuclear Science,* vol. 42, pp. 1189-1195, Aug 1995.

[134] D. C. YANG, E. RAGASA, L. GOULD, M. HUANG, C. Reddy, B. SAUL*, et al.*, "Radionuclide simultaneous dual-isotope stress myocardial perfusion study using the" three window technique," *Clinical nuclear medicine,* vol. 18, pp. 852-857, 1993.

[135] K. Kacperski, K. Erlandsson, S. Ben-Haim, and B. F. Hutton, "Iterative deconvolution of simultaneous 99mTc and 201Tl projection data measured on a CdZnTe-based cardiac SPECT scanner," *Phys Med Biol,* vol. 56, pp. 1397-414, Mar 7 2011.

[136] X. He, C. E. Metz, B. M. W. Tsui, J. M. Links, and E. C. Frey, "Three-class ROC analysis - A decision theoretic approach under the ideal observer framework," *Ieee Transactions on Medical Imaging,* vol. 25, pp. 571-581, May 2006.

[137] X. He and E. C. Frey, "An optimal three-class linear observer derived from decision theory," *Ieee Transactions on Medical Imaging,* vol. 26, pp. 77-83, Jan 2007.

[138] X. He and E. C. Frey, "Three-class ROC analysis - The equal error utility assumption and the optimality of three-class ROC surface using the ideal observer," *Ieee Transactions on Medical Imaging,* vol. 25, pp. 979-986, Aug 2006.

[139] X. He and E. C. Frey, "The meaning and use of the volume under a three-class ROC surface (VUS)," *Medical Imaging, IEEE Transactions on,* vol. 27, pp. 577-588, 2008.

[140] X. He, X. Y. Song, and E. C. Frey, "Application of Three-Class ROC Analysis to Task-Based Image Quality Assessment of Simultaneous Dual-Isotope Myocardial Perfusion SPECT (MPS)," *Ieee Transactions on Medical Imaging,* vol. 27, pp. 1556-1567, Nov 2008.

[141] W. T. Wang, B. M. W. Tsui, D. S. Lalush, C. Tocharoenchai, and E. C. Frey, "Optimization of acquisition parameters for simultaneous Tl-201 and Tc-99m dual-isotope myocardial imaging," *Ieee Transactions on Nuclear Science,* vol. 52, pp. 1227-1235, Oct 2005.

[142] J. Valentin, "Radiation dose to patients from radiopharmaceuticals:(Addendum 2 to ICRP Publication 53) ICRP Publication 80 Approved by the Commission in September 1997," *Annals of the ICRP,* vol. 28, pp. 1-1, 1998.

[143] H. W. Strauss, D. D. Miller, M. D. Wittry, M. D. Cerqueira, E. V. Garcia, A. S. Iskandrian*, et al.*, "Procedure guideline for myocardial perfusion imaging. Society of Nuclear Medicine," *J Nucl Med,* vol. 39, pp. 918-23, May 1998.

[144] M. Ghaly, J. Links, Y. Du, and E. Frey, "Optimization of SPECT using variable acquisition duration," *Society of Nuclear Medicine Annual Meeting Abstracts,* vol. 53, p. 2411, 2012.

CURRICULUM VITAE

Michael Ghaly was born on February 11th, 1981 in Cairo, Egypt. He completed his Bachelor of Science (2004) degree in Systems and Biomedical Engineering from Cairo University. Being in the top 1% of his class, he was offered a faculty position at Cairo University where he worked for four years as a Teaching and Research Assistant. Meanwhile, he was also working as a part-time engineer at GESCA, doing installation, performing acceptance test and providing technical support for various stereotactic radiotherapy systems. During those four years he received a Master of Science (2008) in Systems and Biomedical Engineering from Cairo University with research focused on the development of a Computer Aided Diagnostic system for the automatic detection of malignant masses in digitized mammogram films. He then moved to the U.S upon receiving a fellowship from the Whiting School of Engineering and a Research Assistant appointment from the Division of Medical Imaging Physics, to start a Ph.D. in Electrical and Computer Engineering. He joined the Division of Medical imaging Physics under the supervision of Professor Eric Frey in September 2008. He received the degree of Doctor of Philosophy in Electrical and Computer Engineering in September 2014, with a dissertation focused on the optimization of myocardial perfusion SPECT imaging.

Peer- reviewed Journal Publications:

1. **M. Ghaly**, Y. Du, G. S. Fung, B. M. Tsui, J. M. Links, and E. C. Frey, "Design of a digital phantom population for myocardial perfusion SPECT imaging research," *Physics in Medicine and Biology*, vol. 59, pp. 2935-53, Jun 21 2014.
2. X. Rong, **M. Ghaly**, and E. C. Frey, "Optimization of energy window for 90Y bremsstrahlung SPECT imaging for detection tasks using the ideal observer with model-mismatch," *Medical Physics*, vol. 40, p. 062502, Jun 2013.
3. **M. Ghaly**, Y. Du, J. M. Links and E. C. Frey "Collimator optimization in myocardial perfusion SPECT using the ideal observer and realistic background variability for lesion detection and joint detection and localization tasks" submitted to *Physics in Medicine and Biology*.
4. **M. Ghaly**, J. M. Links and E. C. Frey "Optimization of energy window and evaluation of scatter compensation methods in MPS using the ideal observer with and without model

mismatch and an anthropomorphic model observer" submitted to the *Journal of Medical Imaging*.

5. **M. Ghaly**, J. M. Links and E. C. Frey "Optimization and comparison of simultaneous and separate acquisition protocols for dual isotope myocardial perfusion SPECT" submitted to the *IEEE, Transactions on Medical Imaging*.

Conference Proceedings and Abstracts:

1. **M. Ghaly**, Y. Du, J.M. Links and E.C. Frey "Collimator optimization in myocardial perfusion SPECT using the ideal observer and realistic background variability for lesion detection and joint detection and localization tasks" Image science, *Gordon Research Conference*, 2014.
2. **M. Ghaly**, Y. Du, J.M. Links and E.C. Frey "Ideal Observer for Realistic Detection and Localization Tasks: Application to Collimator Optimization in Myocardial Perfusion SPECT" *IEEE Nuclear Science Symposium and Medical Imaging Conference*, 2013.
3. **M. Ghaly**, J. Links, and E. Frey, "Comparison of scatter compensation methods using the ideal observer with model mismatch," *Society of Nuclear Medicine Annual Meeting* Abstracts, vol. 54, p. 266, 2013.
4. **M. Ghaly**, J. M. Links, Y. Du, and E. C. Frey, "Model mismatch and the ideal observer in SPECT," in *SPIE Medical Imaging*, 2013, pp. 86730K-86730K-9.
5. **M. Ghaly**, J.M. Links and E.C. Frey "Collimator Optimization in Myocardial Perfusion SPECT" *IEEE Nuclear Science Symposium and Medical Imaging Conference*, 2012.
6. **M. Ghaly**, J. Links, Y. Du, and E. Frey, "Importance of including model mismatch in ideal observer-based acquisition parameter optimization in SPECT," *Society of Nuclear Medicine Annual Meeting* Abstracts, vol. 53, p. 326, 2012.
7. **M. Ghaly**, J. Links, Y. Du, and E. Frey, "Optimization of SPECT using variable acquisition duration," *Society of Nuclear Medicine Annual Meeting* Abstracts, vol. 53, p. 2411, 2012.
8. **M. Ghaly** and E. Frey, "Optimization of energy windows and injected activities for dual-isotope simultaneous-acquisition (DISA) myocardial perfusion SPECT using ideal observer (IO) and realistic background variations," *Society of Nuclear Medicine Annual Meeting* Abstracts, vol. 52, p. 2014, 2011.
9. **M. Ghaly**, X. He, Y. Du, G. Fung and E.C. Frey "Optimization of Energy Windows for Dual-Isotope Simultaneous-Acquisition Myocardial Perfusion SPECT using Ideal Observer and Realistic Background Variations" *IEEE Nuclear Science Symposium and Medical Imaging Conference*, 2010.
10. **M. Ghaly**, M., G.S.K. Fung, Y. Du, X. He, J.M. Links, B.M.W. Tsui and E.C. Frey "Design of a Digital Phantom Database for Myocardial Perfusion Imaging Research" *Society of Nuclear Medicine Annual Meeting* Abstracts, vol. 51, p. 1363, 2010.
11. D. Lamba, **M. Ghaly**, P. Greene, J. Hossain and E.C. Frey "Efficient Estimation of Cardiac Time-Activity Curves (TAC) from a Two-Camera SPECT System using Compressed Sensing with Projective Subspace Denoising" *IEEE Nuclear Science Symposium and Medical Imaging Conference*, 2012.
12. T. Ekjeen, C. Tocharoenchai, P. Pusuwan, G.S.K. Fung, **M. Ghaly**, Y. Du and E.C. Frey "Optimization and Evaluation of Compensation Methods and Reconstruction Parameters for

Tc-99m MIBI Parathyroid SPECT” *IEEE Nuclear Science Symposium and Medical Imaging Conference*, 2012.

13. X. Li, **M. Ghaly**, L. Cheng, and E.C. Frey “Patient specific method to determine maximum a posteriori reconstruction hyperparameters for myocardial SPECT” *IEEE Nuclear Science Symposium and Medical Imaging Conference*, 2012.
14. X. Rong, **M. Ghaly** and E.C. Frey “Optimization of energy windows for Y-90 bremsstrahlung SPECT imaging for detection tasks in microsphere brachytherapy” *Society of Nuclear Medicine Annual Meeting* Abstracts, vol. 53, p. 431, 2012.
15. J. Hossain, Y. Du, N. Song, **M. Ghaly**, G.S.K. Fung and E.C. Frey “Investigation of the feasibility of dynamic cardiac imaging with a dual detector gamma camera (DDGC)” *Society of Nuclear Medicine Annual Meeting* Abstracts, vol. 52, p. 2020, 2011.